Emergent phenomena at the conducting interface of insulating oxides with strong spin-orbit coupling

A thesis submitted

by

NEHA

In the partial fulfillment of the requirements for the degree

of

Doctor of Philosophy

Institute of Nano Science and Technology, Mohali, Punjab,India

Indian Institute of Science Education and Research, Mohali, Punjab,India

March 2020

Dedicated to my family,

friends & teachers

for their endless support

and encouragement.

Declaration

The work presented in this thesis has been carried out by me under the guidance of Dr. Suvankar Chakraverty at the Institute of Nano Science and Technology Mohali. This work has not been submitted in part or in full for a degree, diploma or a fellowship to any other university or institute. Whenever contributions of others are involved, every effort has been made to indicate this clearly, with due acknowledgment of collaborative research and discussions. This thesis is a bonafide record of original work done by me and all sources listed within have been detailed in the bibliography.

Neha

Date:

In my capacity as the supervisor of the candidate's Ph.D. thesis work, I certify that the above statements by the candidate are true to the best of my knowledge.

Dr. Suvankar Chakraverty
Institute of Nano Science and Technology, Mohali

Date:

Acknowledgements

Someone has rightly said "We meet to depart is the law of life but what matters is the journey we go on together". And here, I take this opportunity to express my gratitude to all those who helped me during this odyssey of my Ph.D. and curated my life to come.

First and foremost, I would like to extend my heartfelt gratitude to my thesis supervisor, **Dr. Suvankar Chakraverty**. He is the most dynamic person I have ever met in my life with a perpetual passion and dedication for science and research. I joined Ph.D. with a motive to contribute towards science but this motive was given a real direction by Dr. Suvankar. His command on the subject, clear vision to execute research ideas, positive and energetic attitude helped me to solve every single problem of work very easily. I remember spending hours on a problem and a five minutes discussion with him used to make it vanish away into thin air. His continuous input, innumerable questions, excellent guidance and unparalleled encouragement had been a dependable force to arrive to the conclusions of my Ph.D. work. The extensive knowledge he possess always inspired me and ignited an urge of learning more and more in me. I am fortunate enough to be one of his first two Ph.D. students as coming just out of the cradle after post-graduation, we had no research experience, he not only taught us experimental techniques but also helped building scientific temperament in us. The lab practices learnt from him helped us develop in an extremely organized manner and will be with us forever. I feel, by sharing a lot of his time and experience with us, by instilling in us a strong work ethic and a collaborative spirit, Dr. Suvankar fully prepared us for all-round professional and scholarly work. He not only helped us grow professionally but also the pep talks from him helped us in our personal growth. Even his scoldings were always for our betterment and helped us learn a lot. Also, the love and gentle care we received from his wife, mother and daughter Rheedhi always helped us feel at home and created an excellent growing atmosphere for us. I thank Dr. Suvankar for being the architect of my research career. I would not have imagined a better mentor for my Ph.D. work.

I would like to express my gratitude to **Prof. M. Kawasaki** and **Dr. Denis Maryenko** along with Dr. Suvankar Chakraverty for providing me an opportunity to work in **CEMS, RIKEN, Japan**. This opportunity indeed shaped my career as a thin-film grower. I learnt a lot of things from Dr. Maryenko during my stay in Japan, specifically questioning every possibility for a result and reaching out the

true answer. The discipline and commitment for work learnt during my stay there helped me a lot for planning my experiments for completion of the thesis work.

I would also extend my sincerest gratitude to **Prof. Sushanta Datta Gupta** of Bose Institute Kolkata for his valuable scientific discussions, lectures and theoretical modelling of our research problem. His vast sea of knowledge not only helped us to get a better insight of our research problems, but constant scientific discussions with him helped us learn a lot of fundamental science. I would also like to thank **Dr. Yogesh Singh**, of IISER Mohali for his help in building up understanding of the topological systems and understanding of our experimental results.

My sincere thanks to the theoretical physicists of INST, **Dr. Chandan Bera** and **Dr. Abir De Sarkar** for their help in theoratical modelling of our results. Also, I would like to thank **Dr. Goutam Sheet** and **Dr. Ananth Venkatesan** of IISER Mohali for allowing us to use their lab facilities whenever needed.

I would also like to thank **Dr. Kiran Sankar Hazra** and **Mr. Bhanu Prakash**, for their discussions on professional as well as personal fronts which always kept us motivated and cheerful during our stay in INST.

Also, I am grateful to my thesis and annual review committee members: Dr. Goutam Sheet (IISER Mohali), Dr. Yogesh Singh (IISER Mohali), Dr. Ehsaan Ali, Dr. Chandan Bera and Dr. Abir De Sarkar, for their time, suggestions, insightful comments and encouragement.

I also extend my heartfelt thanks to our Founder Director **Prof. A.K. Ganguli** and **Mr. P.K. Datta** for their love, encouragement and support when we joined the institute. The exceptional energy possesed by Prof. Ganguli and his talks always inspired us to aim high. My sincere thanks to **Director, INST** for providing us great working atmosphere and all the facilities required to complete our tasks during the Ph.D. tenure.

I would also like to take this opportunity to thank the **INST-Aministrative staff**, Dr. Mukesh, Mrs. Gurveen, Mrs. Shweta, Ms. Reena, Mr. Ahuja, Mr. Surinder, Mr. Rajeev, Mr. Dhanjeet, Mr. Rohit, Mrs. Suman, Mrs. Vibha and Mr. Prasad for all the help, love and care they have given to me which made my five years of stay in INST feel short. My acknowledgement would be incomplete without mentioning the non-administrative staff of INST. My heartfelt thanks to our driver bhaiya **Ravinder ji**, our cook **Vikram ji**, our gardeners and all the NPDL-INST guards for their love, support and care. Inspite of constant troubles from us, they always helped us and made our stay in INST really comfortable and safe.

I also want to take this opportunity to thank **Mr. Rupinder Tejpal**, my physics teacher, who is the sole reason that I pursued physics in my higher education. He made learning physics so much fun that at an early stage of life, I was sure to study physics and explore more and more about mother nature through it. I thank him from the core of my heart for being a wonderful teacher and enlightening many students like me.

My sincerest gratitude also goes to **Dr. Vishwajit Gaikwad**, former INST-postdoc, who during his stay in INST showed us how a true researcher should be like. His command on his subject, positive attitude and immense knowledge inspired us a lot. He is a constant source of motivation and encouragement and taught us to never give up.

Ph.D. journey is many times overloaded with work and friends are the ones who can take up all your burden and fill you with fresh energy. I have been lucky enough to be surrounded by really great friends during my stay in INST who made my Ph.D. journey even more enjoyable. First of all, I want to extend my deepest gratitude to my partner **Ruchi**. She is not only my lab partner or my flat partner but she is that integral part of my Ph.D. without whom my journey would have been incomplete. Apart from helping in lab works she took great care of me and pampered me like a mom :p. From cooking lessons to being practical in life, I learnt a lot from her. I would also like to thank **Renu** for making our flat family complete. Her speed of finishing any task and cooking skills always surprise and inspire me. I thank her for a lot of memories that we three made during our stay in Mohali.

I have also been fortunate to have the company of great lab members. I want to thank **Nand Kumar** for being our companion for most part of our journey. His lively and humorous nature is commendable and make tense situations also feel light. I also thank his wife for inviting us over dinner parties. I would also like thank my fellow group members, **Saveena, Ripu, Manish, Anamika, Sharmishtha Anshu and Harsha** for common understanding and helping in lab. All of our collective efforts always made work enjoyable. My special thanks to other NPDL members **Astha, Vibhav, Ajit, Nipun, Mayank and Neeraj**. Without all of them NPDL would have never felt like home. Other than work, the group activities from going for tea, leisurely talks to planning trips, NPDL members really made my stay in INST cherishable for the rest of my life.

I also want to thank **Krishna** for always cheering us up and always helping us in Faraday Lab. Along with Krishna, my thanks to **Venu** and **Naimat** for

being our constant companions and hosts for several dinners. I also acknowledge the support of **Anirban, Harman, Nitya, Pulkit, Kalpesh, Ankur**, Anup, Rajinder, Swati, Rashmi and Soumen throughout our jouney. I take this opportunity to specially thank my university friends **Richa, Anjali, Priyanka, Sudesh, Harkawal, Manu and Bharti Sir** for always being there and refreshing me up by small outings.

Besides the people on professional front, I have been extremely lucky on personal front as well and I owe my heartiest gratitude to the pillar of my strength- my life-partner **Varun**. A person of highly concenterated ossomness, he has been with me right from the very beginning of my journey and knows it even better than me. He not only used to lend me his ears for listening to my problems but has always been a troubleshooter for all of them. His practical approach to carry out research work, his gentle care, sustained support and encouragement helped me beyond words throughout my Ph.D. tenure. I thank him from the core of my heart for being with me throughout the pursuit of my scintific career.

Last but not the least, I would like to thank my whole family for making me the person I am today. I am really blessed to be born in a family full of people to be inspired from. Whether it is the elders like my Daadi ma, Bua, Chachu-Chachi ji, Bua-Fufa jis or my young energetic cousins, everyone has their own role to play. I don't have enough words to thank my parents, **Mr. Pardeep Kumar** and **Mrs. Anupam Sehgal** who nurtured us, their children, to become considerate and independent human beings. The deadly combination of my father's scientific temperament, practical approach towards life and my mother's tender care and positive attitude never let the curiosity in us go down and always pushed us to embrace each task with open arms. The way both of them managed a balanced life between work and family taught me greatly to manage all my works well. I can rightly say that I owe my entire life to them. Finally, I want to extend a heartfelt gratitude to the best gift of my life, my sister, **Deepshikha**. She is the best companion I could have while growing up. There is a long list of things that I learnt from her. Adjustment and time management being two of them. I am extremely lucky to have her always there for me. Her small motivational talks whenever I feel low energize me and inspire me to start fresh. Lastly, I thank one and all involved in the completion of this work.

Neha

Abstract

Semiconductors have been the keystone of the field of electronics for decades. The development of high quality growth techniques and our theoretical understanding enabled the realization of a pool of devices such as transistors etc. and revolutionised the way of human living. However, with the evolution of mankind, there is always a demand of materials with larger integration density and enhanced properties. The urge of attaining new functionalities in modern electronic devices led to the manipulation of spin degree of freedom of an electron along with its charge and gave rise to an altogether new field of "spintronics". Recently, among different classes of materials, "oxides", possessing an astounding variety of properties have emerged as potential candidates for spintronics applications. Oxides, particularly, transition metal oxides (TMOs) are a hunting ground to study many fascinating physical properties due to the interplay between their spin, lattice, and orbital degrees of freedom and the presence of strong electron correlations. The benefit of using TMOs over semiconductors for spintronic applications is that many emergent phenomena can be integrated on a single platform due to the electron correlations present and the materials exhibit a full spectrum of electronic, optical, and magnetic behavior: insulating, semiconducting, metallic, superconducting, ferroelectric, pyroelectric, piezoelectric, ferromagnetic, multiferroic, nonlinear optical effects and so on. All these properties and particularly their integrability in oxides make them the materials of choice for future generation electronic devices.

It has been realized that momentum dependent splitting of spin-bands in an electronic system, the "Rashba effect", plays a key role in spintronic devices and the essential condition to realize the Rashba effect is strong spin-orbit coupling. In this dissertation work, we have tried to explore and study perovskite oxide, $KTaO_3$ (KTO) and fabricate its heterostructure with Mott-insulator $LaVO_3$ (LVO). The aim of choosing KTO is its strong spin-orbit coupling in addition to the simple cubic structure and other properties like high dielectric constant etc. which makes it suitable for future generation spintronic devices. The heterostructure LVO-KTO prepared in this work is found to exhibit emergent phenomena like interfacial conductivity, planar Hall effect and anomalous magnetoresistance due to Rashba spin-band splitting. This makes LVO-KTO a potential candidate for channel material of a spin-transistor. In addition to this, the heterointerface is found to have linear dispersion relation at the crossing point of Rashba spin-bands which is similar to the Dirac cone formation in topological systems and hence the system is a playground to

explore topological phases in oxides which may unravel many mysteries of science. Other than, the LVO-KTO heterostructure, this thesis also focuses on the application of KTO in optoelectronic and storage devices and discusses its photo-response and nano-electrical domain writing using atomic force microscopy tip.

Contents

List of Figures

Chapter 1

Introduction

1.1 Background of the study

Semiconductors have been the substratum of the field of electronics for decades. Starting with the invention of the rectifier in 1874, the invention of point-contact germanium transistor changed the world beyond anything that could have been imagined before them. The application of theories of quantum mechanics to condense matter systems along with the development of high quality growth techniques enabled realization of a pool of devices such as transistors, charge coupled devices, light emitting diodes and so on. The conventional semiconductors silicon, germanium or other group III-V compounds remained the materials of choice for fabrication of these devices for decades because of the room for manipulation of their band structure via doping or external stimuli like electrostatic gating etc. However, the ever existing demand of reducing the feature size of the existing electronic devices sparked a need to look for alternative mechanisms or materials with larger integration density and increased functionality. Among many of the proposed or currently developing concepts and materials, this experimental thesis focuses on two such key areas: 'spintronics' and 'oxide electronics'.

1.1.1 Spintronics

Spintronics, an acronym made from spin and electronics is an emerging field characterized by use of spin degree of freedom for information processing. **Spin**, a

fundamental property of elementary particles was first introduced as a quantum number by Wolfgang Pauli in 1920's. This fundamental property of particles was found to bear all properties of angular momentum and furthermore was, quantized. Ever since then, scientists began to work on this new degree of freedom and studies on spin-polarization, spin-relaxation started coming up.[1, 2] In 1971, Mikhail D'yakonov and Vladimir Perel' predicted spin-Hall effect which was experimentally observed in 1979.[2, 3] Then the study of tunnel-magnetoresistance (TMR) in 1975 and giant-magnetoresistance (GMR) in 1988 laid the foundation a new era[4, 5, 6] and the quest for using this fundamental property of elementary particles for applications in electronics gained momentum in 1990 when Datta and Das proposed the concept of spin-polarized field effect transistor.[7] This marked the beginning of a new field of the spin based electronics or "Spintronics" where the central aim was to get the functionalities of the electronic devices by active manipulation of spin degree of freedom of an electron.

Over the years, the relativistic interaction of particle's spin with its motion inside a potential, known as spin-orbit coupling, evolved from a simple atomic contribution to a key effect that modifies the electronic band structure of the materials. It became one of the essential ingredients of spintronics, locking the charge and spin degrees of freedom of an electron together. Spin-orbit coupling when coupled with other parameters in a solid gave rise to a variety of effects which revolutionised the field of spintronics. For example, the Rashba effect, where if you have a system with relativistic electrons (moving with velocity **v** comparable to speed of light **c**) and an intrinsic electric field (**E**) perpendicular to their direction of motion, then the electrons experience a magnetic field **B** given by $(\mathbf{v} \times \mathbf{E})/c^2$ in the direction perpendicular to both **v** and **E**. The energy dispersion relation, which for a free electron is a degenerate parabola for both up and down spins splits into two parabolas corresponding to up and down spin in this case as shown in **Fig. 1.1**. The strength of the splitting given by Rashba parameter α depends on the strength of the spin-orbit coupling of the system. The interesting thing about this kind of splitting is that if we look at a constant energy value, we have two concentric Fermi surfaces with opposite spin-chiralities and a linear dispersion relation at the band crossing point just like a Dirac point in topological systems. This kind of spin arrangement and band structure open many interesting gateways of fundamental physics to be explored. Also, as seen from **Fig. 1.1(b)**, the spin and momentum of the charge carriers are locked in these kind of systems i.e. for a particular direction of motion (**k**), the direction of spin of electron is fixed. This makes the Rashba effect an im-

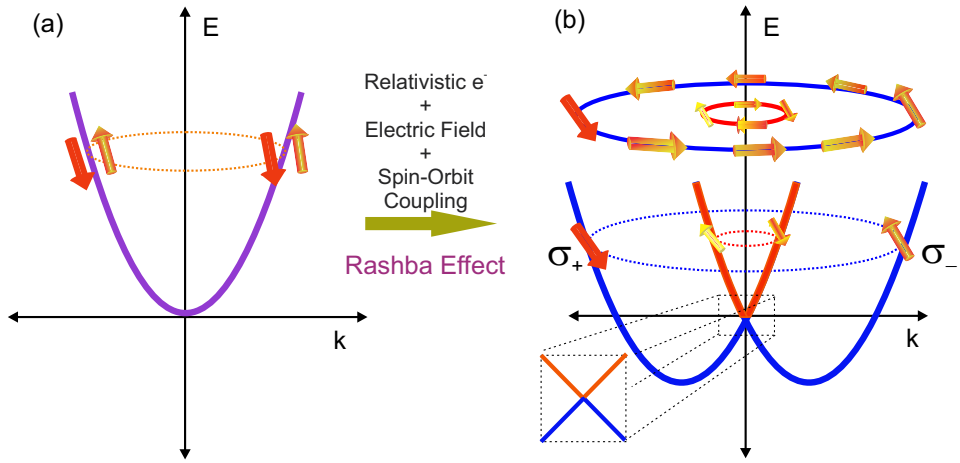

Figure 1.1: Energy dispersion relation: (a) degenerate parabola for free electron (b) spin-split two parabolas for electrons experiencing Rashba field.

portant phenomenon to be used for device applications via control of spin dependent motion of electrons.

The momentum dependent splitting of spin bands in an electron system, the Rashba Effect, is the key pre-requisite for realization of a device called spin-transistor.[8] In a spin-transistor, spin-polarized current from a ferromagnetic source is injected into a conducting channel having an intrinsic electric field perpendicular to the electron wave-vector. If the electrons have relativistic velocities, they experience the Rashba magnetic field. This field, depending on the spin and the direction of propagation of electron, makes it precess. Then controlling the precession of electrons via external electrical field the ON and OFF states of the transistor are realized as shown in **Fig. 1.2**.[9] The advantage of a spin-transitor over a conventional transistor is that its realization is not restricted only to semiconductor materials, its easy control of the on-off swtiching, reduced power consumptiona and smaller leakage currents. Where the source and drain of a spin-transistor are mainly ferromagnetic materials, its channel can be any material with strong spin-orbit coupling. The channel of the spin transistor is an essential component and selection of the right channel material can help in enhancing the efficiency of the device greatly. Here, in this thesis I have mainly focused on selection and synthesis of an optimized channel material with strong spin-orbit coupling.

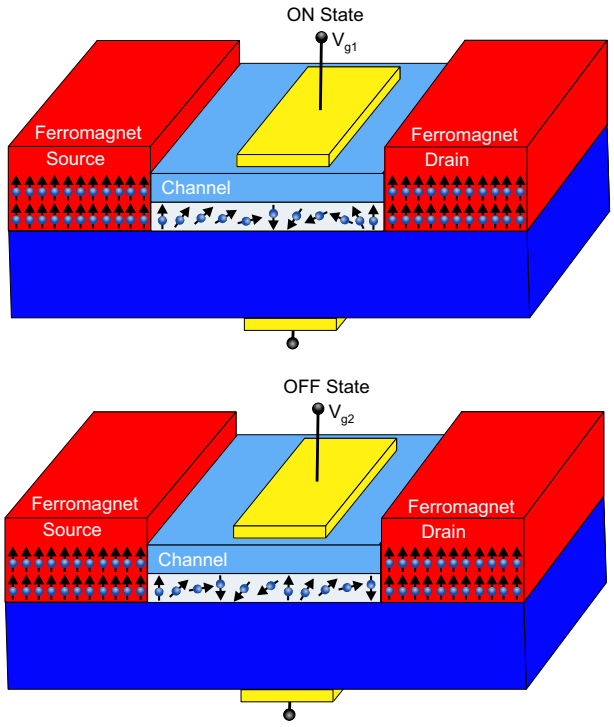

Figure 1.2: Schematic of Datta-Das spin-transistor in ON and OFF state.

1.1.2 Oxide electronics

Oxides which possess an astounding variety of emergent properties are recently gaining attention as the potential candidates for the next generation electronic devices.[10, 11] The oxygen carrying compounds found in almost everything from rocks and glass to ceramics and rust are known to mankind for centuries now. Being the most abundant minerals in the earth's crust and mantle, they form compounds with a vast degree of structural complexity, from simple rock-salt to complex silicates. Particularly, transition-metal oxides are interesting because of the unique nature of their *d*-orbital electrons.[12] Also, the metal-oxygen bond in transition-metal oxides varies from nearly ionic to highly covalent and we have a full range of oxides with metallic properties (e.g. RuO_2, $LaNiO_3$ etc.) on one side and highly insulating oxides (e.g. $BaTiO_3$) on the other side.

Although known for centuries, the field of complex oxides owes its origin to the pioneering work of Sir Neville Mott[13], who identified the complex electronic behavior of oxides. His work for the first time unveiled the role electronic correlations play in determining the transport properties of the complex oxides. In transition metal oxides, the transition metal *s*-electrons are transfered to the oxy-

gen ions and the strongly correlated d-electrons determine their physical properties such as electrical transport, magnetism, thermal conductivity and optical response. The electron-electron correlations in these oxides, limit the number of electrons at a given lattice site and induce an entanglement of spin, charge and orbital degrees of freedom of the carriers. This as a consequence give rise to a wealth of phenomena like metal-insulator transitions, Mott-insulators, charge and spin ordering, multiferroicity and superconductivity etc.[14] A number of interesting phenomena are exhibited by transition-metal oxides for example, $LaMnO_3$ an antiferromagnet in bulk form exhibits ferromagnetic behavior when realized in thin film form. Similarly, ferromagnetism is observerd in (111) oriented superlattice of two antiferromagnetic materials namely, $LaCrO_3$ and $LaFeO_3$.[15] In $SrRuO_3$ thin films, multiple helimagnetic phases are observed indicating the presence of skyrmionic-like topological spin structures and hence, makes it a potential candidate for memory device applications.[16] All these properties and particularly their integrability in oxides makes them the materials of choice for future generation electronic devices. Not only device applications, possibility of realization of Rashba-spin splitting in oxides with strong spin-orbit coupling makes them interesting even from fundamental science perspective because of the linear dispersion relation at the crossing point of two spin-bands. In recent years, there has been a burst of activity to manipulate these phenomena, as well as to create new ones, using oxides.[17] The beauty of oxides is that they have opened the whole periodic table as the playground for the tomorrow's material scientists. Also, the recent developments in the growth techniques is an add on point to enhance the functionalities of the oxides.

Among transition metal oxides, $SrTiO_3$ (STO) had been the material of great interest because of manifestation of exceptional properties from being insulating to superconducting, ferroelectric etc.[18, 19, 20] This simple cubic perovskite oxide has an extremely high dielectric constant at room temperature which scales to as high as $\sim 10^4$ at low temperature making it an ideal oxide for field effect applications.[21] Bulk STO is one of the few known systems to exhibit quantum paraelectricity - a phase in which quantum fluctuations between degenerate lower symmetry configurations suppress ferroelectric ordering.[22, 23] While the bulk of STO is paraelectric, the surface can be ferroelectric. These interesting bulk properties coupled with the improvements in thin film growth techniques lead to an extensive research on STO, including studies on strained STO[24, 25], low dimensional STO[26, 27] and even resulted in realization of conducting 2 dimensional electron gas (2DEG) at the interface of insulating STO with other insulating perovskite oxides.[28, 29, 30] The seminal

work by Ohtomo and Hwang on heterostructure of $LaAlO_3$ (LAO) and STO revolutionised the field of the oxide electronics and brought it on a different level.[28] LAO-STO heterostructure became a hunting ground to explore new functionalities and many emergent phenomena like superconductivity[31], magnetism[32], coexistence of superconductivity and magnetism[33], ferroelectricity[34], charge ordering[35] etc. were witnessed in this heterointerface of insulating, non-magnetic oxides. Not only with LAO, STO was found to form 2DEG at its interface with other oxides as well e.g. $LaVO_3$-STO, $LaTiO_3$-STO, $CaZrO_3$-STO, $GdTiO_3$-STO and $CaHfO_3$/STO etc .[29, 30, 36, 37, 38, 39, 40] However, to extend the use of STO based systems in the emerging spintronic applications, the spin-orbit coupling strength of STO was not very high (17 meV).[41]

In this thesis, we focus on another member of perovskite oxide family, $\mathbf{KTaO_3}$ (KTO), which has properties similar to STO but in addition to them, has a spin-orbit coupling strength of $\sim$400 meV, an order of magnitude higher than that of STO.[41] Inspite of having properties like dielectric constant, crystal structure, lattice constant similar to STO, KTO has been far less investigated. The main obstacle for studying KTO is related to the instability of KTO crystal due to high volatility of potassium.[42] Although a technique to compensate for the volatility was proposed[43] and epitaxial thin films of undoped KTO can be grown[44], not many reports have come up to realize 2DEG at its interface with other oxides or to use its high spin-orbit coupling strength for realization of Rashba-spin splitting for both spintronic or fundamental science applications. This sets the scene for key motivation of this thesis, which is to realize low dimensional electron gas and Rashba-spin splitting in KTO and use its unexplored zoo of properties for future generation spintronic devices. The simple all-oxide system can also be used to understand the rich physics arising in topological systems with linear band dispersion relations.

1.1.3 Thin film technology for oxide electronics

Advances in thin film growth techniques and methods multiply the degrees of freedom available for use of any material, resulting in an extended list of applications and methods to explore fundamental properties of the materials. Similar is the case for oxide thin films and heterostructures. The alluring properties of bulk oxides combined with the advancement in the thin film growth techniques like pulsed laser deposition (PLD) and molecular beam epitaxy (MBE) systems triggered an intense research interest in oxides and gave a new face to the oxide based electronics. The

growth of epitaxial layers bring in new functionalities which coupled with the exotic properties of the correlated complex oxide systems help create integrated devices with combined physical orders.

Thin film growth using PLD or MBE give a vast variety of advantages over bulk samples. First and foremost is the atomic level control of the films which helps in realization of properties not witnessed in bulk form by formation of heterostructures. The properties which are passive in bulk crystals can be made to outshine in the thin film form. The greatest example of this is the work by Ohtomo and Hwang, where thin films of insulating oxide LAO when juxtaposed over TiO_2 terminated band insulator STO single crystal gives a conducting heterostructure.[28] This heterointerface made of non-magnetic oxides LAO and STO is even found to be magnetic.[32] Next is the possibility to achieve high quality single crystal surfaces which help in various surface actuated phenomena, in determining detailed compositional, electronic band dispersions which are not possible in bulk samples due to the defects associated with the growth mechanisms. Thin film growth technology even gives us the controllability of electronic structures of the materials by controlling the epitaxial strain effects during the growth.[45] Another parameter is the precise control of stoichiometry. The control of stoichiometry of any material gives the control over its physical properties because of their predominant dependence on chemical composition of the material. Right from 1988, PLD has been proved to be a valuable thin film deposition technique for oxides for example, superconducting $YBa_2Cu_3O_7$ [46] and piezo/ferro-electric $Pb(Zr,Ti)O_3$ [47] with control on the atomic level. This thesis exploits the thin film growth technology and uses PLD for growth of oxide heterostructures for spintronic applications.

1.1.4 Two dimensional electron gas at the interface of insulator oxides and origin of conductivity

As discussed in the previous section, the initial goal of the extension of thin film techniques was to push the limits of material growth to unit-cell precision to probe the unexplored realm of complex oxides. Methods for creating high-mobility compound semiconductors were widely developed in the 1970s, and the refinements in them resulted in major advances such as the discovery of the integer and fractional quantum Hall effects.[48, 49] As mentioned by Heber in the perspective, the extension of these thin film growth techniques to complex oxides represented a major

new frontier.[17] Harold Hwang, working at Bell Laboratories and managed by Horst Stormer, undertook a program to create atomically precise oxide heterostructures, with the hope that new physics would emerge from these interfaces. Hwang was not disappointed. A milestone was achieved in the field when in 2004, Ohtomo and Hwang observed the charge transfer to occur from single atomic planes and discovered the two dimensional electron gas at the heterointerface of two insulating oxides of LAO and STO grown by PLD. It was a big breakthrough in the field of oxide electronics since two band insultor oxides having large band gap of 5.6 eV(LAO) and 3.2 eV(STO) were found to form a conducting interface. LAO and STO both being perovskite oxides (ABO_3), comprised of alternating planes of AO and BO_2 i.e. LaO and AlO_2 in LAO and SrO and TiO_2 in STO. It was found that for this heterostructure out of the two possible combinations of the interfaces LaO-TiO_2 and AlO_2-SrO (**Fig. 1.3(a)** and **(b)**), only LaO-TiO_2 interface was conducting i.e. the heretrostructures were conducting only when the substrate STO had TiO_2 as the terminating layer. Another interesting observation was that this interface was conducting only above a critical film thickness of 3 monolayers.

This raised several questions about the origin of conductivity at the interface. **Oxygen vacancies** created in the substrate or the film during film deposition and substrate annealing while growth were the most convenient choice to be attributed to the origin of conductivity in such oxide heterostructures. But the fact that the conductivity was dependent on the substrate terminating layer ruled out this possibility. Furthermore to confirm, the LAO-STO samples grown in PLD were then post-annealed in oxygen and it was found that the samples still remained conducting (**Fig. 1.3(c)**). **Figure 1.3(d)** shows the mobility of the as grown and oxygen-annealed samples. It can be seen that the mobility values are almost similar in both the cases. So, this observation also did not support the possibility of oxygen vacancies as the source of conductivity in oxide heterostructures.

Some other studies on the origin of interfacial conductivity proposed that the conductivity at oxide interfaces arises due to the **cationic intermixing**.[50, 51, 52] Reports on insulating and conducting (below and above critical film thickness) LAO-STO heterostructures reveal a complex competition between structural distortions and reconstruction, donor doping and ionic compensation which might be responsible for metal-insulating transition. Experimental evidences suggested that La atoms get interchanged with Sr atoms across the interface causing n-type doping in the STO substartes which might be responsible for giving rise to conductivity at interface. On the other hand, in-plane compressive strain was found to be extended

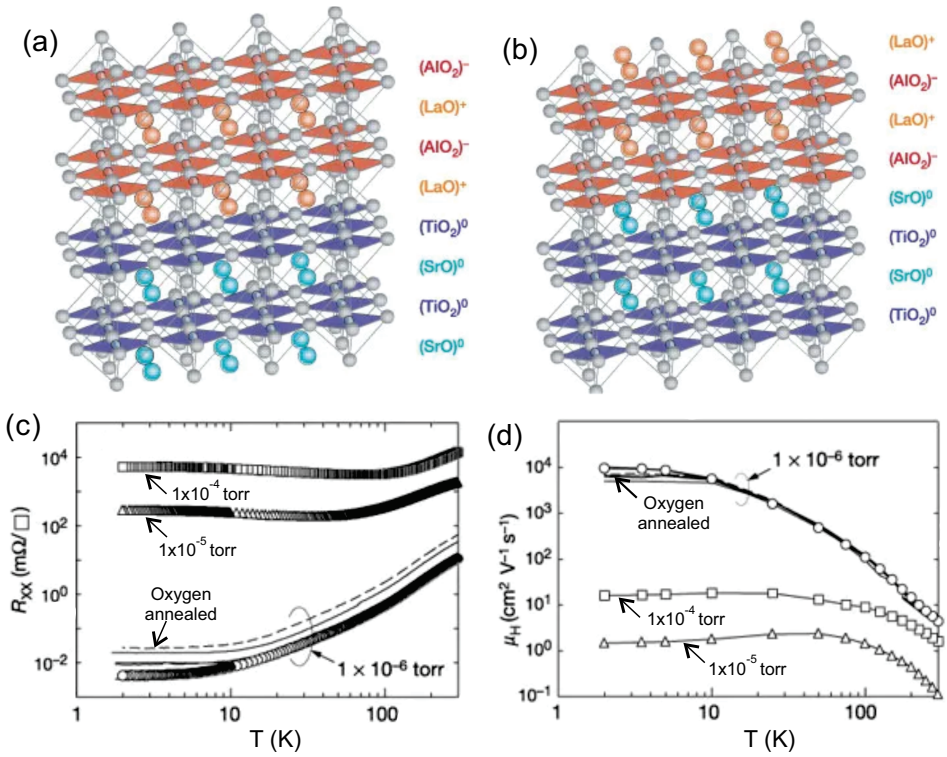

Figure 1.3: Schematic of possible interfaces between LAO and STO (a) LaO-TiO_2 interface (b) AlO_2-SrO interface. (c) and (d) Temperature dependent sheet resistance and mobility for LAO-STO interfaces grown at different oxygen partial pressure [28].

deeper within the substrate producing the insulating interface. Hence, it was concluded that cationic intermixing and structural distortions were some of the possible reasons for producing conducting and insulating interfaces between LAO and STO.

Recently, there have been some other reports on LAO-STO heterostructure suggesting that **film stoichiometry** plays an important role in creating the conducting states between these two insulating oxides.[53, 54, 55]

However, the most promising mechanism proposed so far for formation of two dimensional electron gas at the oxide interface is the **electronic reconstruction**.[28, 56] As mentioned above, STO can be decomposed in a sequence of charge neutral SrO and TiO_2 layers, while LAO is a sequence of alternating charged $(LaO)^+$ and $(AlO_2)^-$ planes. When the LAO films are grown on STO substrate, along (001) crystal direction, the alternating charged LAO planes lead to a divergent electrostatic potential. **Figure 1.4(a)** shows the unreconstructed interface between LAO-STO where ρ is the electric charge, **E** is the electric field and V is the electrostatic potential. It shows that the electrostatic potential diverges as LAO

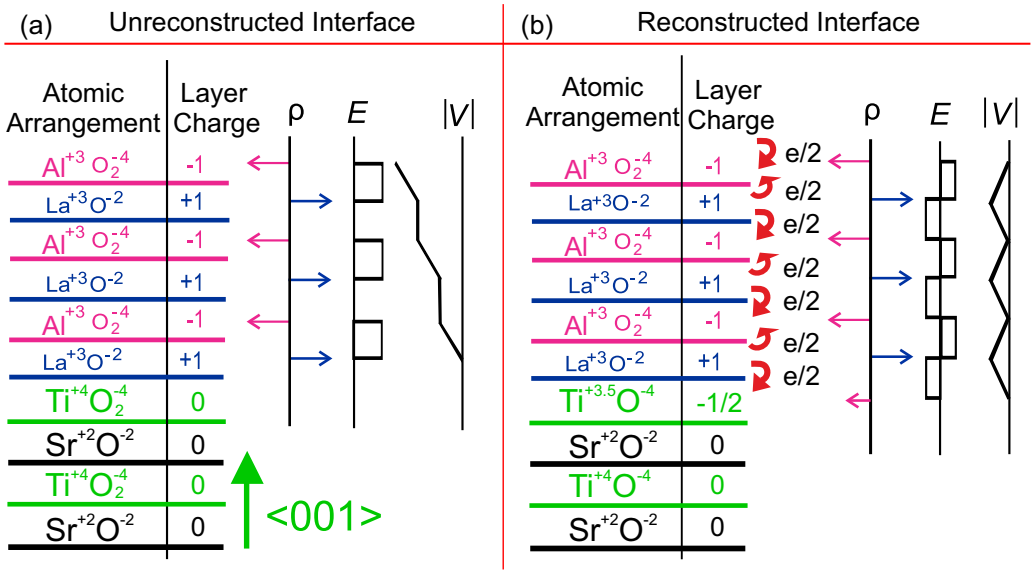

Figure 1.4: Schematic of (a) Unreconstructued (b) Reconstructed interface of LAO-STO.

film thickness increases. This is known as the polar catastrophe. This diverging potential can be prevented by the intrinsic electronic reconstruction, where, electrical charge is transferred from the topmost LAO layer to the LAO-STO interface where owing to the fact that Ti has multiple valence states, the electron is accommodated thus making it conducting interface(**Fig. 1.4(b)**).[28, 29, 56, 57, 58, 59] Experimental evidences have been gradually converging towards the conclusion that the electronic reconstruction is the prime mechanism for the appearance of conducting states at the interfaces. According to this model, a critical film thickness is required to build up such an electric field for providing sufficient driving force to change Ti valence state. This requirement of critical thickness is universal for producing the conducting interfaces of two perovsite oxides even fabricated using different growth techniques and is also observed by several groups working in this field. This mechanism of electronic reconstruction has been successful to anticipate other material combinations as well to realize conducting interfaces.[37, 38, 72, 75] But it could not explain the reason of conducting interfaces between amorphous LAO-STO or(110) oriented LAO-STO. So, the debate to find the ultimate mechanism behind the origin of conductivity at the interface of insulator oxides is still active and the field is open to be explored.

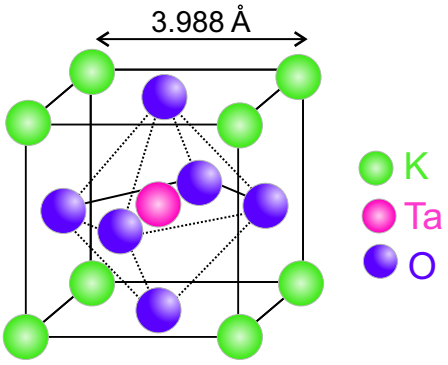

Figure 1.5: Schematic of perovskite structure of $KTaO_3$.

1.2 Properties of $KTaO_3$

In this section, we introduce some physical properties of KTO briefly which make it a prospective candidate for spintronics devices. At room temperature, KTO has a cubic perovskite structure as shown in **Fig. 1.5** with lattice constant of $3.988 A^o$.[60] The alternating charged KO and TaO_2 layers make KTO a polar perovskite oxide. Unlike STO whose crystal structure undergoes a cubic to tetragonal phase transition below ∼110 K[61], KTO does not undergo any such phase transition.

KTO is a semiconductor with a direct band gap of 3.5 eV. **Figure 1.6** shows the calculated band structure of KTO.[62] The conduction band at the Γ point is composed of two degenerate bands, (one light electron band, one heavy electron), together with a spin-orbit split band with splitting energy ∼400 meV. This significant spin-orbit coupling strength and the presence of relativistic electron in Ta $5d$ electrons makes the possibility of realization of Rashba-type spin band splitting in KTO.

KTO can be turned conducting by doping or reduction.[63, 64] Similar to STO, it also has a high dielectric constant at room temperature which increases to ∼4000 at low temperatures due to proximity to ferroelectric instability.[63] This leads to a significant screening of the impurity potentials resulting in a high mobility of $\sim 10^4$ $cm^2V^{-1}s^{-1}$.[63] **Figure 1.7** shows the mobility of reduced KTO at low temperature as a function of volume (3D) charge carrier density in comparison to reduced and chemically doped STO.[63, 65, 66, 67] This high mobility enables the observation of Shubnikov-de Haas (SdH) oscillations, as reported by Uwe et al. for Sr-doped KTO.[68] Even KTO reduced by Ar^+ ion bombardment exhibits SdH oscillations.[69]

In addition to doping or reduction, conduction can also be induced in KTO us-

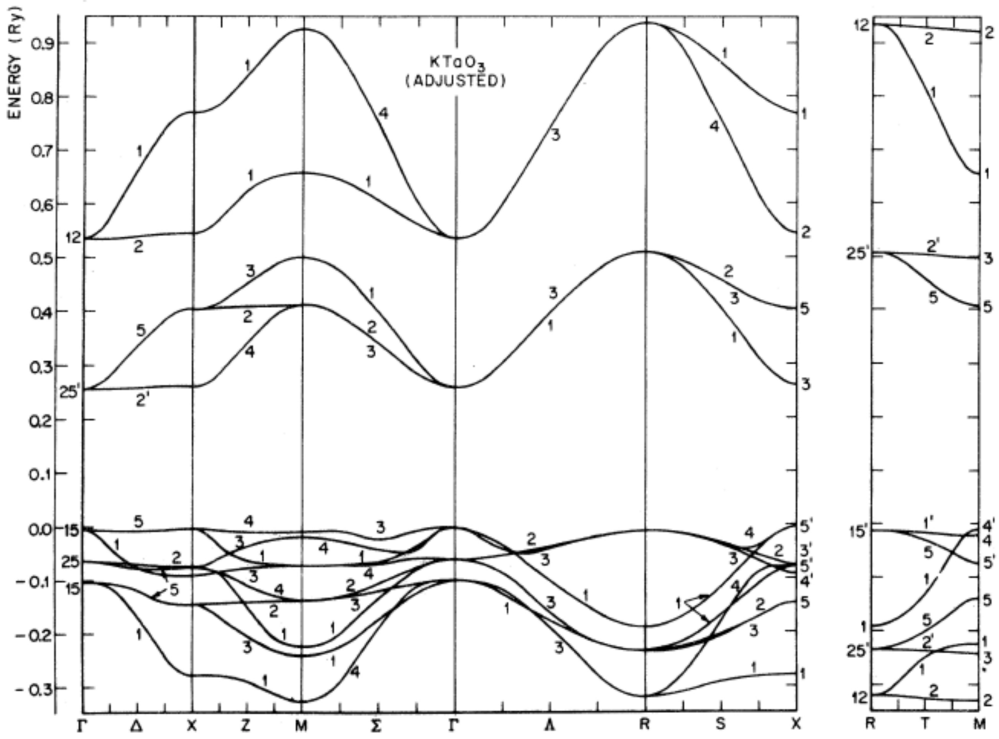

Figure 1.6: Band structure of $KTaO_3$.

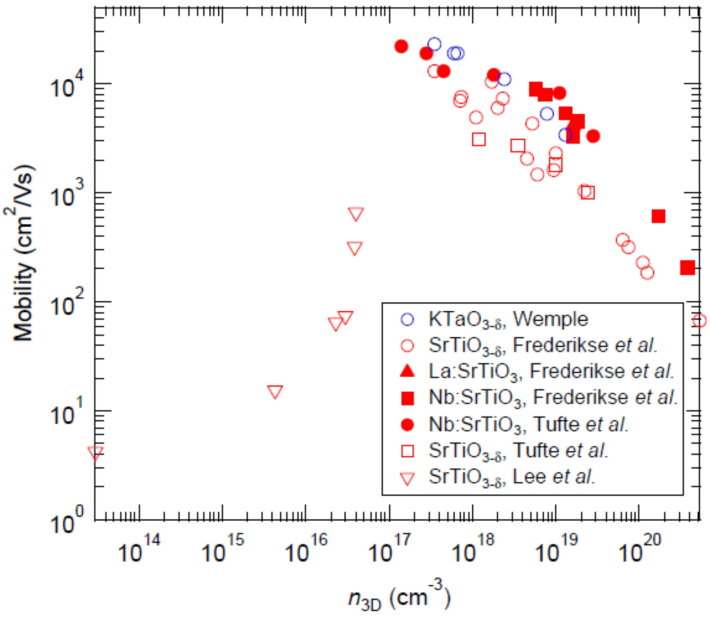

Figure 1.7: Mobility as a function of 3D charge carrier density at T<4.2 K of reduced KTO Wemple[63] and reduced or chemically doped STO Frederikse et al.[65], Tufte et al.[66] and Lee et al.[67].

ing the electric field effect. This was first demonstrated by Ueno et al.[70] Following this work, Nakamura and Kimura[41] reported the observation of weak antilocalisation in electrostatically induced the quasi-two dimensional electron gas at the surface of KTO. They extracted the spin precession length and the phase coherence length of the electrons at various gate voltages. The short spin-precession length obtained by them pointed towards the presence of Rashba-type spin splitting in KTO making it a material of research for future spintronic devices. Other than this, the electrostatic doping by field effect could also make KTO superconducting as demonstrated by Ueno et al.[71]

Inspite of having these alluring properties, unlike STO, KTO has not been explored much for realization of 2DEG at its interface with other oxides. Other than theoretical predictions[72, 73] and reports on amorphous film growths on KTO[74], so far there is only one report on crystalline 2DEG at the interface of $LaTiO_3$ and KTO.[75] Besides other properties, the polar nature of KTO, its strong spin-orbit coupling strength and simple cubic crystal structure makes it even more strong competitor in the run of oxides for electronics device applications. Other than this, the possibility of realization of Rashba effect and spin-band splitting in KTO endows it with an eventuality of topological character because of the formation of Dirac cone at the band crossing point. This makes the study of KTO and its heterostructures even more imperative from the fundamental science point of view. Hence, in this thesis we have undertaken an exploration of properties of KTO and its heterostructure with a Mott-insulator $LaVO_3$ (LVO). Apart from realizing 2DEG at this novel heterointerface and understanding various physical phenomena, we have also tried to use KTO for device applications.

1.3 Scope of the thesis

The main aim of my thesis is to look for perovskite oxides with strong spin orbit-coupling and to use them in thin-film form so that they can form the channel material of the all-oxide spin-transistors. In addition to this several other applications of oxide materials/heterostructures are explored for their applicability in opto-electronic and storage devices.

In order to achieve these aims, the following works and studies are performed which span the eight chapters of this thesis.

First chapter gives a glimpse of the background of spintronics, oxide-

electronics with oxides emerging from scratch to hosting rich physics and bundles of emergent phenomenon. The chapter also introduces the key material of this study KTO and brings out its various properties. It is a broad overview of basic motivation behind my thesis work. **Second chapter** describes the various experimental techniques used to carry out the work. They include the film growth by PLD and various characterization techniques used throughout the study. **Third chapter** deals with the substrate preparation and single termination of KTO for subsequent film depositions. It also discusses the effect of oxygen vacancies, induced during the film growth, on the electronic band structure of KTO. **Fourth chapter** focuses on the synthesis of heterostructure of Mott-insulator LVO with KTO and realization of 2DEG at their interface. The growth parameter optimization and basic characterization like structural and transport properties of the heterointerface are discussed in detail. **Fifth chapter** focuses on the magneto-transport studies performed on LVO-KTO heterointerface. Emergent properties like strong spin-orbit coupling, anisotropic magnetoresistance and planar Hall effect observed at this novel heterointerface are discussed in this chapter. **Sixth chapter** brings out the use of KTO for opto-electronic devices and discuses the photoresponse of KTO. The role of oxygen vacancies in the photoresponse of this oxide material is discussed in detail. In **Seventh chapter**, electrical domain writing on surface of KTO using atomic force microscopy tip is demonstrated. It discusses the use of KTO for electrostatic memory devices. In **Eighth chapter**, I have concluded my thesis work and discussed future possibilities to use KTO in various spintronic applications.

Bibliography

[1] P.M. Tedrow and R. Meservey, *Phys. Rev. B*, **7**, 318 (1973).

[2] M.I. Dyakonov and V.I. Perel', *Fizika Tverdogo Tela*, 13:1382, 1397,(1971).

[3] L. Vorobev, E.L Ivchenko, G. Pikus, I.I. Farbshtein, V.A. Shalygin and A.V. Shturbin *J. Exp. Theor. Phys. Lett.*, **29**, 441 (1979).

[4] M. Julliere, *Phys. Lett. A*, **54**, 225 (1975).

[5] G. Binasch, P. Grunberg, F. Saurenbach and W. Zinn *Phys. Rev. B*, **39**, 4828(R) (1989).

[6] M.N. Baibich, J.M. Broto, A. Fert, F. Nguyen Van Dau and F. Petroff *Phys. Rev. Lett.*, **61(21)**, 2472 (1988).

[7] S. Datta and B. Das *Appl. Phys. Lett.*, **56**, 665 (1990).

[8] Y.A. Bychkov and E.I. Rashba *JETP Lett.*, **39**, 78 (1984).

[9] S. Sugahara and J. Nitta *Proceed. IEEE*, **98(12)**, 2124 (2010).

[10] M. Lorenz et al. *J. Phys. D: Appl. Phys.*, **49**, 433001 (2016).

[11] M.Coll et al. *Appl. Surf. Sci.* , **482**, 1 (2019).

[12] C.N.R. Rao *Annu. Rev. Phys. Chem.*, **40**, 291 (1989).

[13] N.F. Mott, *Taylor and Francis*, London, ed. 2, (1990).

[14] M.Imada, A. Fujimori and Y. Tokura, *Rev. Mod. Phys.*, **70**, 1039 (1998).

[15] K. Ueda, H. Tabata and T. Kawai, *Science*, **280**, 1064 (1998).

[16] S. Chakraverty, T. Matsuda, H. Wadati, J. Okamoto, Y. Yamasaki, H. Nakao, Y. Murakami, S. Ishiwata, M. Kawasaki, Y. Taguchi, Y. Tokura, and H. Y. Hwang *Phys. Rev. B*, **88**, 220405(R) (2013).

[17] J. Heber, *Nature*, **459**, 28 (2009).

[18] J.F. Schooley, W.R. Hosler, and M.L. Cohen, *Phys. Rev. Lett.*, **17**, 474 (1964).

[19] T. Mitsui and W.B. Westphal, *Phys. Rev.*, **124**, 1354 (1961).

[20] M. Kim, C. Bell, Y. Kozuka, M. Kurita, Y. Hikita and H.Y. Hwang *Phys. Rev. Lett.*, **107**, 106801 (2011).

[21] T. Sakudo and H.Unoki, *Phys. Rev. Lett.*, **26**, 1147 (1971).

[22] R.A. Cowley, *Phys. Rev.*, **134**, A981 (1964).

[23] K.A. Muller and H. Burkard, *Phys. Rev. B*, **19**, 3593 (1979).

[24] P. Warusawithana, C. Cen, C.R. Sleasman, J.C. Woicik, Y. Li, L.F. Kourkoutis J. A. Klug, H. Li, P. Ryan, L.-P. Wang, et al., *Science*, **324**, 367 (2009).

[25] A. M. Kolpak, F.J. Walker, J. W. Reiner, Y. Segal, D. Su, M. S. Sawicki, C. C. Broadbridge, Z. Zhang, Y. Zhu, C. H. Ahn, et al., *Phys. Rev. Lett.*, **105**, 217601 (2010).

[26] J. Son, P. Moetakef, B. Jalan, O. Bierwagen, N. J. Wright, R. Engel-Herbert, and S. Stemmer, *Nat. Mater.*, **9**, 482 (2010).

[27] Y. Kozuka, M. Kim, C. Bell, B. G. Kim, Y. Hikita, and H. Y. Hwang, *Nature*, **462**, 487 (2009).

[28] A. Ohtomo and H.Y. Hwang, *Nature*, **47**, 424 (2004).

[29] Y. Hotta, T. Susaki, and H.Y. Hwang, *Phys. Rev. Lett.*, **99**, 236805 (2007).

[30] Y. Chen, F. Trier, T. Kasama, D.V. Christenen, N. Bovet, Z.I. Balogh, H. Li, K.T.S. Thyden, W. Zhang, S. Yazdi, P. Norby, N. Pryds, and S. Linderoth, *Nano Lett.*, **15**, 1849 (2015).

[31] N. Reyren, S. Thiel, A.D. Caviglia, L.F. Kourkoutis, G. Hammerl, C. Richter, C.W. Schneider, T. Kopp, A.-S. Ruetschi, D. Jaccard, et al., *Science*, **317**, 1196 (2007).

[32] A. Brinkman, M. Huijben, M.V. Zalk, J.Huijben, U. Zeitler, J.C. Maan, W.G. Van Der Wiel, G. Rijnders, D.H.A. Blank and H. Hilgenkamp *Nat. Mater.*, **6**, 493 (2007).

[33] L. Li, C. Richter, J. Mannhart and R.C. Ashoori *Nat. Phys.*, **7**, 762 (2011).

[34] V.T. Tra et al. *Adv. Mater.*, **25**, 3357 (2013).

[35] S. Kumar and J.V.D. Brink *Phys. Rev. B*, **78**, 155123 (2008).

[36] F. Li et al. *Phys. Rev. Mater.*, **3**, 100803(R) (2019).

[37] J. Biscaras, N. Bergeal, A. Kushwaha, T. Wolf, A. Rastogi, R. C. Budhani and J. Lesueur *Nature*, **1**, 89 (2010).

[38] J. Betancourt, T. R. Paudel, E. Y. Tsymbal and J. P. Velev *Phys. Rev. B*, **96**, 045113 (2017).

[39] M. Zhang, K. Du, T. Ren, H. T., Z. Zhang, H. Y. Hwang and Y. Xie *Nat. Commun.*, **10**, 4026 (2019).

[40] K. Yang, S. Nazir, M. Behtash and J. Chang *Scien. Rep.*, **6**, 34667 (2016).

[41] H. Nakamura and T. Kimura *Phys. Rev. B*, **80**, 121308 (2009).

[42] K. Szot, W. Speier, M. Pawelczyk, J. Kwapulinski, J. Hulliger, H. Hesse, U. Breuer and W. Quadakkers, *J. Phys.:Condens. Matter*, **12**, 4687 (2000).

[43] H.M. Christen, D.P. Norton, L.A. Gea and L.A. Boatner, *Thin Solid Films*, **312**, 156 (1998).

[44] M. Tyunina, J. Narkilahti, M. Plekh, R. Oja, R.M. Nieminen, A. Dejneka and V. Trepakov, *Phys. Rev. Lett.*, **104**, 227601 (2010).

[45] Y. Konishi, Z. Fang, M. Izumi, T. Manako, M. Kasai, H. Kuwahara, M. Kawasaki, K. Terakura, and Y. Tokura, *J. Phys. Soc. Jpn.*, **68**, 3790 (1999).

[46] D. Dijkkamp, et al., *Appl. Phys. Lett.*, **51**, 619 (1987).

[47] J.S. Horwitz, et al., *Appl. Phys. Lett.*, **59**, 1565 (1991).

[48] K.von Klitzing, *The quantized Hall effect (Nobel Lecture)*, (Singapore: World Scientific) (1985).

[49] H.L. Stormer, *Rev. Mod. Phys.*, **71**, 875 (1999).

[50] H. Zaid, M. H. Berger, D. Jalabert, M. Walls, R. Akrobetu, I. Fongkaew, W. R. L. Lambrecht, N. J. Goble, X. P. A. Gao, Berger and A. Sehirlioglu, *Scien. Rep.*, **6**, 28118 (2016).

[51] A. S. Kalabukhov, Yu. A. Boikov, I. T. Serenkov, V. I. Sakharov, V. N. Popok, R. Gunnarsson, J. Borjesson, N. Ljustina, E. Olsson, D. Winkler, and T. Claeson, *Phys. Rev. Lett.*, **103**, 146101 (2009).

[52] G.S. A. Chambers, M. H. Engelhard, V. Shutthanandan, Z. Zhu, T. C. Droubay, L. Qiao, P. V. Sushko, T. Feng, H. D. Lee, T. Gustafsson, E. Garfunkel, A. B. Shah, J. M. Zuo and Q. M. Ramasse, *Surf. Scien. Rep.*, **65**, 317 (2010).

[53] E. Breckenfeld, N. Bronn, J. Karthik, A. R. Damodaran, S. Lee, N. Mason and L. W. Martin, *Phys. Rev. Lett.*, **110**, 196804 (2013).

[54] H. K. Sato, C. Bell, Y. Hikita and H. Y. Hwang, *App. Phys. Lett.*, **102**, 251602 (2013).

[55] M. P. Warusawithana, C. Richter, J. A. Mundy, P. Roy, J. Ludwig, S. Paetel, T. Heeg, A. A. Pawlicki1, L. F. Kourkoutis, M. Zheng, M. Lee, B. Mulcahy, W. Zander, Y. Zhu, J. Schubert, J. N. Eckstein, D. A. Muller, C. S. Hellberg, J. Mannhart and D. G. Schlom, *Nat. Commun.*, **4**, 2351 (2013).

[56] N. Nakagawa, D. F. Bogorin, H. Y. Hwang and D. A. Muller, *Nat. Commun.*, **5**, 204 (2006).

[57] M. B. Shalom, A. Ron, A. Palevski and Y. Dagan, *Phys. Rev. B*, **105**, 206401 (2010).

[58] L. Li, C. Richter, J. Mannhart and R. C. Ashoori, *Nat. Phys*, **7**, 762 (2011).

[59] S. Okamoto and A. J. Millis, *Nature*, **428**, 630 (2004).

[60] G. A. Samara and B. Morosin, *Phys. Rev. B*, **8**, 1256 (1973).

[61] H. Thomas and K. A. Muller, *Phys. Rev. Lett.*, **21**, 1256 (1968).

[62] L.F. Mattheiss, *Phys. Rev. B*, **6**, 4718 (1972).

[63] S.H. Wemple, *Phys. Rev.*, **137**, A1575 (1965).

[64] A. Sakai, T. Kanno, S. Yotsuhashi, H. Adachi and Y. Tokura *Jpn. J. Appl. Phys.*, **48**, 097002 (2009).

[65] H.P.R. Frederikse and W.R. Hosler *Phys. Rev.*, **161**, 822 (1967).

[66] O.N. Tufte and P.W. Chapman *Phys. Rev.*, **155**, 796 (1967).

[67] C. Lee, J. Yahia and J.L. Brebner *Phys. Rev. B*, **3**, 3525 (1971).

[68] H. Uwe, J. Kinoshita, K. Yoshihiro, C. Yamanouchi and T. Sakudo *Phys. Rev. B*, **19**, 3041 (1979).

[69] S. Harashima, C. Bell, M. Kim, T. Yajima, Y. Hikita and H.Y. Hwang *Phys. Rev. B*, **88**, 085102 (2013).

[70] K. Ueno, I.H. Inoue, T. Yamada, H. Akoh, Y. Tokura and H. Takagi *Appl. Phys. Lett.*, **84**, 3726 (2004).

[71] K. Ueno, S. Nakamura, H. Shimotani, H.T. Yuan, N. Kimura, H. Aoki, Y. Iwasa and M. Kawasaki *Nat. Nanotechnol.*, **6**, 408 (2011).

[72] Y. Wang, W. Tang, J. Cheng, M. Behtash, and K. Yang *ACS Appl. Mater. Interfaces*, **8**, 13659 (2016).

[73] F.N. Wang, J.C. Li, Y. Li, X.M. Zhang, X.J.Wang, Y.F. Chen, J. Liu, C.L. Wang, M.L. Zhao and L.M. Mei *Chin. Phys. B*, **28(4)**, 047101 (2019).

[74] H. Zhang, H. Zhang, X.Yan, X. Zhang, Q. Zhang, J. Zhang, F. Han, L. Gu, B. Liu, Y. Chen, B. Shen and J. Sun *ACS Appl. Mater. Interfaces*, **9**, 36456 (2017).

[75] K. Zou, S.I. Beigi, K. Kisslinger, X. Shen, D. Su, F.J. Walker and C.H. Ahn *APL Materials*, **3**, 036104 (2015).

Chapter 2

Experimental methods for growth and characterization

2.1 Thin film growth by Pulsed Laser Deposition

Pulsed Laser Deposition (PLD)- a powerful tool to deposit high quality compact thin films and multilayered structures was used for fabrication of the heterostructures undertaken in this study. In the past couple of decades, PLD has emerged as one of the most popular and immensely simple techniques for depositing a wide range of exciting materials being explored for next-generation applications.[1, 2, 3, 4] PLD is a popular thin film growth technique due to its inherent versatility, flexibility, and speed of the process that can be applied to essentially any material, from simple metals, to binary compounds, to multicomponent high-quality single crystals.[3] Particularly, for oxides PLD became a preferred deposition technique after the discovery of high-temperature superconductors in 1986.[5] High temperature superconductor materials were perovskites and presented unique challenges for thin-film deposition; they were multicomponent, they were oxides, and their final properties were highly dependent on oriented and/or epitaxial film growth. But their successful growth by PLD made it a suitable choice for oxide thin film growth.[6, 7, 8]

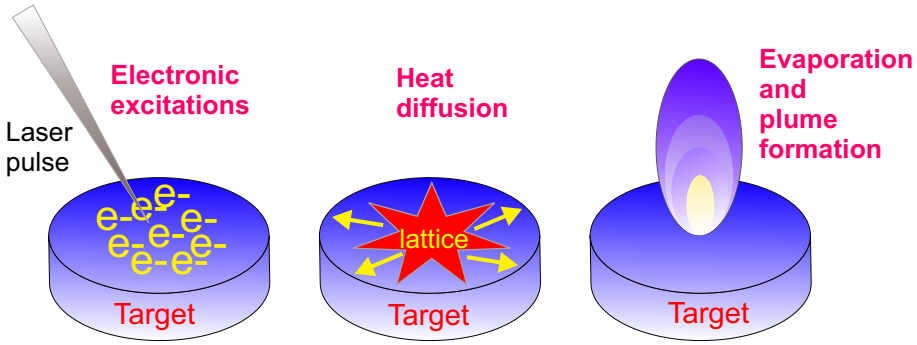

Figure 2.1: Schematic of laser beam interaction with target and formation of plume.

2.1.1 Basic Principle

The principle of PLD involves a simple process where an intense laser beam is made to incident and interact with the surface of a bulk material- the target. The interaction results in electronic excitations in the irradiated area followed by heating and thus evaporation of the target material from the ablated region and formation of plume (**Fig. 2.1**). The vapors in the plume expand and reach the substrate surface where they condensate and create thin layer of material removed from target.[3] Although a simple process, the mechanism behind the growth technique comprises a lot of complex phenomena and achievement of a desired thin film of defined properties requires adjustment and control of a wide range of conditions and parameters involved. Each of them has its own unique role to play in the growth of the film. Some of the important parameters are discussed below:

Laser fluence, defined as the laser energy falling per unit area of the target is a crucial parameter for film growth. It is reported that depending upon laser fulence and the shape of the laser spot on the target, the stoichiometry of the deposited material change significantly from the target composition. As clear from the definition, laser fluence can be steered either by changing the laser energy or by controlling the laser spot area by playing with the optics of the laser.

Deposition rate, is another important parameter for stoichiometric transfer of the target material to the substrate. This mainly depends on the laser fluence. For fixed laser spot area, deposition rate can be tuned by changing the laser energy.

Substrate temperature is one of the most vital factors influencing the quality of the film growth. It controls the nucleation density and plays a great role in

deciding the morphology of the film grown. In addition to this, the diffusion of the target species on the substrate surface also greatly depends on the substrate temperature. The substrate temperature can be controlled by thermal heating or by using infrared heating lasers.

Ambient pressure, is another substantial parameter which controls the dynamics of the plume and the growth kinetics. Depending upon the ambient pressure the scattering of the ablated particles differs and affects the shape of the plume and hence the growth kinetics. Optimization of the deposition chamber pressure is crucial because where too high background pressure causes scattering and impedes the growth process, too low partial pressure leads to a higher kinetic energy of the ablated species leading to resputtering of the already grown film. Also, in many cases coupled with the substrate temperature the ambient pressure results in formation of defects in the grown films such as oxygen vacancies in case of oxides.

In addition to the above parameters, some other factors like distance between the target and the substrate, repetition rate of laser pulses, angle of incidence of laser beam on the target are also optimized to have the desired film growth. Depending on the choice of parameters, there are three possible growth modes by which the films grow:

Layer-by-layer growth: In this growth mode, islands of the ablated material nucleate on the surface of the substrate until a critical island density is achieved. With more and more material being added, the islands grow in size until they run into each other. This is known as coalescence. Once coalescence is reached, the more material is added into the empty spaces to complete one layer and this process is repeated for each subsequent layer.

Step-flow growth: This growth mode occurs when the substrates have a miscut associated with the crystal which gives rise to atomic steps on the surface of the substrate. In this mode, the ablated atoms reach the substrate surface and diffuse to a step edge before they have a chance to nucleate an island. The growing surface is viewed as steps traveling across the surface. Usually, this growth mode occurs at high growth temperatures.

3D growth: This growth mode is like the layer-by-layer growth. The difference is that once an island is formed, the next island nucleates on top of it. Therefore, the growth does not persists in a layer-by-layer fashion and the surface roughness increases each time the material is added.

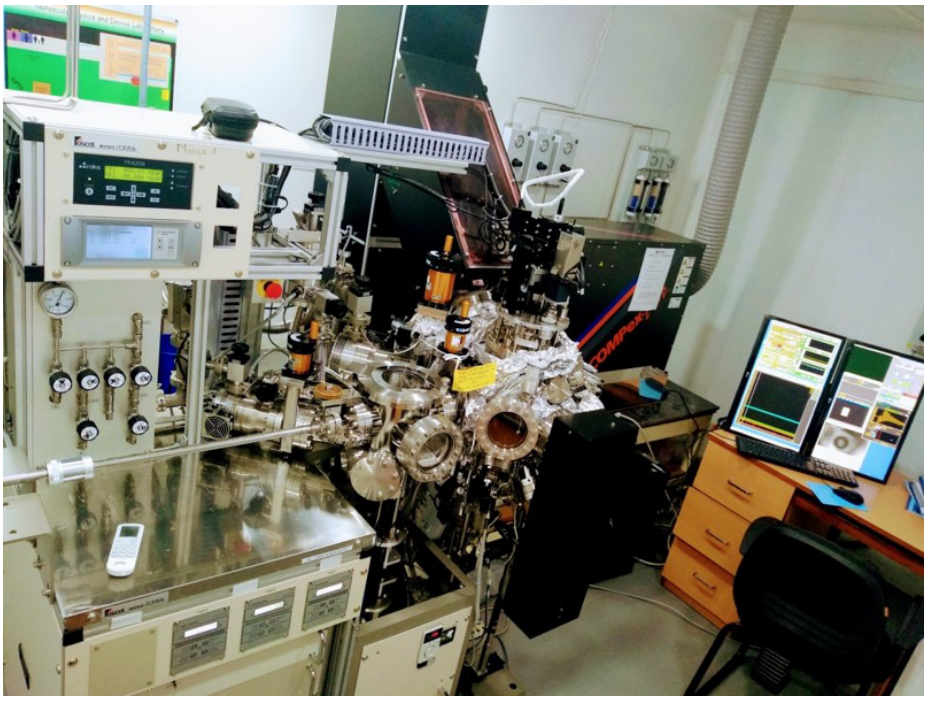

Figure 2.2: Picture of our PLD system, Mobile-Combi-Laser MBE.

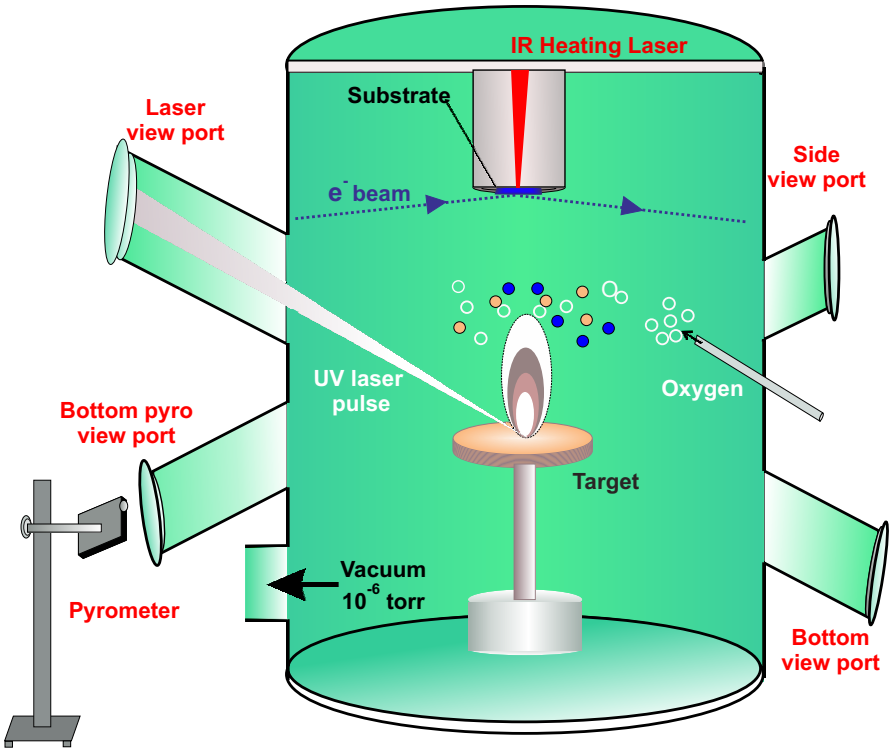

Figure 2.3: Schematic of the deposition chamber of our PLD system.

2.1.2 Experimental set-up

Our combinatorial pulsed laser deposition system, Mobile-Combi-Laser MBE by Pascal, used in this study consists of a load-lock chamber and a main chamber. Turbo-molecular pumps followed by roughing by rotary pumps are used to evacuate the chambers and the base pressure of the main chamber is kept to less than 10^{-8} Torr. The substrate is heated by an infrared (IR) laser of 809.5 nm via a SiC plate. The substrates can be heated using a focused lens for developing a temperature gradient across the length of the substrate or by using a lens of higher focal length for uniform heating of the substrate. Two pyrometers one at the top of the substrate and one at the bottom are used to measure the temperature. The temperature is precisely controlled by a proportional-integral-derivative (PID) controller. Gases can be supplied in our deposition chamber during growth and the pressures are maintained depending on the growth requirements. The gas pressure of the main chamber is manually adjusted by controlling the rate of the gas injection and is measured by ion gauges at low pressure, and a thermo-couple gauge at high pressure. The film growth and the thickness is monitored by reflection high-energy electron diffraction (RHEED) system as discussed in the next section. The main chamber is equipped with six target holders and two motor operated masks which can be used for the combinatorial film growths. For ablating the targets, a 248 nm KrF excimer laser (Compex, Coherent) with a pulse duration of 20 ns is used. The output energy of the laser pulse is controlled by varying the input excitation voltage. In addition to this, we can control the spot area of the ablated region by varying the position of a motor operated lens which focusses the laser beam onto the target. **Figure 2.2** shows the picture of our PLD system and **Fig. 2.3** shows the schematic of the deposition chamber.

2.1.3 Reflection high energy electron diffraction technique (RHEED)

RHEED is a significant in-situ film growth monitoring tool which is indispensable for the fabrication of layered structures because of the useful information like surface structure, deposition rate, number of layers and lattice relaxation etc. provided by it.[9, 10, 11] RHEED utilizes diffraction of electrons by the surface atoms and provides information of their periodic arrangement. Being compatible with the (ultra) high vacuum deposition conditions, it is the most preferred technique to know about

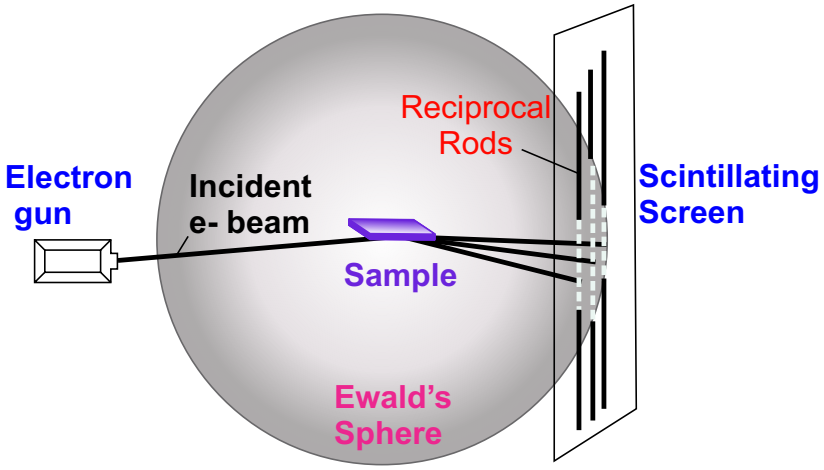

Figure 2.4: Schematic of RHEED measurement geometry and construction of Ewald's sphere.

the surface morphology during thin film growth.[12] RHEED mainly consists of an electron gun and a scintillating screen fixed with camera. To know about the substrate surface properties and film thickness, an electron beam having monoenergetic electrons of typical energy 20 keV are made to incident on the substrate at grazing angles and the diffracted beams from the sample crystal planes are collected at the scintillating screen.[9] **Figure 2.4** shows the schematic of the RHEED measurement geometry and construction of Ewald's sphere. The crossection of the Ewald's sphere and the scintillating screen gives the RHEED pattern and the RHEED spot intensity variation during the growth gives the most important information of the growth mode and thickness of the film. **Figure 2.5** shows the schematic presentation of the RHEED intensity oscillations used to count the number of layers of the film grown. When the electron beam is diffracted from the crystalline surface of the substrate, the intensity of the diffracted beam is maximum (represented by case A). When the ablated material starts depositing on the substrate, the intensity of the diffracted beam reduces because of the scattering by the deposited material (case B). Once the complete layer of the film starts forming, the intensity is regained (cases C and D). By counting the number of these oscillations in the intensity of the diffracted beam, the number of layers of the deposited film can be counted. Also, the RHEED intensity oscillations gives us the deposition-rate and the quality of the film grown. In our study we used RHEED to monitor the layer-by-layer growth of our LVO films over KTO under the optimized conditions.

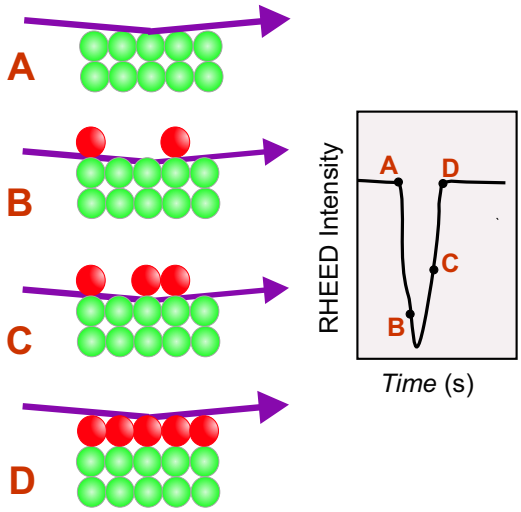

Figure 2.5: Schematic presentation of the RHEED intensity oscillations.

2.2 Surface and structural characterization

The crystalline structure and the surface morphology of epitaxially grown films are a direct result of the various surface processes occurring during growth. The detailed study of the structural as well as surface properties can therefore, help in understanding these processes. Hence, atomic force microscopy is used for the analysis of surface morphology and thin film x-ray diffractometry is used to study the crystalline structure of the grown heterostructures.

Atomic Force Microscopy (AFM): The surface morphology characterization of the heterostructures grown for this study was done using Bruker Multimode-8 AFM which is capable of doing both tapping and contact mode surface scans. SiN tips of force constant around 40 N/m were used for the the normal height profile scans and the surface quality was assessed by the roughness of the film surface. In addition to the morphology studies, AFM was used to write nano-electrical domains over the surface of STO and KTO systems having different origin of conductivity. In such experiments conducting tips of model SCM-PIC having PtIr coating with force constant of 0.2 N/m were used to write the electrical domains in contact mode and conducting and magnetic tips of model MESP having Co/Cr coating with force constant of 2.8 N/m were used to read the written signal in electrostatic/magnetic force microscopy modes.

X-ray diffractometery (XRD): To determine the structure of crystals, XRD is the most widely used technique because of the wavelength of x-rays which is

typically of the order of the atomic spacing. The intensity profile of the diffracted x-ray beams is related to the reciprocal lattice, which is the Fourier transform of the real-space lattice. To determine the crystallinity of the films, θ-2θ scans are performed where θ is the incident angle from the (hkl) plane and 2θ is the diffracted angle from incident x-ray direction. If the thin film is epitaxially grown on the substrate, symmetric reflection gives the out-of-plane lattice spacing according to the Bragg's law,

$$d_{00l} = \frac{l\lambda}{2sin\theta} \tag{2.1}$$

where λ is the x-ray wavelength. XRD can also be utilized to obtain other useful information like in-plane lattice constant by using asymmetric reflection, the thickness of films from fringes near a Bragg peak in the θ-2θ scans, and various kinds of crystal coherence from the broadening of peaks. In the current study, we used Bruker Discover D-8 x-ray diffractometer equipped with a copper target (Cu-K_α $\sim$1.5406 A^o)to characterize our films and substrate crystals.

2.3 Electrical and magnetic transport measurements

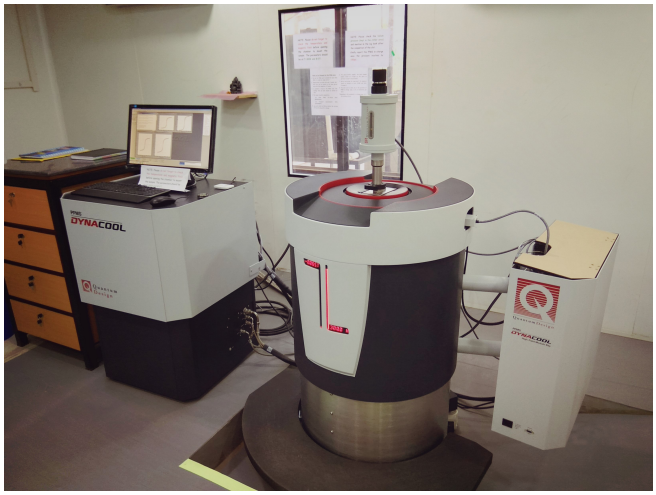

Figure 2.6: Picture of physical property measurement system.

One of the important results of our study was the realization of conducting two dimensional channel at the interface of insulating oxides. For such electrical

transport measurements, we used physical property measurement system (PPMS) by Quantum Design (**Fig. 2.6**). This system was capable of temperature scans from 350 K down to 1.8 K. The magneto-transport measurements were done using magnetic field scans ranging from -14 T to 14 T. Both electrical and magneto-transport measurements were done using electrical transport option (ETO) of PPMS. In addition to this, PPMS' horizontal rotator (HRT) was used to perform angle dependent transport measurements by varying the angle between the magnetic field and the normal to the sample plane or by varying the angle between the magnetic field and the current in the sample plane. For all the transport measurements, electrical contacts were made by Al wire ultrasonically wirebonded directly on the sample surface. The ultrasonic bonds locally depletes the top or capping layer and give a good ohmic contact to the conduction layer at the interface.

2.4 Other Tools

In addition to the above main tools and techniques used for fabrication and charcterization of samples in this study, many other equipments have also been used to carry out different parts of study. They include Kiethley source meters 2635B and 2450 capable of working in voltage range of -200V to +200V for photoconductivity measurements. Also, Diode-pumped solid state (DPSS) lasers having wavelength 405 nm and 532 nm have been greatly used to check the effect of photo-excitation of the carriers in our oxide samples.

Bibliography

[1] J.S. Horwitz, K. S. Grabowski, D. B. Chrisey, and R. E. Leuchtner, *Appl. Phys. Lett.*, **59**, 1565 (1991).

[2] G. Koster, L. Klein, W. Siemons, G. Rijnders, J. S. Dodge, C.B. Eom, D. H. A. Blank, and M. R. Beasley *Rev. Mod. Phys.*, **84**, 253 (2012).

[3] R. Eason, *Pulsed laser deposition of thin films:applications-led growth of functional materials*, John Willey and sons, inc., Hoboken, New Jearsy (2007).

[4] A. Ohtomo and H.Y. Hwang, *Nature*, **47**, 424 (2004).

[5] D. Dijkkamp and T. Venkatesan, *Appl. Phys. Lett.*, **51**, 619 (1987).

[6] M.Coll et al. *Appl. Surf. Sci.* , **482**, 1 (2019).

[7] Y. Hotta, T. Susaki, and H.Y. Hwang, *Phys. Rev. Lett.*, **99**, 236805 (2007).

[8] Y. Kozuka, M. Kim, C. Bell, B. G. Kim, Y. Hikita, and H. Y. Hwang, *Nature*, **462**, 487 (2009).

[9] W. Braun, *Applied RHEED: Reflection High-Energy Electron Diffraction During Crystal Growth*, SpringerVerlag, Berlin, (1999).

[10] A. Ichimiya and P. I. Cohen, *Reflection high-energy electron diffraction*, Cambridge (2004).

[11] J.M. McCoy, U. Korte, P. A. Maksym and G. M. Ehmsen *Surf. Sci.*, **261**, 29 (1992).

[12] L. Daweritz, *Superlattices and Microstructures*, **9**, 141 (1991).

Chapter 3

Substrate preparation and single termination of the $KTaO_3$

3.1 Introduction

To study and explore the emergent physical phenomena occurring at the interface of oxide thin film heterostructures, the foremost step is the substrate preparation. The substrate lattice parameter, atomic site termination and chemical compatibility etc. are crucial parameters to be considered carefully so as to obtain high quality epitaxial thin films, superlattices and interfaces. The transition metal perovskite oxides admit a large range of cationic composition in their valence state and stoichiometry and this very fact which is the root of their vast variety of properties, is a crucial thing to be taken care of when considering interfaces between films and substrates. The commercially available perovskite oxide substrates are mechanically cut along a certain crystallographic direction and subsequently polished. There is always a possibility of cuts or polishing imperfections leading to a situation where multiple atomic terminations coexist at the crystal surface severely affecting the growth of epitaxial films on top. In complex oxide systems it is known that a slight change in the atomic termination, crystal orientation or any other parameter of the substrate can result in extremely opposite properties of the heterostructure e.g. the heterostructure of LAO-STO with SrO termination is insulating, on the other hand, LAO-STO heterostructure with TiO_2 termination is found to be even superconducting. This issue is of relevance even in the case of ultrathin transition

metal oxide films having ferroic properties. In such cases, the typical length scale for interactions is within the nanometric range which is comparable to the perovskite unit cell and is therefore extremely sensitive to the local stacking order of the film layers. Indeed depending on the surface of the substrate, many structural, chemical or electrostatic driven reconstructions may take place at the interfaces, thus leading to emerging properties. Hence, a detailed knowledge of the surface properties of the substrate along with proper atomic termination is really crucial to achieve desired functionalities of the heterostructures. As discussed in the first chapter, our substrate KTO, having lattice parameter 3.988 A^o consists of alternating layers of KO and TaO_2 along [001] direction. The commercially available substrates are usually mixed terminated so a method is required to make them singly terminated. Till now single termination of STO has been greatly focused and the first report for it came in 1994, where pure TiO_2 terminated surface of STO was obtained by using selective chemical etching.[1] A buffered NH_4FHF (BHF) solution was used by Kawasaki et al. to dissolve the SrO layer selectively. Similarly, on lines of STO, single termination was tried on KTO using buffered HF solution.[2] However, the use of HF acid is a corrosive method for achieving single atomic termination and distorts the surface of the substrate. In this chapter, we discuss a detailed framework to achieve single TaO_2 terminated surface of KTO which is coveted to observe many interesting phenomena at the interface of LVO-KTO by using simple deionized water etching technique followed by annealing at high temperature. This method results in a good quality single terminated step and terrace structure on KTO and is a non-corrosive process.

In addition to surface characteristics of the substrate, another important factor influencing the properties of the thin films, superlattices or interfaces is the substrate oxygen vacancies. The oxygen vacancies are known to play a crucial role in the modification of surface composition. The entire band structure and hence the transport properties of the conducting electrons of the system can be altered by the presence of oxygen vacancies. There is always a high probability of oxygen vacancies being created in the substrate during growth due to the high temperature annealing of the substrate, low oxygen partial pressure of the deposition chamber or due to knock out of oxygen by the high energy ablated target species. Hence, this makes a detailed study of the effect of oxygen vacancies on the band structure of KTO imperative. In this chapter, we also discuss the effect of oxygen vacancies, created in the KTO substrates, on the electronic band structure of KTO. For studying the effect of oxygen vacancies, we intentionally created oxygen in KTO by Ar^+ ion

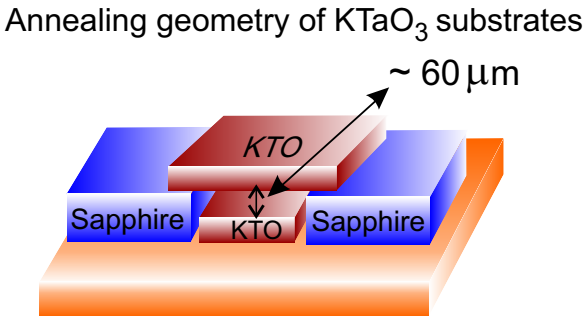

Figure 3.1: Schematic of annealing geometry of KTO substrates.

bombardment and turned them conducting. The sheet charge-carrier density was systematically varied by changing the Ar^+ bombardment time. Combining optical spectroscopy and Kelvin probe force microscopy (KPFM), we saw the appearance of defect states and an anomalous change in work function as a function of oxygen vacancies vis--vis charge-carrier densities. Alongwith our experimental measurements, we also performed density functional theory (DFT) based calculations on the bulk KTO and KTO slab to understand the electronic structure and electron distribution of the KTO surface as a function of oxygen vacancies. Our calculations reveal a strong and nontrivial correlation between oxygen vacancies, surface dipole, and charge distribution in KTO.

3.2 Single termination of KTO

To achieve the single termination of KTO, we used a simple technique of annealing the substrates at high temperatures followed by etching of KO layers with deionized water. **Figure 3.1** schematically presents the steps of our framework to attain single termination of KTO. Since potassium is a volatile material there is always a chance of potassium vacancies being created when KTO is annealed at high temperatures. To avoid this situation, we annealed our KTO substrates by arranging them in a unique geometry. **Figure 3.1** shows the annealing geometry of the KTO substrates. Here, two KTO substrates were annealed simultaneously with one on the top of the other. A gap was maintained between the two substrates with the help of sapphires on the sides as shown in the **Fig. 3.1** This was required to maintain the K vapor pressure between the two substrates to overcome the formation of K vacancies. **Figure 3.2** (a) schematically shows the surface morphology of the as received substrate having mixed termination. On high temperature annealing, we expected the KO particles

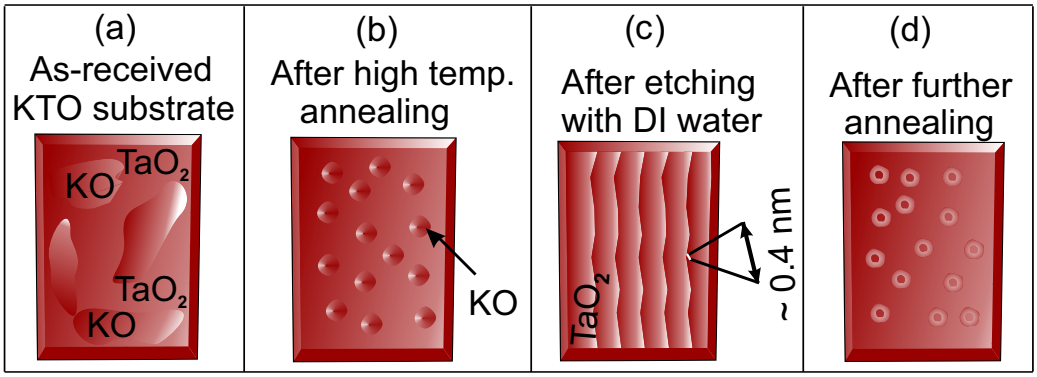

Figure 3.2: Schematic representation of surface morphology of KTO with high temperature annealing. (a)Commercially available mixed terminated surface of KTO. (b) Possible formation of KO particles on the substrate after high temperature annealing. (c) Expected surface morphology of KTO substrate after DI water etching indicating the single terminated steps and terraces surface with step height ∼0.4 nm equivalent to the unit cell of KTO.(d) Further annealing at higher temperature leading to the formation of holes on the KTO surface.

to agglomerate on the surface of KTO as depicted in **Fig. 3.2** (b) which may dissolve in DI water heated at an optimized temperature. This was expected to give the steps and terraces like structure with step height ∼0.4 nm as shown by **Fig. 3.2**. We also expected that further annealing of the substrate may leave holes on the surface of the substrate which is visualized in **Fig. 3.2(d)**. The surface morphology of the samples was checked at each step by atomic force microscope (AFM) (Bruker, Multimode-8).

Following these steps, firstly we identified the annealing temperature for our substrates at which the steps start appearing. For this we used both sides mechanically polished single crystalline KTO(001) substrates of size 5 mm x 5 mm purchased from MTI corporation. **Figure 3.3** (a) shows the AFM image of the KTO as-received substrate. We started annealing our substrates from 500^{o}C in steps of 50^{o}C for two hours at each temperature step. All the annealing was done in air under ambient conditions. To anneal the substrates at each temperature step, the ramp rate was kept 300^{o}C/hour. After attaining the desired temperature, the substrate was kept at that temperature for two hours and then cooled down to room temperature with the rate of 250 ^oC/hour. **Figure 3.3(b)** shows the AFM image of the KTO substrate annealed at 600^o without capping. As expected, we observed

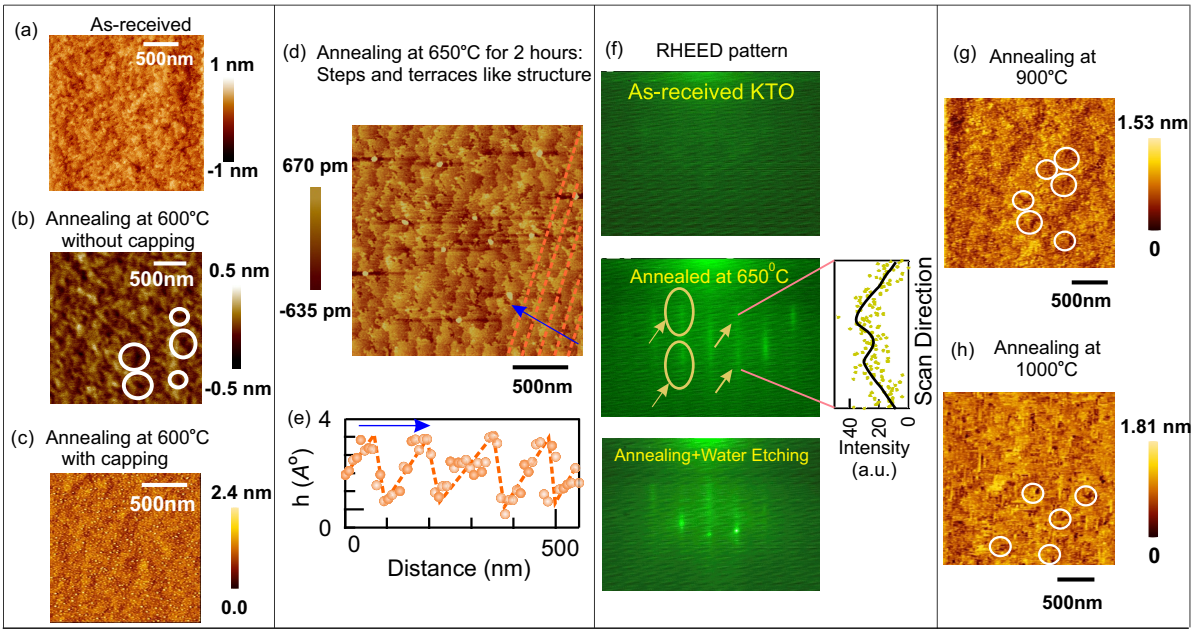

Figure 3.3: (a) AFM image of as-received KTO (001) substrate. (b) Annealing at 600^{o}C of the substrate without capping and formation of holes. (c) Formation of agglomerates and no holes at 600^{o}C with capping. (d) Single terminated steps and terraces like structure of KTO. (e) The graph shows the height profile of treated KTO substrate along the blue arrow. (f) No RHEED pattern in case of as received KTO substrate (top), RHEED pattern of annealed KTO at 650^{o}C (middle) (right panel shows the intensity profile of a stick along vertical direction) and, annealed and water etched KTO substrate (bottom) (g) AFM image of KTO after annealing at 900^{o}C. (h) AFM image of KTO after annealing at 1000^{o}C.

some holes on the surface of the sample which might be due to K vacancies. So we annealed the samples by capping one KTO with another as discussed above. **Figure 3.3(c)** shows the AFM image of the KTO substrate annealed at 600^{o}C with capping. It can be clearly seen that no holes occurred by annealing in this geometry due to the confinement of potassium vapor between two KTO substrates. The gap between the substrates was also optimized. It was varied from 30 μm to 90 μm in gaps of 30 μm and it was observed that the vapor pressure remained effective until 60 μm gap. Higher gap lead to rather rough surface. The capping KTO substrate was taken little bigger than the capped surface by putting sapphires on both the sides as shown in **Fig. 3.1(a)**. It was observed that annealing the samples at

600 ^{o}C lead to the formation of agglomerates at the surface with no appearance of steps. So, we increased the annealing temperature to 650 ^{o}C and it was found that there was formation of steps and terraces along with small agglomerated particles on the surface. These small particles could not be removed by cleaning the samples with acetone-ethanol. To remove these agglomerates, the substrates were etched by DI water at optimized temperature of 60^{o}C. From this, we inferred that most likely these agglomerated particles were KO, which dissolved in water as KOH. After etching these KO particles, steps and terraces like surface of KTO was realized as shown in **Fig. 3.3(d)**. **Figure 3.3(e)** shows the surface profile of KTO with steps and terraces like surface along the blue arrow which clearly suggests the step height of ∼0.4 nm. This is equivalent to the height of one unit cell of KTO. The uniform height profile of one unit cell of KTO (∼0.4 nm) throughout the substrate surface in the form of steps suggested the formation of single terminated surface. Our inference was further confirmed by Reflection High Energy Electron Diffraction (RHEED) observations. RHEED had been performed on KTO substrates at various stages of processing as shown in **Fig. 3.3(f)**. **Fig. 3.3(f)** top image shows that no RHEED pattern is observed for the as-received KTO substrate suggesting mixed terminated rough surface. The formation of crystalline islands (of KO) is suggested by spotty sticks like RHEED pattern shown in the middle image of **Fig. 3.3(f)**, arising from the transmission of electrons through crystalline islands.[3, 4] The intensity graph of second streak from the right of the RHEED pattern (right panel) clearly shows two peaks in intensity justifying the spotty stick structure.[5, 6] **Figure 3.3(f)** bottom image shows intense diffraction spots indicating atomically smooth and well defined surface after hot water etching and annealing.[7] It was observed that further annealing of the substrates at elevated temperature (900^{o}C), even with capping arrangement, lead to the disappearance of steps and left holes on the surface (**Fig. 3.3(g)**). **Fig. 3.3(h)** shows that annealing at 1000^{o}C resulted in the complete distortion of the surface. So, 650^{o}C was identified as the optimum temperature for attaining the TaO_2 terminated surface of KTO.

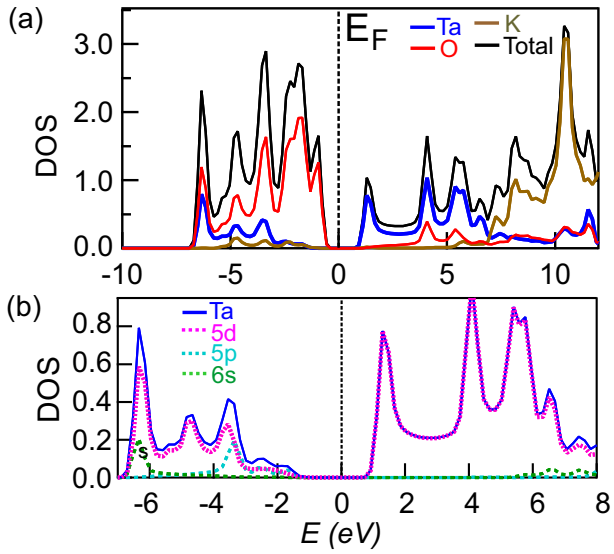

Figure 3.4: (a) Colored lines represent the DOS of individual Ta, O, and K atoms. (b) DOS of $5d$, $5p$, and $6s$ orbitals of Ta along with total DOS of Ta are shown, clearly manifesting $5d$ orbital electrons across the conduction band.

3.3 Effect of oxygen vacancies on electronic band structure of KTO

To study the effect of oxygen vacancies on the electronic structure of KTO, we firstly performed first-principles electronic structure calculations to understand the nature of the electronic charge carriers in KTO. **Figure 3.4(a)** shows the projected density of states of constituent atoms of KTO. **Figure 3.4(b)** further resolves the orbital character of the conducting electrons into "Ta" atom basis states, which suggests clearly that conduction electrons of KTO possess mainly "Ta" $5d$ electronic character. This is in good agreement with the case of STO, which has a strong "Ti" $3d$ electronic character in its conduction electrons as reported by Henrich et al.[8] Infact, this is a crucial point for the choice of KTO for the aim of this thesis, since the presence of d character in conduction electrons is important for spin-orbit coupling.

To create oxygen vacancies, we bombarded the KTO (001) single crystals with Ar^+ ions for different duration of time using reactive ion etch mode in SI500 system (Sentech) at 80 mtorr pressure, -530 V bias voltage, RF power of 225 W and flow rate of 100 SCCM of Ar (initially, the system was kept under high vacuum for one hour and was subsequently conditioned with Ar^+ for another hour). The bias voltage was

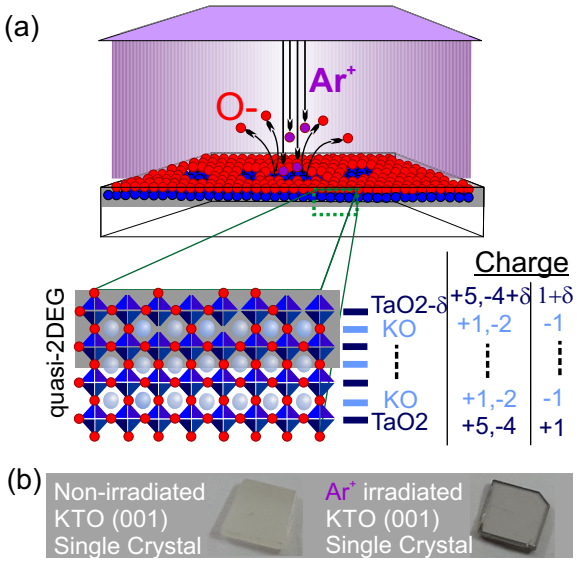

Figure 3.5: Schematic diagram of Ar^+ irradiation of KTO single crystal and possible formation of Q-2DEG due to oxygen vacancies. Lower left panel shows the crystal structure of KTO near and away from surface. Next panel shows the atomic arrangements at different layers. Right panel shows the charge distribution at each layer and formation of n-doped surface. (b) Optical image of nonirradiated (left) and Ar^+ irradiated (right) KTO.

enough to strip oxygen from surface levels.[9] In semiconductor accumulation layers or inversion layers like in Metal Oxide Semiconductor (MOS) structures, the total charge is given by Q=C[V-V_T], where C is the geometric capacitance of the MOS structure. The V_T depends on the band gap as well as impurities that produce localized states. [10, 11] The exposure time in present case is analogous to the applied voltage, increasing the effective charge carrier density. The bombardment energy corresponding to this bias voltage gives rise to a penetration depth of around 15 nm as calculated from:

$$L = 1.1\frac{E^{2/3}W}{\rho(Z_i^{1/4} + Z_t^{1/4})^2}$$

where, E is the energy of Ar^+ in eV, W is the atomic weight of the target in atomic mass units, ρ is the target specific gravity and $Z_{i,t}$ are the atomic numbers of the ion and target respectively.[12] This suggested the formation of a quasi-2D electronic gas (Q-2DEG) system of ∼10 nm thickness. The time of bombardment was varied from 2 to 40 minutes keeping other parameters same. A systematic increase in

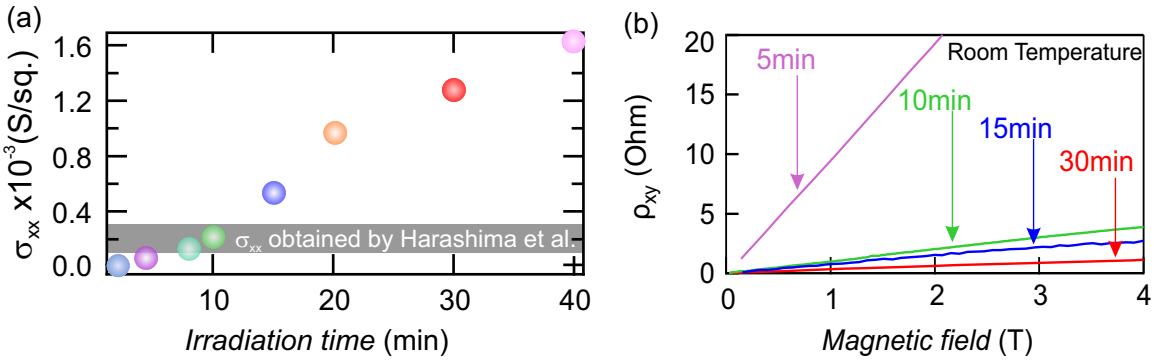

Figure 3.6: (a) Room-temperature sheet conductance as a function of irradiation time. The gray area indicates the values of room temperature sheet conductance reported in Ref. [9]. (b) Hall resistance measurements of Ar^+ irradiated samples at room temperature. Linearity of the curves suggests the presence of a single type of charge carriers (electrons in our case).

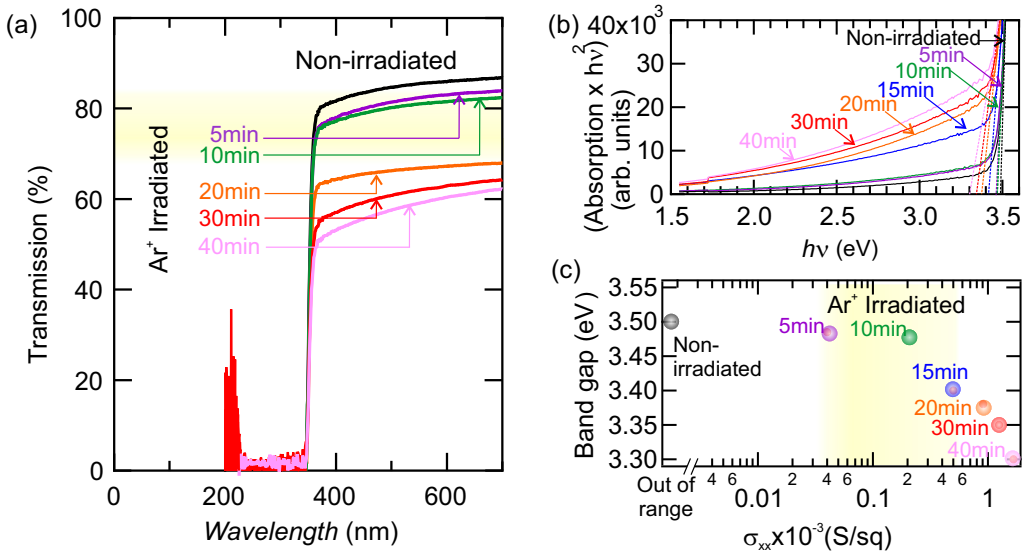

Figure 3.7: (a) Optical transmission data of Ar^+ irradiated and non-irradiated KTO single crystals. (b) (optical absorption x $h\nu)^2$ as a function of photon energy is plotted to estimate the band gap. Dotted lines are tangents to determine the band gap. (c) Band gap of KTO single crystals as a function of room temperature sheet conductance.

sheet conductance of the samples was observed with increasing bombardment time (**Fig. 3.6(a)**) and all the samples were found to be conducting down to 2K. The

irradiation process and possible scenario of oxygen vacancies in KTO crystal upon irradiation is schematically shown in **Fig. 3.5(a)**. After bombardment, the crystals turned greyish black as seen in **Fig. 3.5(b)**. Oxygen vacancies in bulk KTO may also be created by using high temperature annealing as reported for STO.[13] Ar^+ bombardment method in present case was adopted over high temperature annealing in vacuum because potassium is a volatile material and high temperature annealing may create potassium vacancies as well. Ar^+ irradiation might have also caused potassium vacancies in the system. To check this possibility, we annealed all the bombarded samples in air at 400^{o}C for 4 hours, and all conducting samples turned insulating. This suggests the appearance of conductivity is due to oxygen vacancies. On increasing the irradiation time from 2 to 40 minutes, there was an increase in the charge carrier density from 1.3 x 10^{13} to 1.7 x 10^{15} cm^{-2} and hence, the conductance increased by almost 2 orders of magnitude as observed in **Fig. 3.6(a)**.

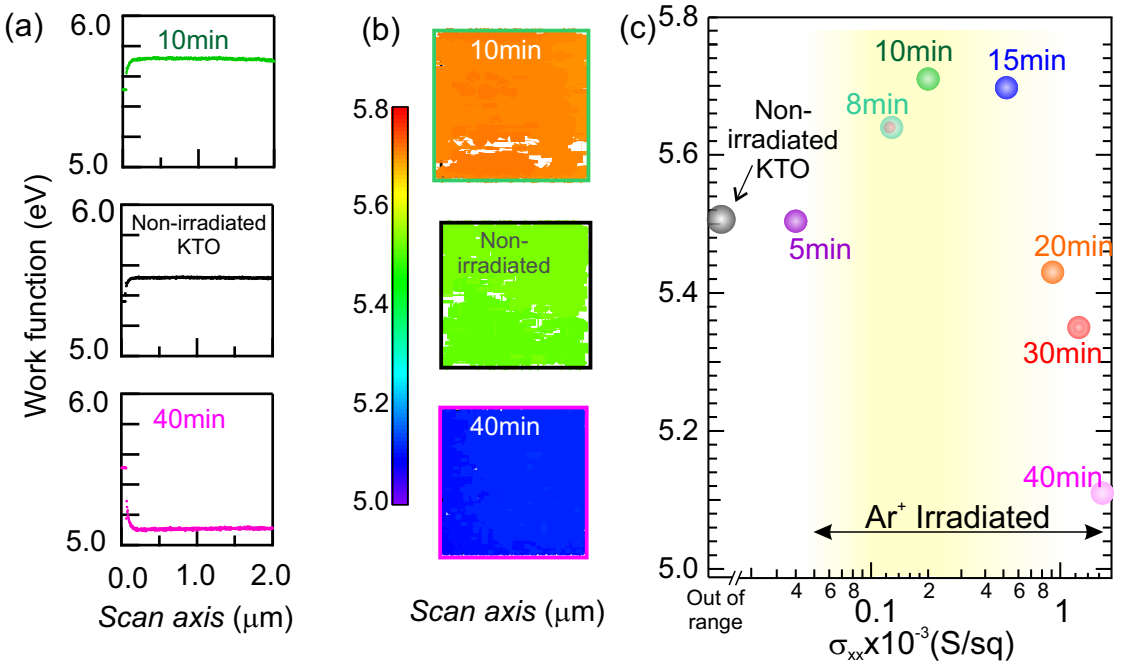

Figure 3.8: (a) The average work function of the non-irradiated, 10 minutes and 40 minutes irradiated samples as a function of scan length. (b) The contour plots of work function of non-irradiated, 10 minutes and 40 minutes irradiated samples. The color bar below indicates the work function in eV. (c) Work function of KTO single crystals as a function of sheet conductance at room temperature measured by KPFM.

3.3.1 Optical Spectroscopy- band gap calculation

Then to know the change in band gap with oxygen vacancies, we performed optical spectroscopy on all the samples using Agilent Carry UV-Vis-NIR spectrometer. Transmission spectra in **Fig. 3.7(a)** show percentage decrease in the transmission of light on increasing the irradiation time, indicating the increase in free charge carriers in the system. It was also observed from the transmission spectra that there were roughly two regions of percentage transmission. Upto 10 minutes of irradiation, change in the percentage transmission is small while there is a sudden change after that. Similar behavior was observed in case of optical band gap. Optical band was estimated from the tangent of (absorption x incident photon energy)^2 curve as a function of incident photon energy (hν) (**Fig. 3.7(b)**). In **Fig. 3.7(c)**, we plotted band gap as a function of sheet conductivity that also indicates two irradiation regions: slightly irradiated (upto 10 minutes) and heavily irradiated (above 10 minutes) respectively. From this observation, we inferred that during initial irradiation process, free charge carriers are generated that increase the absorption of photons even with lower energies. Further bombardment generates electronic states at the conduction band edge, decreasing the band gap.

3.3.2 Kelvin Probe Force Microscopy- work function calculation

To estimate the overall changes in the surface potential upon bombardment for different duration of time, Kelvin Probe Force Microscope (KPFM) was performed using Bruker Multimode 8 AFM.[14, 15, 16] For KPFM, we used a conducting tip (SCIM-PIT) and calibrated its work function using gold as the standard sample whose work function is known to be 5.1 eV. On knowing the work function of the tip, we measured the contact potential difference (CPD) between the tip and the samples. The work function of the tip and the CPD were then used to calculate the work function of our samples. The contour plots of work function of non-irradiated, 10 and 40 minutes irradiated samples for 2μm x 2μm region are shown in **Fig. 3.8(b)**. The color bar indicates the work function of the samples. The average work function of these samples along the scan length are shown in **Fig. 3.8(a)**. A non-monotonic change in the work function of the irradiated KTO samples was observed as a function of conductivity vis-a-vis irradiation time as depicted in **Fig. 3.8**. The expected decrease in the work function for an electron doped system was preceded

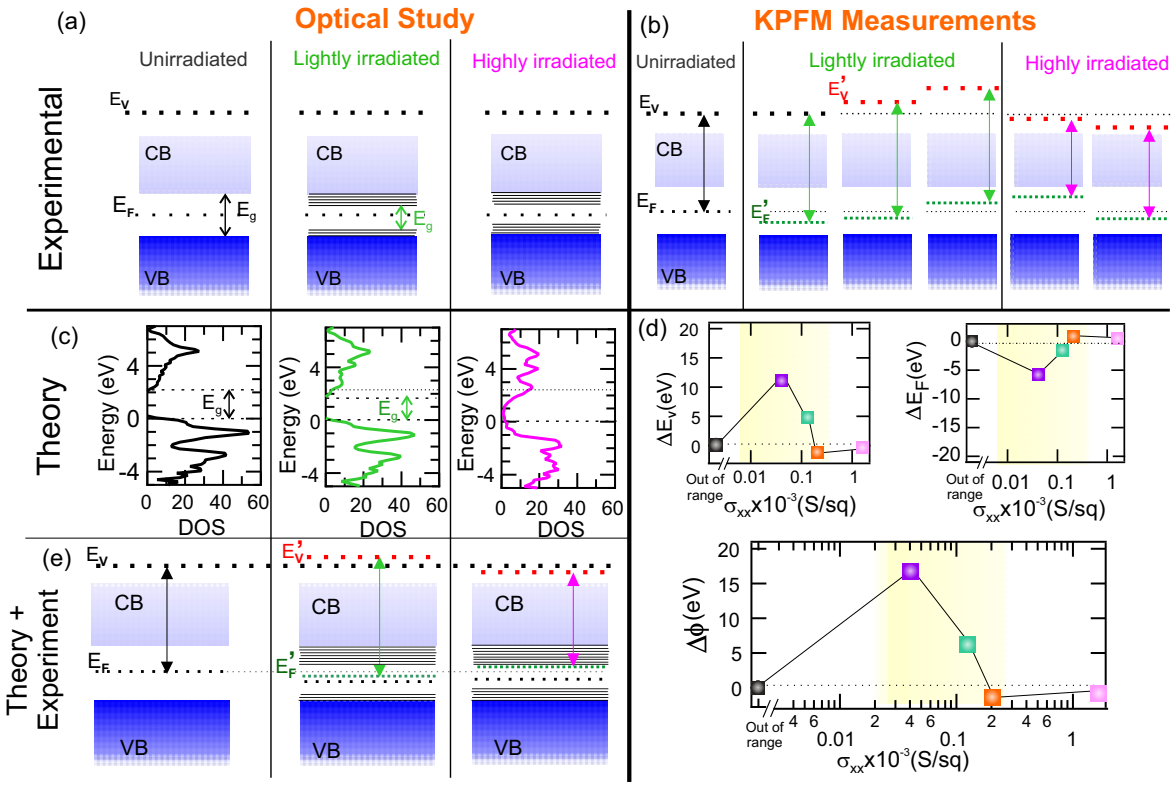

Figure 3.9: (a) and (b) Depiction of possible band structure modifications taking place according to experimental optical spectroscopy and KPFM measurements respectively. (c) DOS of unirradiated (left), lightly irradiated (middle) and highly irradiated (right) KTO calculated from first-principles DFT calculations. (d) Change in vacuum level (top left), fermi level (top right) and work function (bottom) calculated from surface potential calculations by including the oxygen vacancies. (e) Band diagrams for unirradiated, lightly and highly irradiated samples obtained by combining experimental observations and theoretical calculations.

by an initial increase in it, suggesting possibility of two kind of charge carriers (electrons and holes) in the system. To verify this, Hall measurements were done using Quantum Design Physical Property Measurement System (PPMS). Linear curves of Hall resistance as a function of magnetic field in **Fig. 3.6(b)**, however, clarified the existence of only one type of charge carriers. Similar to optical data, two distinct regions were seen in KPFM plot. Upto 10 minutes of bombardment, there was an anomalous increase in work function while above 10 minutes, work function monotonically decreased as expected. All the measurements on bombarded samples

were done immediately after bombardment to avoid ageing effect.

Figure 3.9(a) and **(b)** show the cartoon depiction of the possible band structure modifications taking place according to the experimental results. **Figure 3.9(a)** shows the band diagrams for the unirradiated, lightly irradiated and highly irradiated KTO samples where the band gap decreases on increasing the bombardment time. Optical property measurements shown in Fig. 3.7(c) suggest that with short irradiation time there is a small change in band gap, followed by a sharp decrease in it with further increase in irradiation time. Accordingly, our middle band diagram (**Fig. 3.9(a)**) mimic this situation through the introduction of defect states between conduction band and valence band. **Figure 3.9(b)** shows the possible band line-up of the unirradiated and irradiated samples based on our KPFM observations. **Figure 3.9(b)** (middle) shows several possible band structure reconstructions that can explain the increase in work function as we have seen for lightly irradiated samples. We have shown three most probable scenarios (i) movement of fermi level (E_F) towards valence band (VB) with no change in vacuum level (E_V) (ii) movement of E_F towards VB as well as movement of E_V away from conduction band (CB) and (iii) movement of E_F towards the CB accompanied by a larger shift of E_V away from the CB. For highly irradiated samples we have presented two of the possible cases where we show that the decrease in work function can be due to (i) movement of E_F towards CB accompanied by shifting of E_V downwards or (ii) movement of E_F towards the VB along with a larger downward shift of E_V.

3.3.3 DFT based theoretical band structure calculations

To identify the band structure as a function of oxygen vacancies out of these several possible combinations, DFT based theoretical band structure calculations have been performed.[17, 18, 19, 20] Here, we used Perdew-Burke-Ernzerhof (PBE) [21] exchange-correlation functional and projector augmented wave (PAW) basis set as implemented in Vienna Ab initio Simulation Package (VASP) [22, 23] to calculate DOS and work function of the KTO slab. For the bulk cubic unit cell of the KTO, $4 \times 4 \times 4$ Gamma centered K- mesh was used. The surface of KTO was constructed as $2D$ slab by considering periodic boundary condition along x and y directions and a 20 A^o vacuum region separating two repeating regions along z (001) direction. 2D slab geometry of thickness 15.9 A^o was created with 2x2x4 supercell of 80 atoms. The (001) surface of KTO was studied in this present calculation. For oxygen vacancy calculation, 4.1%, 20.8%, 37.9% and 50% of oxygen vacancy was

created in the supercell. It was found that oxygen vacancy created electron donating point defect in the structure (**Fig. 3.9(c)**). **Figure 3.9(c)** shows DOS for unbombarded (no oxygen vacancies), slightly (4.1% oxygen vacancies) and heavily (20.8% oxygen vacancies) bombarded systems. This figure suggests the DOS as well as band gap remain similar (very small reduction) with slight bombardment in comparison to unbombarded system where as the band gap significantly collapses for heavily bombarded system. This calculation further strengthened our claims based on experimental (optical) observations.

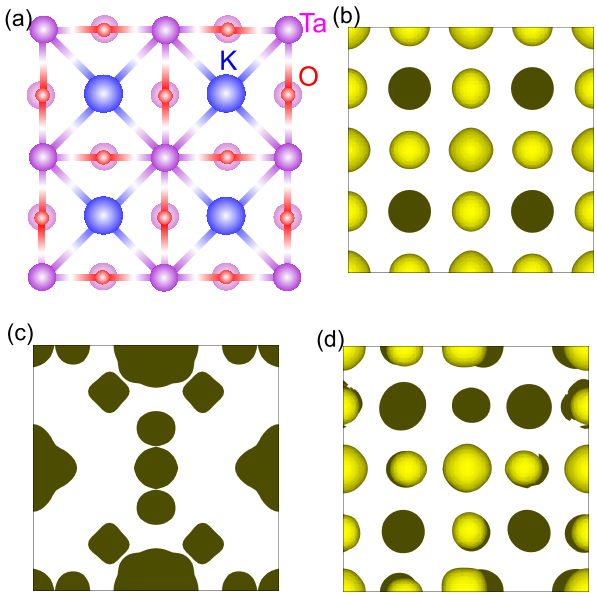

Figure 3.10: (a) Top view of (0 0 1) surface of KTO. (b), (c) and (d) present the electronic charge distribution of unirradiated, lightly irradiated and highly irradiated KTO samples respectively, where yellow color represents positive and dark green represents negative charge.

To understand the non-monotonic behavior of the work function ($\phi = E_V - E_F$) as a function of oxygen vacancies and identify the possible band line-up out of several possibilities shown in **Fig. 3.9(b)**, we have theoretically calculated change in vacuum level (ΔE_V), fermi level (ΔE_F) and work function ($\Delta\phi$) as a function of oxygen vacancy (**Fig. 3.9(d)**). These values were extracted from the theoretical calculations performed on 2D KTO slab. We considered a finite thickness of 2D KTO for the work function and vacuum level calculations. Due to this finite size, there might be a quantum size effect error.[24] These calculations showed a significant effect of surface dipoles with oxygen vacancies, leading to an anomalous

change in vacuum level as well as fermi level. The work function extracted from the calculations as a function of oxygen vacancy showed qualitatively very similar non-monotonic behavior (**Fig. 3.9(d)**) as observed experimentally. Combining all the results of theoretical simulations with our experimental observations, we proposed the band line-up of lightly and heavily irradiated samples in **Fig. 3.9(e)**. Upon light bombardment, E_F moves downwards due to formation of localized defect states near CB and band gap modifications. Also, there is an upward shift in E_V due to surface reconstruction. In case of highly bombarded samples, there is an upward movement of E_F indicating n-type of charge carriers in the system and E_V also moves slightly downwards as shown in **Fig. 3.9(e)**.

To further investigate this non-trivial behavior in work function, we also plotted charge density isosurface (**Fig. 3.10**). **Figure 3.10(a)** shows the top view of (0 0 1) surface of KTO and **Fig. 3.10(b, c, d)** represents the charge density of pure KTO slab, 4.1% oxygen vacant and 20.8% oxygen vacant slab. The yellow and green color isosurface correspond to positive and negative values, respectively. An interesting pattern was found in charge density plot for these vacancies. In pure slab, charge density was equivalently distributed on all surface atoms. For the 4.1% vacancy, positive charge was completely depleted and charge density was very localized. However, positive charge isosurface had a strong presence on 20.8% oxygen vacant slab (**Fig. 3.10(d)**) and the charge distribution was very similar to the unbombarded KTO slab. Depletion of charge density at 4.1% vacancy, increases the dipole moment of the surface and plausibly the high dipole moment plays a crucial role to increase the vacuum potential and hence, work function at low percentage vacancy. While smoothing of electron charge density for higher percentage vacancy decrease dipole moment, hence work function.[25]

3.4 Conclusion

In conclusion, we realized single terminated steps and terraces surface of KTO (001) oriented substrates, by using high temperature annealing followed by hot DI water etching. The technique is non-corrosive and results in uniform steps throughout the sample surface. Also, we prepared oxygen vacant electron doped conducting surface of KTO via Ar^+ irradiation. Density functional theory indicates that these conduction electrons have Ta $5d$ character and could be a good hunting ground for Rashba effect and other emergent phenomena. Optical spectroscopy along with

KPFM measurement clearly indicates two distinct effects of irradiation, where in the initial slight irradiation process (upto 10 minutes in our case), a small change in band gap with an anomalous change in work function was observed. Longer exposure to Ar^+ produces sharp decrease in band gap with a usual monotonic decrease in work function as a function of increasing irradiation time vis-a-vis charge carrier density. DFT calculations suggest a significant effect of surface dipole and modification of electronic DOS specially a non-trivial change in vacuum level due to oxygen vacancies upon Ar^+ irradiation.

Bibliography

[1] M. Kawasaki, K. Takahashi, T. Maeda, R. Tsuchiya, M. Shinohara, O. Ishiyama, T. Yonezawa, M. Yoshimoto and H. Koinuma, *Science*, **266**, 1540 (1994).

[2] H.J. Bae, J. Sigman, D.P. Norton, L.A. Boatner *App. Surf. Sci.*, **241**, 271 (2005).

[3] T.G. Le, *Mater. Sci. Appl.*, **6**, 533 (2015).

[4] R.A. Lukaszew, V. Stoica, C. Uher and R. Clarke, *Appl. Surf. Sci.*, **2019**, 74 (2003).

[5] M. Lippmaa, N. Nakagawa, M. Kawasaki, S. Ohashi, H. Koinuma, *Appl. Phys. Lett.*, **76**, 2439 (2000).

[6] H. Calderon and H. Hochst, *Phys. Rev. B*, **27**, 4961 (1983).

[7] M.G. Lagally, *Opt. Mater. Exp.*, **22**, 237 (1995).

[8] V. E. Henrich, G. Dresselhaus, and H. J. Zeiger *Phys. Rev. B*, **17**, 4908 (1978).

[9] S. Harashima, C. Bell, M. Kim, T. Yajima, Y. Hikita, and H. Y. Hwang, *Phys. Rev. B*, **88**, 085102 (2013).

[10] T. Ando, A. B. Fowler, and F. Stern, *Rev. Mod. Phys.*, **54**, 437 (1982).

[11] B. G. Streetman and S. K. Banerjee, *Solid State Electronic Devices*, 6th ed. (Phi Learning Private, New Delhi, India) (2009).

[12] D. W. Reagor and V. Y. Butko, *Nat. Mater.*, **4**, 593 (2005).

[13] F. V. E. Hensling, C. Xu, F. Gunkel, and R. Dittmann, *Sci. Rep.*, **7**, 39953, (2017).

[14] W. Melitz, J. Shen, A. C. Kummel, and S. Lee, *Surf. Sci. Rep.*, **66**, 1 (2011).

[15] C. Maragliano, S. Lilliu, M. S. Dahlem, M. Chiesa, T. Souier and M. Stefancich, *Sci. Rep.*, **4**, 4203 (2014).

[16] A. K. Henning, T. Hochwitz, J. Slinkman, J. Never, S. Hoffmann, P. Kaszuba, and C. Daghlian, *J. Appl.Phys.* , **77**, 1888 (1995).

[17] B. J. Morgan and G. W. Watson, *Surf. Sci.*, **601**, 5034 (2007).

[18] J. A. Enterkin, A. K. Subramanian, B. C. Russell,M. R. Castell, K. R. Poeppelmeier, and L. D. Marks, *Nat. Mater.*, **9**, 245 (2010).

[19] M. Nolan, S. Grigoleit, D. C. Sayle, S. C. Parker, and G. W. Watson, *Sur. Sci.*, **76**, 217 (2005).

[20] G. Henkelman, B. P. Uberuaga, D. J. Harris, J. H. Harding, and N. L. Allan, *Phys. Rev. B*, **72**, 115437 (2005).

[21] J. P. Perdew, K. Burke, and M. Ernzerhof, *Phys. Rev. Lett.*, **77**, 3865 (2010).

[22] P. E. Blochl, *Phys. Rev. B.*, **50**, 17953 (1994).

[23] G. Kresse and D. Joubert, *Phys. Rev. B.*, **59**, 1758 (1999).

[24] C. J. Fall, N. Binggeli, and A. Baldereschi, *J. Phys.:Condens. Matter*, **11**, 2689 (1999).

[25] A. J. Bennett and C. B. Duke, *Phys. Rev.*, **188**, 1060 (1969).

Chapter 4

Two dimensional electron gas at the polar-polar interface of insulating oxides $LaVO_3$ and $KTaO_3$

4.1 Introduction

In recent times, the urge of attaining new functionalities in modern electronic devices has led to the manipulation of spin degree of freedom of an electron along with its charge.[1, 2] This has given rise to an altogether new field of spin-electronics or "spintronics". It has been realized that momentum dependent splitting of spin-bands in an electronic system, the "Rashba effect", might play a key role in spintronic devices.[3, 4, 5] The Rashba effect is important not only because it might have tremendous potential for technical applications, but also because it is a hunting ground of emergent physical properties.[6, 7, 8, 9, 10, 11, 12, 13, 14]

Semiconducting materials such as heterostructures of GaAs/GaAlAs and InAs/InGaAs have already been explored for the manifestation of the Rashba effect.[15, 16] As discussed in chapter 1, another potentially rewarding class of materials for realization of this effect is "oxides".[17, 18] The benefit of using oxides for spin based electronic devices is that they manifest a wealth of functional properties

like magnetoresistance, superconductivity, ferromagnetism, ferroelectricity, charge ordering etc. which can be coupled with the Rashba effect to achieve emergent phenomena if a suitable interface or superlattice is designed.[19, 20, 21, 22] In addition to this, simple cubic structure of perovskite oxides makes them easily usable for fabrication of heterostructures for device applications.[17] Also, in recent times oxide thin films and interfaces with strong spin-orbit coupling are predicted to exhibit topological phases owing to their non-trivial spin-structures and electronic states which may add further dimensions to the field of "oxide spintronics".[23]

So with the aim of realizing Rashba spin-splitting in oxides and explore its rich physics for fundamental and device applications, we fabricated an epitaxial heterostructure of two perovskite oxides of LVO and KTO. LVO is a $3d$ Mott-insulator and KTO is a $5d$ band insulator. However, the strong spin-orbit coupling of KTO makes it a potential candidate for realization of Rashba spin-splitting.[24, 25] In this chapter, we show the emergence of conductivity at the heterointerface of these insulating oxides when the film thickness is more than 3 monolayers (ml). We performed a detailed thickness dependent study of the electrical properties of the heterostructure by varying the LVO film thickness. A reasonably high carrier mobility of around 600 $cm^2V^{-1}s^{-1}$ was measured at the interface with varying thickness of the LVO film. The fabrication of the two dimensional conducting channel at the interface of LVO-KTO oxide heterostructure along with the structural and electrical transport properties is discussed in this chapter.

4.2 Experimental Details

4.2.1 LVO thin film growth

Thin films of LVO were grown on (001) oriented Ta-terminated KTO single crystals. For Ta-termination, method of high temperature annealing followed by DI water etching was employed as discussed in the last chapter.[26] The KTO (001) single crystals were annealed at an optimized temperature of 650^{o}C for two hours in air under ambient conditions. Two substrates were annealed at one time with one kept upside down at the top of other with a gap of 60 μm using two sapphires on the sides. This was done to avoid K vacancies. To anneal, the substrates the ramp rate was kept 300^{o}C/hour while heating and it was kept 250 ^{o}C/hour while cooling down to room temperature. The annealing accumulated KO particles on the surface of

the substrate which were removed by etching with deionised (DI) water heated at 60^{o}C giving us TaO_2 terminated step and terrace like structure.

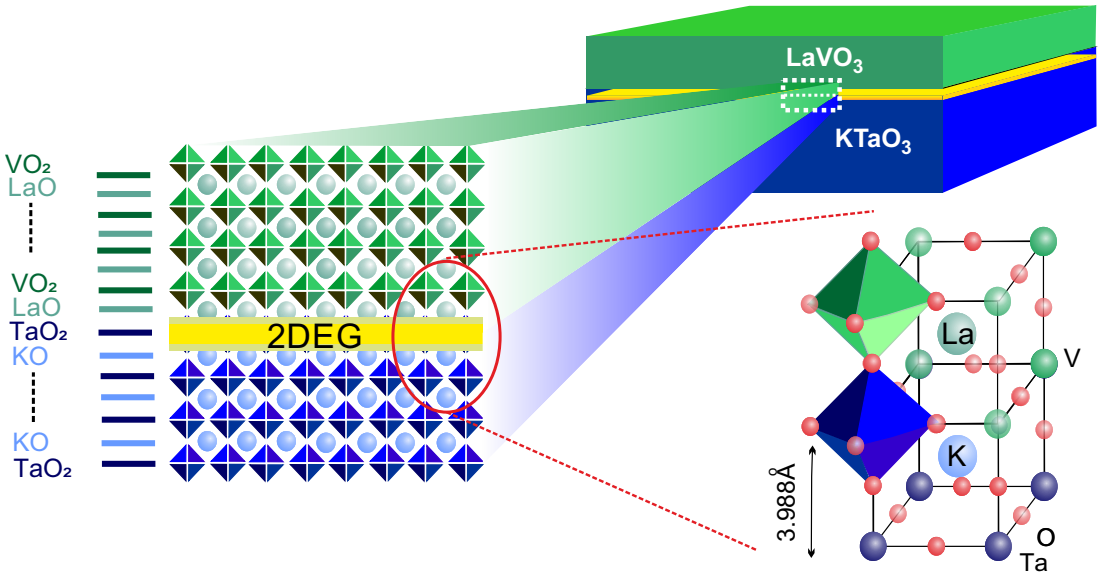

Figure 4.1: Schematic of LVO-KTO heterostructure.

Then, the thin films of LVO were grown on the Ta-terminated KTO substrates using PLD. Various growth conditions like the substrate temperature, oxygen partial pressure and laser fluence were optimized. Firstly, we identified the substrate heating temperature to be 600^{o}C. This was influenced by the fact that there were chances of K vacancies at higher temperatures. As heating of the substrate and its bombardment with the ablated species of the target material can cause oxygen vacancies, a partial pressure of oxygen is to be maintained in the deposition chamber during growth. We chose the oxygen partial pressure of $\sim$1x10^{-6} using the previous optimized results for LVO-STO system and keeping in mind the tendency of formation of $LaVO_4$ at higher oxygen partial pressures.[27, 28, 29] Then keeping the substrate temperature and oxygen partial pressure constant, we varied the laser fluence from 0.6 J cm^{-2} to 4 J cm^{-2}. It was found that all the samples grown above 1 J cm^{-2} laser fluence were conducting. But the mobility value was maximum for the laser fluence value of 4 J cm^{-2}. So we chose 4 J cm^{-2} as the laser fluence for our thickness dependent study. LVO films of different thickness were grown at these optimized conditions. **Fig. 4.1** shows the schematic of the LVO-KTO heterostructure. The thickness of the films was controlled using reflection high-energy electron diffraction (RHEED) technique. The RHEED oscillations of the specular spot, for 10 ml, 8 ml, 4 ml sample, as a function of number of unit cells are shown in **Fig.**

4.2(a). **Figure 4.2(a)** right panel shows the RHEED pattern of the 10 ml sample before and after the film growth. The RHEED oscillations and the RHEED pattern clearly shows the layer-by-layer growth of the LVO films.

4.2.2 Structural analysis

Further structural analysis of the thin films was done using X-ray diffractometer (XRD) (Bruker, Discover 8). **Figure 4.2(b)** shows the XRD plot of 40 ml sample. LVO film (001) and (002) peaks can be clearly seen along with the substrate peaks suggesting crystalline growth of the film over the substrate. In addition to this the presence of Laue fringes further determines the quality of the growth. Inset of **Fig. 4.2(b)** shows the rocking curve of the KTO substrate depicting the high quality and crystallinity of the sample.

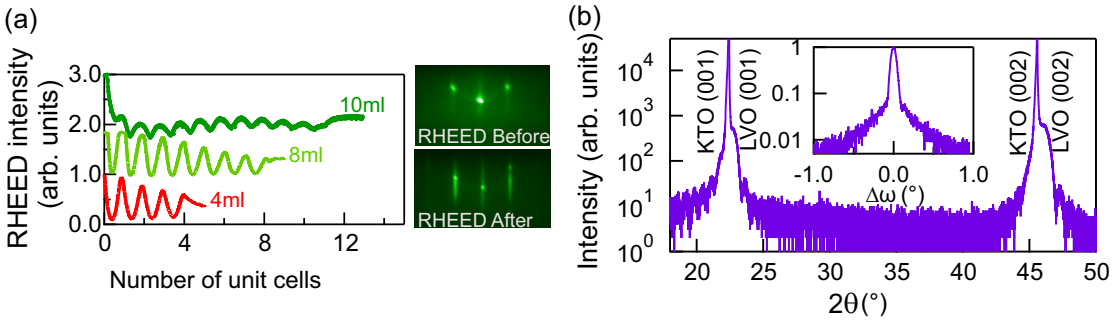

Figure 4.2: (a) RHEED oscillations for 4, 8 and 10 ml LVO-KTO samples and RHEED pattern for 10 ml sample before and after growth of LVO film. (b) X-ray diffraction pattern of 40 ml sample showing crystalline film growth of LVO on KTO.

4.2.3 Film oxidation states

As vanadium (V) can have multiple valence states and a small change in the doping electrons can modify the V spin states, we performed X-ray photoelectron spectroscopy (XPS) measurement on the freshly prepared LVO thin films to know the oxidation states of V. XPS measurement of the core level spectrum were carried out with a non-monochromatic Mg K_α x-ray source having photon energy 1253.6 eV, the hemispherical analyzer operated at a constant pass energy of 20 eV and the pressure of analyzing chamber was maintained at $\approx$ 1x10^{-9} mbar throughout

the measurement. All the spectra obtained were calibrated to a C 1s peak at 284.2 eV.[30]

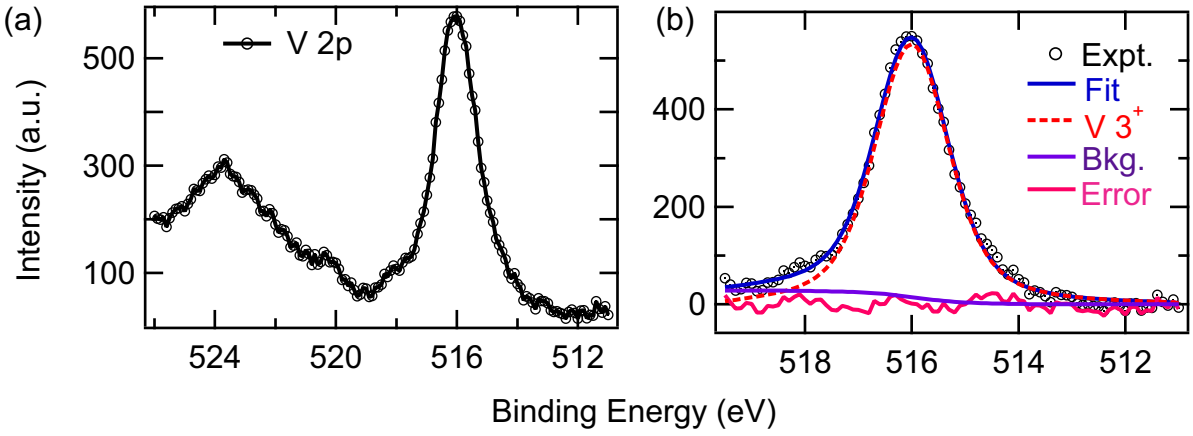

Figure 4.3: (a) Core level X-ray photoemission spectrum of V 2p collected with Mg K_α x-ray source having 1253.6 eV photon energy (b) Fitting of V $2p_{3/2}$ peak using the convoluted function (Lorentzian function convoluted with Gaussian function).

Core level XPS spectrum of LVO thin film is shown in **Fig. 4.3(a)**, where the obtained binding energy (BE) curve of V 2p core level depict the two peaks corresponding to V $2p_{3/2}$ and V $2p_{1/2}$ at 516.0 and 523.6 eV BE respectively. As we used the non-monochromatic Mg K_α x-ray source, this always gives Mg $K_{\alpha 3,4}$ signal in XPS spectrum which needs to be subtracted from raw data. The spectrum shown in the **Fig. 4.3(a)** is Mg $K_{\alpha 3,4}$ signal subtracted spectrum from the raw data of V 2p core level. There are several reports available in the literature for XPS peak position of the V^{3+} species ranging from 515.15 eV to 516.3 eV [31, 32, 33, 34] and our result fall well within the reported range. We have further analysed V $2p_{3/2}$ core level spectrum by fitting it with the convoluted function. The shape of peak is defined by a Lorentzian function convoluted by a Gaussian function with full width at half maximum (FWHM) representing the lifetime and resolution broadening respectively. In the **Fig. 4.3(b)**, fitting of the V $2p_{3/2}$ peak is shown, where black open circles are the experimental data, blue solid line is the fitted spectrum, red dashed line is V^{3+} contribution in the spectrum, magenta solid line shows the error in the fitting and the violet solid line depicts the Shirley background used for the background subtraction. We have deliberately omitted the V $2p_{1/2}$ part while fitting, since V $2p_{1/2}$ peak overlaps with tail part of the O 1s peak and that makes the fitting of whole V 2p spectrum more complicated. As shown in the **Fig. 4.3(b)**, V $2p_{3/2}$ peak is fitted well with a single peak and this confirms the presence of the single

valence state of V^{3+}.

Hence, combining XRD, RHEED and XPS measurements we confirmed that high quality LVO films were epitaxially formed on the KTO substrate.

4.2.4 Transport measurements

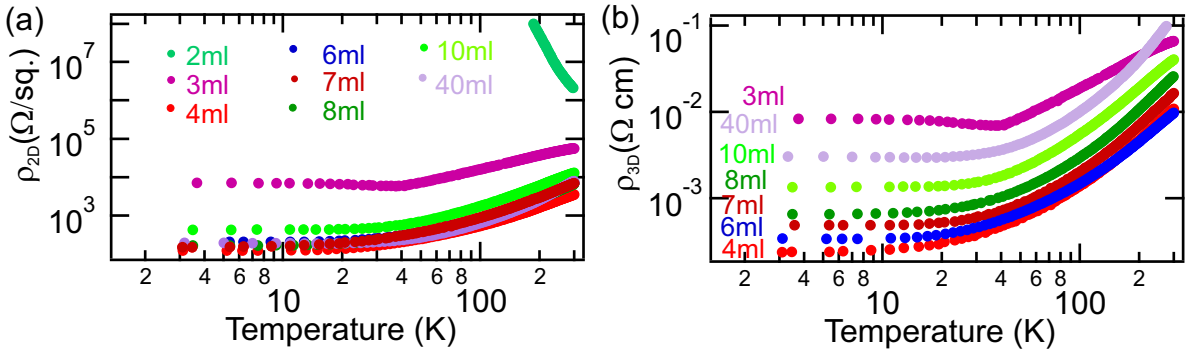

Figure 4.4: (a) Temperature dependent 2D resistivity and (b) 3D resistivity for LVO-KTO samples with varying LVO thickness.

Next, to check whether we heterostructure formed was conducting, we performed temperature dependent resistivity measurements using PPMS by Quantum Design as discussed in chapter 2. The temperature dependent resistivity measurements were done for different samples of varying thickness. **Figure 4.4** shows the temperature dependent resistivity for all the samples, where panel (a) shows the two dimensional resistivity (ρ_{2D}) for conduction parallel to the interface and panel (b) shows the three dimensional resistivity (ρ_{3D}) normalized by the film thickness. It was found that the sample having LVO thickness 2 ml was insulating. The 3 ml sample although conducting at room temperature exhibited an upturn near 30 K. All other samples with LVO thickness more than 3 ml were conducting down to 1.8 K. In contrast to the wide range of values found for (ρ_{3D}), the same data plotted as (ρ_{2D}) showed that the data for all conducting samples essentially collapsed to a narrow range of (ρ_{2D}) values. This was in accordance with the electronic reconstruction phenomena of formation of 2DEG at the oxide heterointerface and was an evidence that LVO films itself were insulating and that only the interface formed the conducting channel.[35]. In addition to this, for further confirmation, we deposited LVO film on one half of the substrate by covering the other half with a hard mask inside the PLD deposition chamber. Then after the growth, to know about the

origin of conductivity, the resistance was measured in three different configurations as shown in **Fig. 4.5**. In the first configuration (**Fig. 4.5(a)**) the resistance of the LVO film was measured by making electrical connections at the top of LVO film surface using silver paint and at the interface by ultrasonically wire-bonding the Al wire. In the second configuration (**Fig. 4.5(b)**), the resistance across the interface was measured by making all electrical connections at the interface using wire bonder. In the third configuration, all the electrical contacts were made on the bare KTO substrate part to know the resistance of the substrate (**Fig. 4.5(c)**). It was found that out of the three cases only interface was conducting. Neither the film nor the substrate was conducting individually. This confirmed that the origin of conductivity was formation of interfacial two dimensional electron gas only and not oxygen vacancies formed in the film or the substrate.

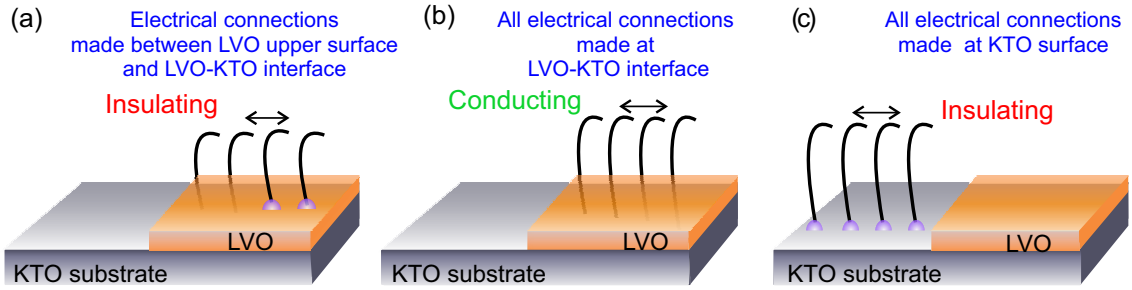

Figure 4.5: Schematic of connection geometry for measuring resistance (a) across the LVO thin film (b) at the LVO-KTO interface (c) at the KTO substrate.

After confirming the conductivity of the interface, we performed Hall measurements on all the samples to calculate the charge carrier density and mobility of the samples. **Figure 4.6** shows the Hall resistance of all the samples as a function of magnetic field at 1.8 K. The linear dependence of Hall resistance showed that the interface had only single type of charge carriers. Charge carrier density was then calculated from these measurements. **Figure 4.7(a)** and **(b)** shows the charge carrier density and mobility, for the conducting samples, calculated at 300 K and 1.8 K. It can be seen that above 3 ml of LVO, once the interface becomes conducting, the charge carrier density and mobility are independent of LVO thickness. This was again in accordance with the electronic reconstruction mechanism for formation of 2DEG where after achieving the critical thickness to avoid polar catastrophe, increasing the thickness of the film does not add further carriers at the interface.[28, 35] **Figure 4.7(a)** inset shows the Hall resistance of 4 ml LVO-KTO. We obtained carrier mobility of around 600 $cm^2V^{-1}s^{-1}$ at 1.8 K in our samples as

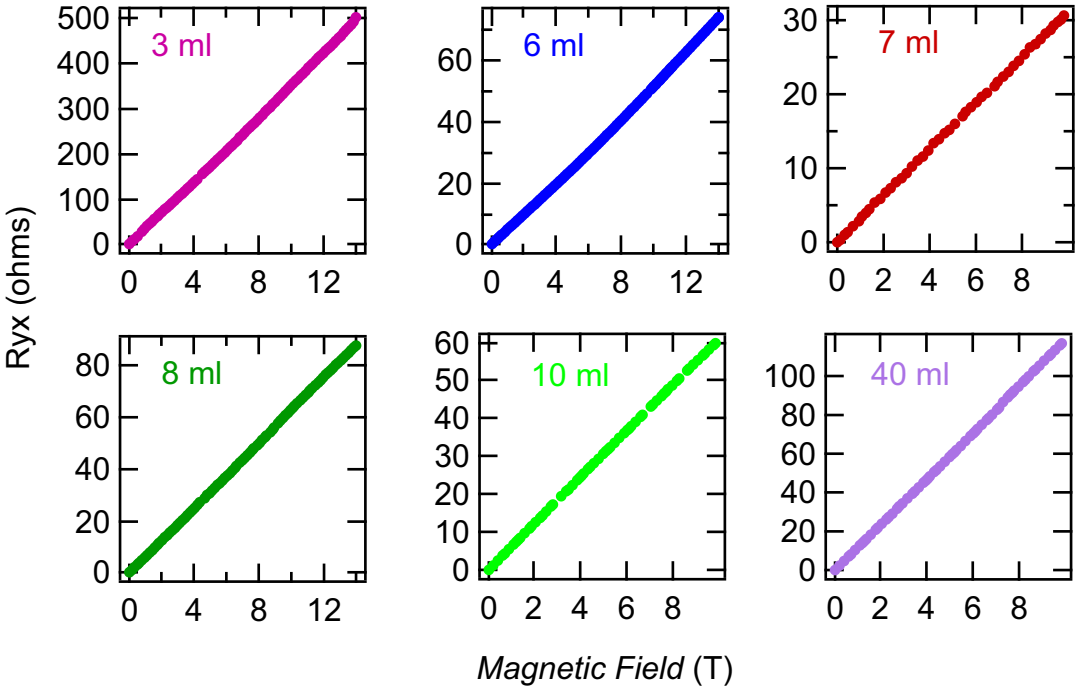

Figure 4.6: Hall resistance for all the samples measured at 1.8 K. The linear dependence of Hall resistance suggests single type of carriers in the system.

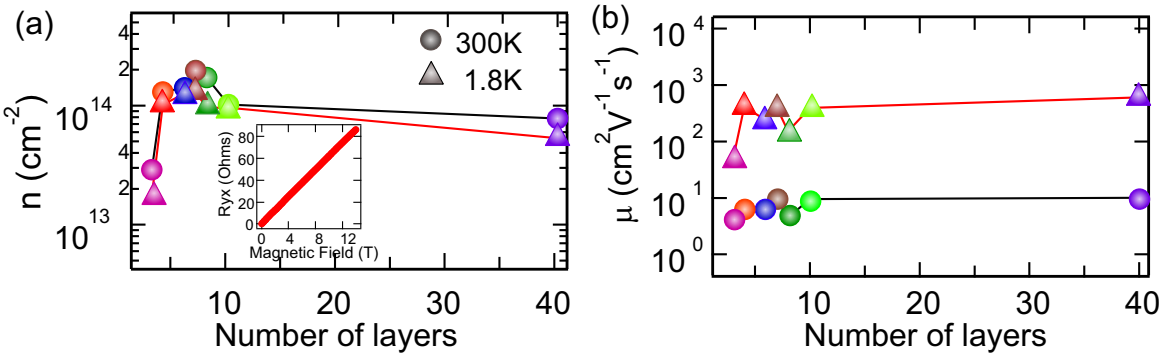

Figure 4.7: (a) Charge carrier density and (b) mobility of all the samples measured at 300 K and 1.8 K. Inset of (a) shows the Hall data for 4 ml sample at 1.8 K.

shown in **Fig. 4.7(b)**.

4.3 Conclusion

In conclusion, we realized a high quality thin film new interface of two polar-polar perovskite oxides LVO and KTO. The heterostructure made out of two insulating oxides was found to be conducting showing realization of 2DEG at the interface. The linear Hall resistance of all samples depicted presence of single type of charge carriers and a fairly high mobility of around 600 $cm^2V^{-1}s^{-1}$ was observed at this new heterointerface. The high mobility 2DEG at the interface of heterostructure made of polar oxides having strong spin-orbit coupling and broken inversion symmetry are potential candidates for realization of Rashba type spin-splitting and can be extremely useful as a channel material of future generation spintronic devices. Such oxide heterostructures open up new opportunities in the field of oxide electronics and are a hunting ground for exploring rich physics.

Bibliography

[1] S. Datta, and B. Das, *Appl. Phys. Lett.*, **56**, 665 (1990).

[2] G. Meier, T. Matsuyama, and U. Merkt, *Phys. Rev. B*, **65**, 125327 (2002).

[3] Y.A. Bychkov and E.I. Rashba *JETP Lett.*, **39**, 78 (1984).

[4] G. Seibold, S. Caprara, M. Grilli, and R. Raimondi, *EPL*, **112**, 17004,(2015).

[5] J. Nitta, and T. Koga, *J. Supercond.*, **16**, 689 (2003).

[6] S. Hurand, J. Jouan, C. Feuillet-Palma, G. Singh, J. Biscaras, E. Lesne, N. Reyren, A. Barthelemy, M. Bibes, J.E. Villegas, C. Ulysse, X. Lafosse, A. Pannetier Lecoeur, S. Caprara, M. Grilli, J. Lesueur, and N. Bergeal, *Sci. Rep.*, **5**, 12751 (2015).

[7] J.I. Inoue, T. Kato, G.E.W. Bauer, and L.W. Molenkamp, *Semicond. Sci.Technol*, **24**, 064003 (2009).

[8] H. Murakawa, M.S. Bahramy, M. Tokunaga, Y. Kohama, C. Bell, Y. Kaneko, N. Nagaosa, H. Hwang, and Y. Tokura, *Science*, **342**, 1490 (2013).

[9] S. Caprara, *Nat. Mater.*, **15**, 1224 (2016).

[10] E. Lesne, Y. Fu, S. Oyarzun, J.C. Rojas-Sanchez, D.C. Vaz, H. Naganuma, G. Sicoli, J.P. Attane, E. Jacquet, J.M. George, A. Barthelemy, H. Jaffres, A. Fert, M. Bibes, and L. Vila, *Nat. Mater.*, **15**, 1261 (2016).

[11] G. Seibold, S. Caprara, M. Grilli, and R. Raimondi, *Phys. Rev. Lett.*, **119**, 256801 (2017).

[12] F. Zheng, L.Z. Tan, S. Liu, and M. Rappe, *Nano Lett.*, **15**, 7794 (2015).

[13] S.D. Stranks, and P. Plochocka, *Nat. Mater.*, **17**, 381 (2018).

[14] J. Puebla, F. Auvray, N. Yamaguchi, M. Xu, S.Z. Bisri, Y. Iwasa, F. Ishii, and Y. Otani, *Phys. Rev. Lett.*, **122**, 256501 (2019).

[15] J.P. Eisentein, H.L. Stormer, V. Narayanamurti, A.C. Gossard, and W. Wiegmann, *Phys. Rev. Lett.*, **53**, 2579 (1984).

[16] J. Nitta, H. Takayanagi, and T. Enoki, *Phys. Rev. Lett.*, **78**, 1335 (1997).

[17] M. Bibes, J.E. Villegas, and A. Barthelemy, *Advances in Physics*, **60(1)**, 5 (2011).

[18] K.V. Shanavas, Z.S. Popovic, and S. Satpathy, *Phys. Rev. B*, **90**, 165108 (2014).

[19] Y. Tokura, A. Urushibara, Y. Moritomo, T. Arima, A. Asamitsu, G. Kido, and N. Furukawa, *J. Phys. Soc. Jpn.*, **63**, 3931 (1994).

[20] J.F. Schooley, W.R. Hosier, and M.L. Cohen, *Phys. Rev. Lett.*, **12**, 474 (1964).

[21] O. Tikhomirov H. Jiang and J. Levy, *Phys. Rev. Lett.*, **89**, 147601 (2002).

[22] J.S. Lee, Y.W. Xie, H.K. Sato, C. Bell, Y. Hikita, H.Y. Hwang, and C.C. Kao, *Nat. Mater.*, **12**, 703 (2013).

[23] M. Uchida and M. Kawasaki, *J. Phys. D:Appl. Phys.*, **51**, 143001 (2018).

[24] K.V. Shanavas, and S. Satpathy, *Phys. Rev. Lett.*, **112**, 086802 (2014).

[25] H. Nakamura and T. Kimura *Phys. Rev. B*, **80**, 121308 (2009).

[26] R. Tomar, N. Wadehra, V. Budhiraja, B. Prakash, and S. Chakraverty, *Appl. Surf. Science*, **427**, 861 (2018).

[27] Y. Hotta, Y. Mukunoki, T. Susaki, H. Y. Hwang, L. Fitting, and D. A. Muller *App. Phys. Lett.*, **89**, 031918 (2006).

[28] Y. Hotta, T. Susaki, and H.Y. Hwang, *Phys. Rev. Lett.*, **99**, 236805 (2007).

[29] R. Tomar, R. M. Varma, N. Kumar, D. D. Sarma, D. Maryenko and S. Chakraverty, *Adv. Mater. Interfaces*, 1900941 (2019).

[30] Cardona M. and Ley L., *Eds. Photoemission in Solids I: General Principles (Springer- Verlag, Berlin)* (1978).

[31] Mendialdua J., Casanova R. and Barbaux Y., *J. Electron Spectrosc. Relat. Phenom.*, **71**, 249 (1995).

[32] Sawatzky G.A. and Post D., *Phys. Rev. B*, **20**, 1546 (1979).

[33] Maiti and Sarma D.D., *Phys. Rev. B*, **61(4)**, 2525 (2000).

[34] Hryha E., Rutqyist E. and Nyborg L., *Wiley Online Library, https://doi.org/10.1002/sia.3844* (2011).

[35] N. Nakagawa, H. Y. Hwang and D. A. Muller, *Nat. Materials*, **5**, 204 (2006).

Chapter 5

Planar Hall effect and anisotropic magnetoresistance in polar-polar interface of $LaVO_3$-$KTaO_3$ with strong spin-orbit coupling

5.1 Introduction

In the past, oxides have been used in conventional semiconductor technologies and devices. Materials like polycrystalline or amorphous oxide thin films with a large band gap have been widely used as capacitors and gate insulators etc. In recent decades, however, a number of emergent functionalities such as high temperature superconductivity, colossal magnetoresistance and multiferroics have been discovered. They attracted a great deal of attention for unique electronics applications along with emerging physics only realized in oxide materials. Strong electron correlation in charge, spin, and orbital degrees of freedom in correlated oxides is believed to be the origin of observation of such effects.

In condensed matter physics, more recently, the role of topology has become an area of intense research. It has led to the discovery of several new phenomena and multiple electronic phases opening up new fields to explore.[1] The term "topology" is used to describe or classify the properties maintained for a continuous deformation

in a given space. Thus, a topological state is intrinsically stable against any kind of perturbations favoring other states, producing novel functionalities which are suited for storing and processing information as a state variable. For example, in topological "insulators", where the bulk bands have non-trivial topology in momentum space, give rise to a symmetry protected "conductive" surface state.

In recent times, oxide thin films and interfaces with strong spin-orbit coupling are also predicted to exhibit topological phases owing to their non-trivial spin-structures and electronic states.[2, 3] Oxide systems having Rashba type spin-slitting are potential candidates for observation topological characteristics because of the presence of linear dispersion relation at the crossing point of two spin bands and hence, two spheres with spin arrangement having opposite chiralities. Anisotropic magnetoresistance (AMR) and planar Hall effect (PHE) which are relativistic magnetotransport phenomenon observed in magnetic systems have now also been observed in topological systems and give evidence of the topology of the system.[4, 5, 6, 7] Also, such phenomena are theoretically predicted in systems with the Rashba-Dresselhaus type spin-splitting.[8, 9] Experimental observation of such phenomena in oxide heterostructures and their theoretical understanding may add further dimensions to the field of "oxide spintronics".

So, after observing the emergence of electrical conductivity at the interface of insulating LVO and KTO, in this chapter we focus on the magnetotransport properties of the heterostructure. As spin-orbit coupling is an important parameter for the realization of Rashba effect, we calculate the spin-orbit coupling strength of LVO-KTO and show that it is the highest among all other perovskite oxide heterostructures reported so far. We also show topological chiral anomaly via observation of PHE and oscillations in longitudinal AMR in our LVO-KTO system. A theoretical modelling using Rashba spin-split energy spectrum could predict our observation of 2 fold oscillations in AMR and PHE at low applied magnetic fields. The appearance of an additional periodicity in AMR above 8 T magnetic field suggests a possible complex and rich physics arising from the interplay between chiral nature of the band structure, relativistic 2 dimensional itinerant electrons and strong spin-orbit coupling present in the system. We observe a B^2 dependence of AMR and PHE amplitudes which we are able to capture within our theoretical model.

5.2 Experimental Details

5.2.1 Out-of-plane magneto-transport measurements: Observation of weak antilocalization in magnetoresistance

We adopted weak antilocalization to probe spin-orbit coupling strength in our LVO-KTO system.[10, 11] Weak localization (WL) and weak antilocalization (WAL) are basically quantum interference phenomena of electrons. When the temperature is sufficiently low, constructive interference of electron waves results in an increased probability of back scattering events, leading to an extra resistivity added to the classical term. This is weak localization. Spin-orbit coupling however, allow the electron spin to flip, resulting in change of sign of the constructive interference to destructive one, and hence, a decrement in the resistivity. This is known as antilocalization.[11] Both the effects are destroyed when magnetic field is applied, yielding a negative magnetoresistance for WL and a positive magnetoresistance for WAL.[12] Therefore, WAL can be used as a sensitive probe of spin-orbit coupling. WAL has also been used to detect spin-orbit coupling in a wide range of systems from metals,[10] semiconductors[13, 14, 15], to graphene.[16]

For these measurements, we applied magnetic field normal to the sample plane carrying current as shown in **Fig. 5.1(a)** and measured the longitudinal resistance as a function of magnetic field. The contacts for these measurements were made by ultrasonically wire bonding aluminum wires on the 4 ml LVO-KTO sample. The low temperature (1.8 K) magnetoresistance measurements revealed the presence of strong spin-orbit coupling in the system. A sharp dip at 0 T with positive MR at low fields was observed in the MR data as shown in **Fig. 5.1(b)**. This is a signature of WAL and hence spin-orbit coupling present in the system.[11, 12] Theory has been developed by Iordanskii, Lyanda-Geller, and Pikus (ILP theory) to describe the weak-antilocalization in magnetoconductance for the materials with strong spin-orbit coupling. So we converted the MR data to magnetoconductance as shown in **Fig. 5.1(c)**. The expression of the magnetoconductance developed by ILP theory is given by [17, 18]

$$\Delta\sigma = \frac{e^2}{2\pi^2\hbar}[ln(\frac{B_\phi}{B}) - \psi(\frac{1}{2}+\frac{B_\phi}{B}) + ln(\frac{B_{SO}}{B}) - \psi(\frac{1}{2}+\frac{B_{SO}}{B}) - A_k\frac{\sigma_o}{G_o}B^2] \quad (5.1)$$

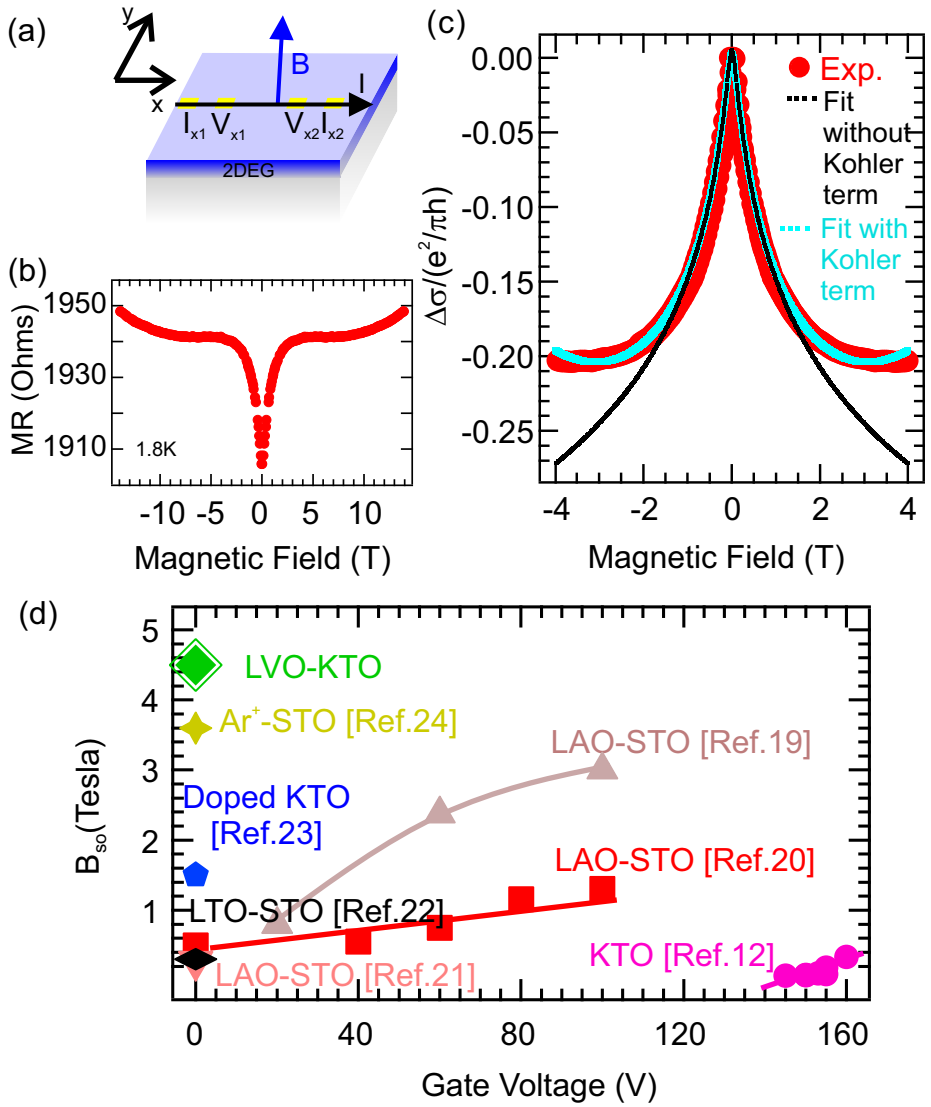

Figure 5.1: (a) Schematic of the connection geometry for magnetoresistance (R_{xx}) measurements for magnetic field applied out-of-plane. (b) Magnetoresistance plot of 4 ml sample as a function of magnetic field. (c) Magnetoconductance plot showing weak anti-localization due to high spin-orbit coupling along with the fitting done without the Kohler term (black line) and the fit including the Kohler term (cyan line). (d) Comparative plot of B_{SO} vs. gate voltage for STO and KTO based systems.

where, **B** is the applied magnetic field, B_ϕ ($\hbar/4el_\phi^2$) and B_{SO} ($\hbar/4el_{SO}^2$) are two characteristic magnetic fields related to phase coherence length (l_ϕ) and spin-precession length (l_{SO}), ψ is the digamma function and G_o ($e^2/\pi h$) is the quantum

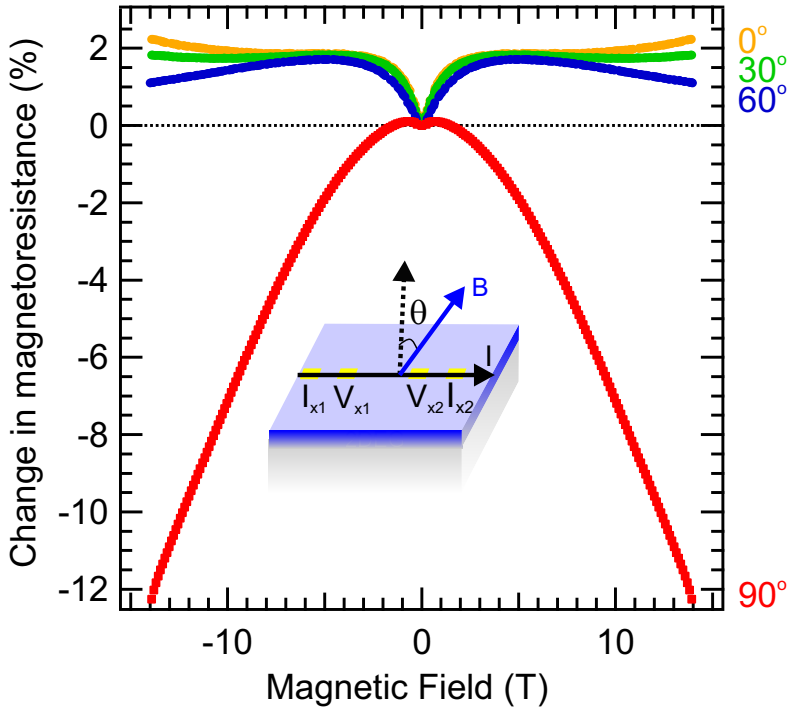

Figure 5.2: Magnetoresistance plot showing transition from positive to negative MR on varying the angle between the normal to the sample plane and magnetic field.

conductance. The ILP theory was derived for the magnetic field region $B < \hbar/2el_m^2$; where l_m is the mean free path of the carriers.[12, 17] For the present sample $\hbar/2el_m^2$ was estimated to be 0.3 T. However, we were able to fit our data upto 1 T as shown in **Fig. 5.1(c)** fitting with black line. The last term with Kohler coefficient A_k accounts for the orbital magnetoconductance having B^2 dependence. **Figure 5.1(c)** fit with cyan line shows the magnetoconductance data for 4 ml sample using full equation 1. A high value of $B_{SO} \sim 4.4$ T corresponding to a spin-precession length of 6 nm was obtained from the fitting. Phase coherence length of 70 nm and magnetic field strength corresponding to inelastic scattering B_ϕ=0.03 T was obtained for our system. These values of phase coherence length and B_ϕ were in excellent agreement with the previous report.[12]

Then we compared the spin-orbit coupling strength obtained in our case with that measured for other perovskite oxides. **Fig. 5.1(d)** shows the B_{SO} of STO and KTO based systems as a function of applied gate voltage from the literature compared with our sample.[12, 19, 20, 21, 22, 23, 24] The figure clearly suggests that our LVO-KTO interface had the highest B_{SO} among all reported STO and KTO systems.

Interesting results were obtained when we varied the angle between the normal to the plane and the magnetic field as shown in **Fig. 5.2**. We observed a transition from positive to negative MR when the magnetic field was landed in the plane of the sample carrying current. This kind of in-plane negative MR is usually observed in topological systems. This was strange for an all oxide system and indicated the presence of topological Rashba spin-split bands in our system.

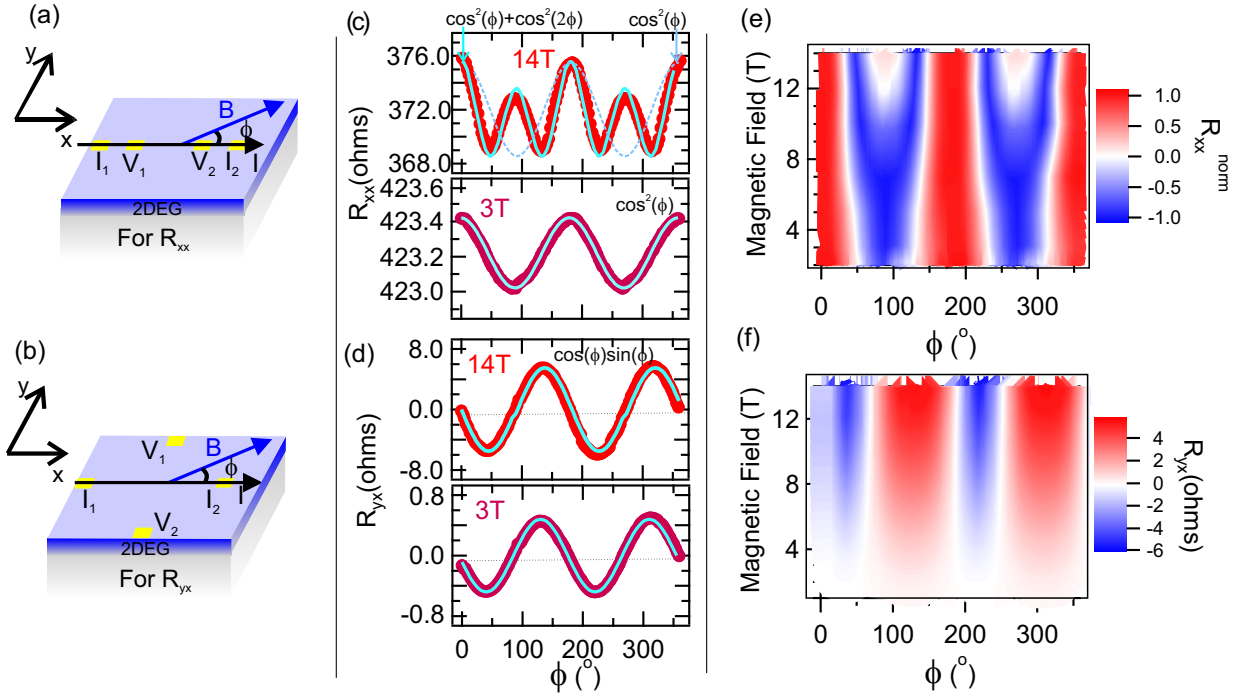

Figure 5.3: (a) and (b) Schematic of measurement geometry for R_{xx} and R_{yx} respectively wit magnetic field applied in the current carrying plane of the sample. (c) and (d) Angle dependent R_{xx} and R_{yx} measured at 1.8 K for 14 T and 3 T. Blue line is the fitted curve. (e) and (f) Applied magnetic field and angle dependent contour plots for normalized R_{xx} and R_{yx}.

5.2.2 In-plane magnetotransport measurements: Observation of planar Hall effect and anisotropic magnetoresistance

Next, we performed in-plane magnetoresistance measurements by applying magnetic field in the plane of the sample carrying current and measured the longitudinal and

transverse magnetoresistance as shown schematically in **Fig. 5.3(a)** and **(b)** respectively. Usually, PHE and AMR are observed in magnetic systems and are associated with the crystalline anisotropy of the system.[4, 5] Also, recently some topological systems have been reported to witness in-plane AMR and PHE [6, 7], the origin of which is anisotropic spin flip transition probabilities arising from broken time reversal symmetry. Theoretically, it has been predicted that the systems with the Rashba-Dressalhaus type of spin band splitting in presence of magnetic impurities may also exhibit in-plane AMR and PHE.[8, 9] Although theoretically predicted, experimental realization of such phenomena in the 2DEG systems with high spin-orbit interaction is not well explored. Considering the large spin-orbit coupling obtained for our system, we expected interesting in-plane AMR and PHE, as well as their evolution as a function of the applied magnetic field.

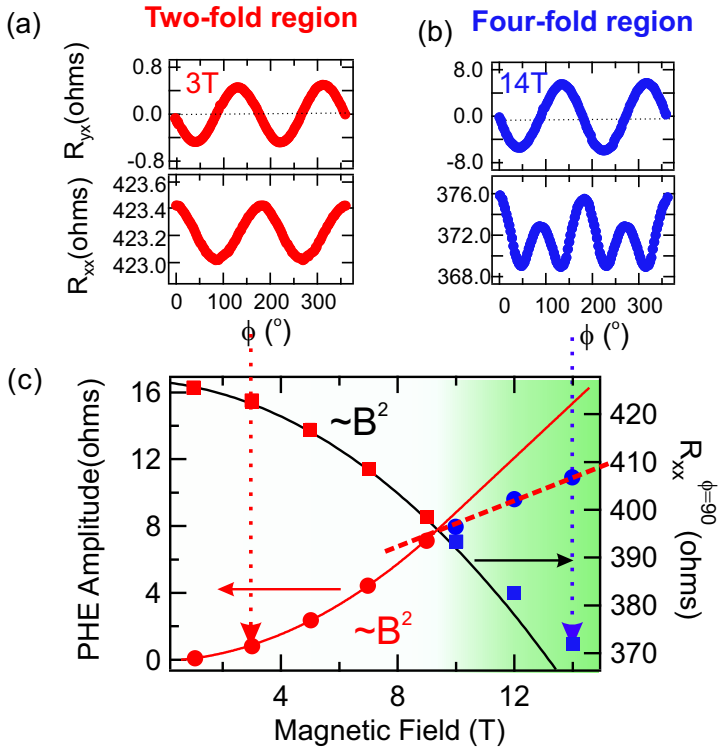

Figure 5.4: (a) R_{yx} and R_{xx} data for 3 T and (b) for 14 T. (c) The red markers (white background area) show the low magnetic field region where AMR has two fold symmetry and blue markers (green background) show high field region where AMR has four fold symmetry. Circles represent the PHE amplitude as a function of magnetic field and squares represent $R_{xx}^{\phi=90}$ i.e. absolute value of magnetoresistance R_{xx} for ϕ=90^o as a function of magnetic field.

For these measurements, with magnetic field (**B**) applied in the sample plane, simultaneous measurements of longitudinal magnetoresistance (R_{xx}) and transverse resistance (R_{yx}) were made while varying the in-plane angle between I and **B**. For the first set of experiments, R_{xx} and R_{yx} were measured at 1.8 K by varying the magnitude of applied magnetic field. On scanning the angle between **B** and I, R_{xx} and R_{yx} were found to show oscillatory behavior. Upto 8 T, we obtained 2 fold periodic oscillations in R_{xx}, it slowly changed to 4 fold oscillations above 8 T. **Figure 5.3(c)** shows the R_{xx} behavior at 3 T and 14 T. The behavior of normalized R_{xx} on varying the applied magnetic field is shown in the contour plot presented in **Fig. 5.3(e)**, where $R_{xx}^{norm} = (R - R_{symm})/(R_o - R_{symm})$. $R_{symm} = R_{min} + (R_{max} - R_{min})/2$ and R_{min} is minimum value of R_{xx}, R_{max} is maximum value of R_{xx} and R_o is the value of R_{xx} at 0^o. The low field behavior of R_{xx} is very similar to that observed in topological insulator systems such as $Bi_{2-x}Sb_xTe_3$ thin films.[6]

We observed oscillations in the planar Hall resistance value as a function of in-plane angle between **B** and I, with minima at 45^o and maxima at 135^o repeated at 180^o interval. Field dependent measurements were also performed at 1.8 K. **Figure 5.3(f)** shows the contour plot of field dependent R_{yx} as a function of angle between **B** and I at 1.8 K. It was seen that, on decreasing the magnetic field, the amplitude of oscillations decreases but the nature of oscillations remains same throughout. **Figure 5.3(d)** shows the planar Hall resistance for 14 T and 3 T field. It is clear that the two-fold periodicity is maintained even for high fields.

Two to four fold transitions in AMR have been reported in STO but these transitions are much complicated and irregular.[25, 26, 27, 28] Such transitions in STO were explained in terms of Liftshitz transitions arising from the topological change in Fermi surface in presence of intrinsic magnetization of STO. The mechanism of such a transition for our system is not currently understood.

In addition to this, in topological materials, PHE originates from the Adler-Bell-Jackiw (ABJ) chiral anomaly and nontrivial Berry curvature and is regarded as an evidence of the Dirac/Weyl cones in the band structure.[6, 29, 30, 31, 32, 33, 34] In contrast, metals and semiconductors with trivial band structure, are not expected to show PHE. PHE and AMR in topological systems can be mathematically represented as,[31]

$$R^{PHE} = \Delta R^{chiral} sin(\Phi) cos(\Phi) \tag{5.2}$$

$$R_{xx} = R_{xx}^{\phi=90^o} + \Delta R^{chiral} cos^2(\Phi) \tag{5.3}$$

where, ΔR^{chiral} is the chiral contribution to the PHE resistance (R_{yx}) and $R_{xx}^{\phi=90^o}$ is the absolute value of longitudinal magnetoresistance (R_{xx}) for ϕ=90^o. It was theoretically shown that the amplitude of PHE and AMR of such topological materials should follow B^2 dependence.[31]

The angular dependence of PHE and AMR of our system was found to be very similar to that observed for topological systems as shown in **Fig. 5.4(a)** and **(b)**. To illustrate this, we plotted the amplitude of PHE (left axis) and AMR (right axis) as a function of applied magnetic field in **Fig. 5.4(c)**. We found that the amplitude of both PHE as well as AMR exactly followed a B^2 dependence upto 9 T magnetic field. For larger fields, both deviated from B^2 dependence. It is worth noting that above this field, AMR no more follows $\cos^2(\phi)$ dependence (**Fig. 5.4(b)**). At the same time, although the two fold symmetry of PHE was retained above 9 T, the amplitude of PHE no more remained B^2 dependent.

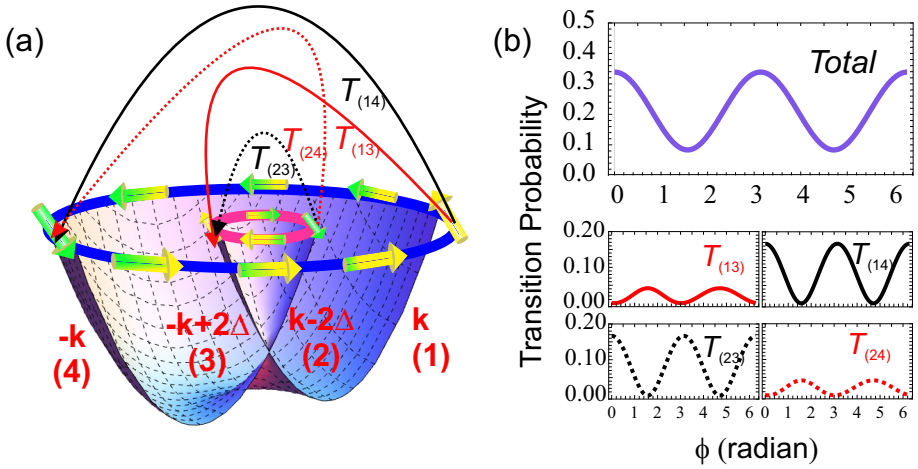

Figure 5.5: (a) Rashba energy-split bands showing spin-texture at a particular energy and the allowed electronic transitions. (b) Total probability and individual probabilities for different allowed electronic transitions between the bands.

5.3 Theoretical modelling

The observed two fold oscillations in the AMR and PHE as well as low field B^2 dependence of AMR and PHE amplitude on application of an in-plane magnetic field could be intuitively understood on the basis of electronic transitions which take place between the Rashba-split energy bands. In LVO-KTO system, due to broken

inversion symmetry at the interface and subsequently developed electric field, the relativistic electrons in $5d$ orbitals of Ta experience a pseudo magnetic field in the conduction plane and hence may lead to Rashba spin-splitting. The occurrence of a significant spin-orbit interaction has already been reported in the literature, from ARPES measurements in a single crystal of KTO.[23]. The presence of a Rashba spin-splitting, that relies on the additional presence of an electric field, was also seen in this material, for a Fermi wave vector ($\sim$0.2 A^{-1} to 0.4 A^{-1}) at a carrier density of $\sim$2x10^{14} cm^{-2}. On the other hand, our system is not just KTO but its interface with LVO (a polar material). Hence, like KTO, the interface, for a (measured) carrier density of 1.02x10^{14} cm^{-2} at a (calculated) Fermi vector of 0.3 A^{-1}, is not only endowed with a non-zero spin-orbit coupling, but is also expected to exhibit a prominent Rashba effect in view of a substantial, polar-polar interface-generated electric field. Our analysis presented below, is based on this premise.

In our system, the degenerate energy parabola of electrons is Rashba split into two parabolas as shown in **Fig. 5.5(a)**. Application of an external magnetic field in the conduction plane further adds a Zeeman splitting term. The external parabola is called the majority band and the internal parabola is called the minority band. Depending on the propagation vector **k**, spin of the electron, Rashba strength parameter α and the direction and magnitude of the external applied magnetic field, the electrons can make transitions between majority-to-majority (or minority-to-minority) i.e. intra-band transitions and majority-to-minority (or minority-to-majority) i.e. inter-band transitions. Each allowed transition results in back-scattering of the conduction electrons and hence, contributes to increase in resistance. The energy eigen values for the spin bands can be calculated by solving the Hamiltonian, which in the absence of magnetic field, can be written as[8]:

$$H = \epsilon(k) - \alpha(\sigma_x k_y - \sigma_y k_x) \tag{5.4}$$

where, ϵ(k) is free electron energy, $\sigma_{(x,y)}$ are the Pauli spin matrices, and k_x and k_y are the wave vectors in **x** and **y** direction. The electronic transition probability between the bands can be calculated using the eigen vectors for each band and finding the transition matrices. The eigen vectors used for the majority and minority bands are:

$$\frac{1}{\sqrt{2}} \begin{pmatrix} 1 \\ ie^{i\theta k} \end{pmatrix} \text{ and } \frac{1}{\sqrt{2}} \begin{pmatrix} 1 \\ -ie^{i\theta k} \end{pmatrix}$$

respectively, where, θ is the angle between **k**-vector and **x**-axis. The allowed

transitions between different bands (T_{13}, T_{14}, T_{23}, T_{24}) having finite probability are shown with arrows in **Fig. 5.5(a)**. Using the above eigen vectors, matrix elements for the transitions between the Rashba-energy split bands (1,2,3 and 4) were calculated to be:

$$\langle 1|\,\sigma_{\rm y}\,|2\rangle = f_-^*(k) - f_-(k-2\Delta) \tag{5.5}$$

$$\langle 1|\,\sigma_{\rm y}\,|3\rangle = f_-^*(k) - f_+(k-2\Delta) \tag{5.6}$$

$$\langle 1|\,\sigma_{\rm y}\,|4\rangle = f_-^*(k) + f_+(k) \tag{5.7}$$

$$\langle 2|\,\sigma_{\rm y}\,|3\rangle = -f_-^*(k-2\Delta) - f_+(k-2\Delta) \tag{5.8}$$

$$\langle 2|\,\sigma_{\rm y}\,|4\rangle = -f_-^*(k-2\Delta) + f_+(k) \tag{5.9}$$

$$\langle 3|\,\sigma_{\rm y}\,|4\rangle = -f_+^*(k-2\Delta) + f_+(k) \tag{5.10}$$

where,

$$f_{(+,-)}(k) = \frac{1}{2}[\frac{k + (-)rsin(\Phi) - (+)ircos(\Phi)}{\sqrt{r^2 + k^2 + (-)2rksin(\Phi)}}] \tag{5.11}$$

and f* is its complex conjugate, **k** is wave vector, Δ is the split in the Rashba-energy bands, ϕ is the angle between applied current (I) and magnetic field (**B**), $\sigma_{\rm y}$ is the Pauli-spin matrix and $\mathbf{r}=(\mu_B * \mathbf{B})/\alpha$. Knowing these matrices the transition probabilities were calculated as shown in **Fig. 5.5(b)**. It can be clearly seen that the prominent transitions followed a $\cos^2\phi$ dependence in agreement with our experimental data while the other transition prbabilities were low.

Apart from this, we were also able to capture the behavior of $R_{\rm xx}$ and $R_{\rm yx}$ using our theoretical model. For that, imagine that a **B**-field is applied in a direction which is also coincident with the above **x**-axis (which however is distinct from the **x**-axis in the laboratory frame i.e., the frame of the planar sample, along which the current is applied). The present **x-y**-frame then defines the principal coordinate system, in the sense of Taskin et al.[6] The corresponding Zeeman term contains the x-component of the Pauli spin which does not affect the term proportional to $k_{\rm y}$, in Eq. 5.4. However, the Zeeman coupling, being off-diagonal in the σ_y-representation, can cause a spin-flip thereby triggering a reversal in $k_{\rm x}$. Interestingly, these momentum-reversal transitions are akin to Drude scattering that is ever present, albeit small,

as a 'residual' resistivity [35]. Now, when the **B**-field is not too large (<8 T, in our experiments), the additional transition probabilities due to the Zeeman interaction can be calculated from the 'Golden Rule' of perturbation theory, thus yielding a quadratic dependence on **B**, which have to be supplanted to the residual Drude resistivity parallel to **x**-axis. The perpendicular component however retains only the residual part, for reasons mentioned earlier. The detailed analysis is discussed below:

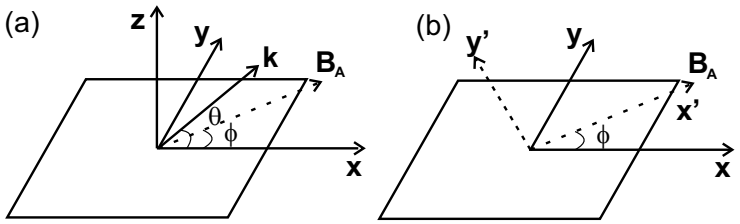

Figure 5.6: (a)Schematic for the direction of propagation of carriers and applied magnetic field. (b) Schematic presenting the laboratory frame of reference and the frame of reference of the applied magnetic field.

For our system, the total Hamiltonian can be written as:

$$H = H_{\mathrm{o}} + V \tag{5.12}$$

where considering **Fig. 5.6(a)**,

$$H_o = \epsilon(k) - \alpha(\sigma_{\mathrm{x}} k_{\mathrm{y}} - \sigma_{\mathrm{y}} k_{\mathrm{x}}) \tag{5.13}$$

$$\alpha = \mu_{\mathrm{B}} \hbar E / mc^2$$

$$V = -\mu_{\mathrm{B}} |\mathbf{B_A}| (\sigma_{\mathrm{x}} cos\phi - \sigma_{\mathrm{y}} sin\phi) \tag{5.14}$$

H_{o} is the unperturbed Hamiltonian, V is the perturbation.

The eigenvalues of H_{o} are:

$$\lambda_{\mathrm{o}}^{\pm} = \epsilon(k) \mp \alpha k = \hbar^2 k^2 / 2m \mp \alpha k \tag{5.15}$$

$$k = \sqrt{k_{\mathrm{x}}^2 + k_{\mathrm{y}}^2}$$

The corresponding eigenfunctions known as minority Rashba-band and majority Rashba-band are respectively given as:[8]

$$|k^+\rangle = \frac{1}{\sqrt{2}} \begin{pmatrix} 1 \\ -ie^{i\theta_k} \end{pmatrix} and\, |k^-\rangle = \frac{1}{\sqrt{2}} \begin{pmatrix} 1 \\ ie^{i\theta_k} \end{pmatrix} \tag{5.16}$$

Here,

$$cos\theta_k = \frac{k_{\mathrm{x}}}{k} \; and \; sin\theta_k = \frac{k_{\mathrm{y}}}{k} \tag{5.17}$$

Now referring to Taskin et al. supplementary notes[6], when a resistivity anisotropy is induced by an in-plane magnetic field $\mathbf{B_A}$ along **x'**-axis (**Fig. 5.6(b)**), the resistivity tensor may be written in a diagonalized form:

$$\begin{pmatrix} E_{\mathrm{x'}} \\ E_{\mathrm{y'}} \end{pmatrix} = \begin{pmatrix} R_{\parallel} & 0 \\ 0 & R_{\perp} \end{pmatrix} \begin{pmatrix} j_{\mathrm{x'}} \\ j_{\mathrm{y'}} \end{pmatrix} \tag{5.18}$$

Here, $E_{\mathrm{x'}}$ and $j_{\mathrm{x'}}$ are along $\mathbf{B_A}$ while $E_{\mathrm{y'}}$ and $j_{\mathrm{y'}}$ are perpendicular. Here, unlike Taskin et al., we provide explicit expressions for $R_{\parallel}$ and $R_{\perp}$ with reference to the Hamiltonian in Eqs. 5.12-5.14.

Computation of $\boldsymbol{R_{\perp}}$ This part is the simplest because in this geometry, the electric field $\mathbf{E}$ is applied along **y'**-axis ($E_{\mathrm{y'}}$) and the current j is also measured in this direction ($j_{\mathrm{y'}}$). Hence, the magnetic field, being normal to **y'**-axis, has no influence on $R_{\perp}$, thereby making the Rashba physics irrelevant. Then we take $R_{\perp}$ to be the simple Drude contribution R_o, which we do not calculate. So,

$$R_{\perp} = R_{\mathrm{o}} \tag{5.19}$$

Computation of $\boldsymbol{R_{\parallel}}$ Now, both the electric field $E_{\mathrm{x'}}$ and the current $j_{\mathrm{x'}}$ are along the direction in which the in-plane $\mathbf{B_A}$ field is applied. Therefore, in addition to the residual Drude resistivity R_{o}, the strong presence of the spin-orbit interaction via the Rashba effect comes into play.

Because $\mathbf{B_A}$ couples to $\sigma_{\mathrm{x'}}$ via the Zeeman interaction (Eq. 5.14), it causes transitions between the majority and minority Rashba bands which are the eigenstates of the unperturbed Hamiltonian H_{o} (Eq. 5.16). These transitions are like 'spin-flip' scattering processes which, in turn, cause momentum reversal (from **k** to **-k**) thereby causing resistance. In first order perturbation theory,

$$R_{\parallel} = R_{\mathrm{o}} + \gamma \mu_{\mathrm{B}}^2 \, |\mathbf{B_A}|^2 \, \overline{|\, \langle \underline{k}'^{-} |\, \sigma_{\mathrm{x}} \, |\underline{k}'^{+}\rangle \,|^2} \tag{5.20}$$

γ being a constant, where from Eq. 5.16,

$$|\underline{k}'^{+}\rangle = \frac{1}{\sqrt{2}} \begin{pmatrix} 1 \\ -ie^{i\theta_{k'}} \end{pmatrix} and \, |\underline{k}'^{-}\rangle = \frac{1}{\sqrt{2}} \begin{pmatrix} 1 \\ ie^{i\theta'_k} \end{pmatrix} \tag{5.21}$$

In Eq. 5.20, the Drude contribution R_{o} is added. The bar denotes an average over all $\underline{\mathrm{k}}$'-directions. Now,

$$\langle \underline{k}'^{-} |\, \sigma_{\mathrm{x}} \,| \underline{k}'^{+} \rangle = \frac{1}{2} \begin{pmatrix} 1 & -ie^{-i\theta_{k'}} \end{pmatrix} \begin{pmatrix} 0 & 1 \\ 1 & 0 \end{pmatrix} \begin{pmatrix} 1 \\ -ie^{i\theta_{k'}} \end{pmatrix}$$

$$= \frac{1}{2} \begin{pmatrix} 1 & -ie^{-i\theta_{k'}} \end{pmatrix} \begin{pmatrix} -ie^{i\theta_{k'}} \\ 1 \end{pmatrix} = -icos\theta'_k$$

Therefore,

$$\overline{|\, \langle \underline{k}'^{-} |\, \sigma_{\mathrm{x}} \,| \underline{k}'^{+} \rangle \,|^2} = \overline{cos^2\theta_{k'}} = \frac{1}{2} \tag{5.22}$$

Substituting,

$$R_{\parallel} = R_{\mathrm{o}} + \frac{\gamma}{2} \mu_{\mathrm{B}}^2 \; B_{\mathrm{A}}^2 \tag{5.23}$$

Following Taskin et al., the transformation from the principal axes to the film (i.e. laboratory axes) is effected by

$$\begin{pmatrix} E_{\mathrm{x}} \\ E_{\mathrm{y}} \end{pmatrix} = \begin{pmatrix} cos\phi & -sin\phi \\ sin\phi & cos\phi \end{pmatrix} \begin{pmatrix} R_{\parallel} & 0 \\ 0 & R_{\perp} \end{pmatrix} \begin{pmatrix} cos\phi & sin\phi \\ -sin\phi & cos\phi \end{pmatrix} \begin{pmatrix} j_{\mathrm{x}} \\ j_{\mathrm{y}} \end{pmatrix} \tag{5.24}$$

By setting j_{y}=0, in confirmation with our experimental results, we get,

$$R_{\mathrm{xx}} = \frac{E_{\mathrm{x}}}{j_{\mathrm{x}}} = R_{\perp} + (R_{\parallel} - R_{\perp}) cos^2\phi \tag{5.25}$$

$$R_{\mathrm{yx}} = \frac{E_{\mathrm{y}}}{j_{\mathrm{x}}} = (R_{\parallel} - R_{\perp}) cos\phi sin\phi \tag{5.26}$$

From Eq. 5.23 and 5.19,

$$R_{\mathrm{xx}} = R_{\mathrm{o}} + \frac{\gamma}{2} \mu_{\mathrm{B}}^2 \; B_{\mathrm{A}}^2 \; cos^2\phi \tag{5.27}$$

$$R_{\mathrm{yx}} = \frac{\gamma}{2} \mu_{\mathrm{B}}^2 \; B_{\mathrm{A}}^2 \; cos\phi sin\phi \tag{5.28}$$

In Eq. 5.27, R_o is expected to be small.

With the parallel and perpendicular ('diagonal') components in hand we can transform back to the laboratory frame a la Taskin et al.[6] Since the residual Drude resistivity cancels out from the difference between the parallel and perpendicular

components, the dominant contribution to the resistivity arises from the Rashba effect. Further, following Taskin et al. [6], $R_{xx} \sim(\cos^2 \phi)$, while $R_{yx} \sim (\cos\phi \sin\phi)$, both being proportional to B^2, in conformity with our data shown **Fig. 5.3**. Here, ϕ is the angle between the applied magnetic field and the direction along which the current is measured. As we mentioned earlier, beyond 8 T, there is a substantial departure in the $(\cos^2 \phi)$-behavior of R_{xx}, as well as its B^2 dependence, a theoretical understanding of which requires going beyond the Golden Rule of perturbation theory and perhaps also the simple Rashba effect, implemented in this paper.

In the present system, we speculate that it might be due to the relativistic character with strong spin-orbit coupling of the carriers in the system. Our observations suggest a detailed theoretical model of such systems is essential and it would have to contain ingredients of low dimensionality, relativistic electrons, localized magnetic moments and strong spin-orbit coupling. Further evolution of the Fermi surface with electrostatic gating and in-plane magnetic field can be explored which we plan to do in a follow-up study to build up a complete understanding of the mechanism.[36]

5.4 Conclusion

In conclusion, we realized a high mobility two dimensional electron gas at a new interface of two polar-polar perovskite oxides. We observed a high spin-orbit coupling in the system. The magneto-transport measurements showed signature of in-plane anisotropic transverse and longitudinal magnetoresistance as a consequence of strong spin-orbit coupling and Rashba spin splitting. The observed nature of the AMR and PHE at low magnetic field showed very similar behavior as observed in topological materials having Weyl-fermions due to ABJ chiral anomaly. The observed features of PHE and AMR at low magnetic field could be understood from our phenomenological theory with Rashba-spin splitting. The high field four fold AMR warrants an elaborate theoretical analysis. Such a model system may open up an avenue for in depth understanding of the physical properties of low dimensional relativistic electrons in oxide materials with strong spin-orbit coupling. Such detailed understanding might play an important role in the design of new materials for spintronic applications.

Bibliography

[1] Y. Tokura, M. Kawasaki and N. Nagaosa, *Nat. Phys.*, **13**, 1056 (2017).

[2] S. Gariglio, A.D. Caviglia, J. M. Triscone and M. Gabay, *Rep. Prog. Phys.*, **82**, 012501 (2019).

[3] M. Uchida and M. Kawasaki, *J. Phys. D: Appl. Phys.*, **51**, 143001,(2018).

[4] V.D. Ky, *Phys. Stat. Sol.*, **26**, 565 (1968).

[5] S.T.B. Goennenwein, R.S. Keizer, S.W. Schink, I.V. Dijk, T.M. Klapwijk, G.X. Miao, G. Xiao, and A. Gupta,*Appl. Phys. Lett.*, **90**, 142509 (2007).

[6] A.A. Taskin, H.F. Legg, F. Yang, S. Sasaki, Y. Kanai, K. Matsumoto, A. Rosch, and Y. Ando, *Nat. Commun.*, **8**, 1340 (2007).

[7] D. Rakhmilevich, F. Wang, W. Zhao, M.H. Chan, J.S. Moodera, C. Liu, and C.Z. Chang, *Phys. Rev. B*, **98**, 094404 (2018).

[8] M. Trushin, K. Vyborny, P. Moraczewski, A.A. Kovalev, J. Schliemann, and T. Jungwirth, *Phy. Rev. B*, **80**, 134405 (2009).

[9] I.V. Kozlov, and Y.A. Kolesnichenko *Phys. Rev.B*, **99**, 085129 (2019).

[10] G. Bergmann, *Phys. Rep.*, **107**, 1 (1984).

[11] S. Hikami, A. I. Larkin, and Y. Nagaoka, *Prog. Theor. Phys.*, **63**, 707 (1980).

[12] H. Nakamura and T. Kimura *Phys. Rev. B*, **80**, 121308 (2009).

[13] W. Knap et al., *Phys. Rev. B*, **53**, 3912 (1996).

[14] T. Koga, J. Nitta, T. Akazaki, and H. Takayanagi, *Phys. Rev. Lett.*, **89**, 046801 (2002).

[15] J. B. Miller, D. M. Zumbuhl, C. M. Marcus, Y. B. Lyanda-Geller, D. Goldhaber-Gordon, K. Campman, and A. C. Gossard, *Phys. Rev. Lett.*, **90**, 076807 (2003).

[16] X. Wu, X. Li, Z. Song, C. Berger, and W. A. de Heer, *Phys. Rev. Lett.*, **98**, 136801 (2007).

[17] S.V. Iordanskii, Y.B. Lyanda-Geller, and G.E. Pikus, *JETP Lett.*, **60**, 206 (1994).

[18] J. Lee, J. Park, J.H. Lee, J,S. Kim, and H.J. Lee, *Phys. Rev. B*, **86**, 245321 (2012).

[19] A.D. Caviglia, M. Gabay, S. Gariglio, N. Reyren, C. Cancellieri, and J.M. Triscone, *Phys. Rev. Lett.*, **104**, 126803 (2010).

[20] G. Herranz, G. Singh, N. Bergeal, A. Jouan, J. Lesueur, J. Gazquez, M. Varela, M. Scigaj, N. Dix, F. Sanchez, and J. Fontcuberta, *Nat. Commun.*, **6**, 6028 (2015).

[21] K. Gopinadhan, A. Annadi, Y. Kim, A. Srivastava,cB. Kumar, J. Chen, J.M.D. Coey, Ariando, and T. Venkatesan, *Adv. Electron. Mater.*, **1**, 1500114 (2015).

[22] M.J. Veit, R. Arras, B.J. Ramshaw, R. Pentcheva, and Y. Suzuki, *Nat. Commun.*, **9**, 1458 (2018).

[23] P.D.C. King, R.H. He, T. Eknapakul, S.K. Mo, Y. Kaneko, S. Harashima, Y. Hikita, M.S. Bahramy, C. Bell, Z. Hussain, Y. Tokura, Z.X. Shen, H.Y. Hwang, F. Baumberger, and W. Meevasana, *Phys. Rev. Lett.*, **108**, 117602 (2012).

[24] A.F.S. Syro, F. Fortuna, C. Bareille, T.C. Rodel, G. Landolt, N.C. Plumb, J.H. Dil, and M. Radovic, *Nat. Mater.*, **13**, 1085 (2014).

[25] M.B. Shalom, C.W. Tai, Y. Lereah, M. Sachs, E. Levy, D. Rakhmilevitch, A. Palevski, and Y. Dagan, *Appl. Phys. B*, **80**, 40403 (2009).

[26] A. Annadi, Z. Huang, K. Gopinadhan, X.R. Wang, A. Srivastava, Z.Q. Liu, L.C. Zhang, H.H Ma, T.P. Sarkar, T. Venkatesan, and Ariando, *Phys. Rev. B*, **87**, 201102(R) (2013).

[27] H.J.H. Ma, J. Zhou, M. Yang, Y. Liu, S.W. Zeng, W.X. Zhou, L.C. Zhang, T. Venkatesan, Y.P. Feng, and Ariando, *Phys. Rev. B*, **95**, 155314 (2017).

[28] P.K. Rout, I. Agireen, E. Maniv, M. Goldstein, and Y. Dagan, *Phys. Rev. B*, **95**, 241107(R) (2017).

[29] R. Singha, S. Roy, A. Pariari, B. Satpati, and P. Mandal, *Phys. Rev. B*, **98**, 081103(R) (2018).

[30] A.A. Burkov, *Phys. Rev. B*, **96**, 041110(R) (2077).

[31] S. Nandy, G. Sharma, A. Taraphder, and S. Tewari, *Phys. Rev. Lett.*, **119**, 176804 (2017).

[32] N. Kumar, S.N. Guin, C. Felser, and C. Shekhar, *Phys. Rev. B*, **98**, 041103(R) (2018).

[33] S. Nandy, A. Taraphder, and S. Tewari, *Sci. Reports*, **8**, 14983 (2018).

[34] D. Ma, H. Jang, H. Liu, and X.C. Xie, *Phys. Rev. B*, **99**, 115121 (2019).

[35] N.W. Ashcroft, and N.D. Mermin, *Solid State Physics, Cengage Learning,*, ISBN 8131500527, 9788131500521 (2011).

[36] D. Bucheli, M. Grilli, F. Peronaci, G. Seibold, and S. Caprara, *Phys. Rev. B*, **89**, 195448 (2014).

Chapter 6

Defects, conductivity and photoconductivity in Ar^+ bombarded $KTaO_3$

6.1 Introduction

Light is an important stimuli which can tune the electronic configuration and hence the physical properties of a system.[1, 2] The illumination of STO-based systems with ultraviolet/visible light has been demonstrated to enhance the electrical conductivity by several orders of magnitude.[3, 4] It has also been observed that the oxygen vacancies present in these systems play a substantial role in their photoresponse.[5, 6, 7, 8, 9, 10] Hence, understanding the creation of oxygen vacancies and the dependence of the photodynamics of a system on it may give further insight to the electronic states as well as the device performance of oxide based system.

In this chapter, we discuss photoresponse of conducting surface of (001) KTO single crystal which is realized by Ar^+ bombardment through the creation of oxygen vacancies.[10, 11, 12, 13] The time evolution of photoresponse to a daylight illumination lamp can be described with a bi-exponential function for all the samples having different charge carrier densities. The amplitude of photoresponse strongly depends on the charge carrier density whereas the response time is independent of

it. The dynamics of a sample with charge carrier density 4x10^{14} cm^{-2} has been studied under 633, 532 and 405 nm laser light illumination. Under 405 nm laser light, the photoresponse can be described with a bi-exponential function whereas it follows a single exponential function when illuminated with monochromatic light at 532 and 633 nm. The defect states are calculated from the photoconductivity relaxation. The Fermi level position in Ar^+ bombarded samples is probed using KPFM measurement technique and is found to be always positioned inside the KTO band gap even under the laser light illumination. This founding may contradict the observation of electrical conductance in our samples down to 2 K. However, the hint to resolve this apparent contradiction is provided by AFM images visualizing the appearance of strip like structures, which are suggested to be interconnected oxygen vacancies formed along some preferential crystal orientation. To reconcile KPFM and electrical conductance measurement, we suggest that the KTO surface exhibits large patches of non-conducting regions intercalated with conducting paths.

6.2 Experimental Details

Single crystals of both sides polished KTO (MTI Corporation) with orientation (001) were bombarded with Ar^+ for different duration of time using the reactive ion etch mode in the SI500 system (Sentech) to realize the conducting surface. The flow rate of 100 SCCM of Ar, 80 mTorr pressure, -530 V bias voltage and rf power of 225 W were used during bombardment.[12] Three different Ar^+ irradiation times (20, 30 and 40 minutes) were used to prepare the samples with different charge carrier densities. The transport measurements were performed with the help of physical property measurement system (PPMS). To perform these measurements, first the gold electrodes were deposited on the sample surface and then ohmic contacts were made by using ultrasonic wire bonder. The Hall measurements were performed for all samples at room temperature in dark. The conductivity measurements were performed for all samples at room temperature in dark, under daylight and monochromatic light (wavelengths, 633, 532 and 405 nm) illumination. The KPFM measurements were performed using conducting tip (Model: SCM-PIT) to probe the position of Fermi level under different conditions: in dark, after Ar^+ bombardment and under light illumination. The morphology of the samples was checked with the help of AFM (Bruker Multimode 08) in tapping mode.

6.3 Results and Discussion

After bombarding the samples with Ar^+ ions, the electrical conductivity of the samples was checked. The transport measurements suggested that all samples were conducting down to 2 K as shown in **Fig. 6.1(b)**. An average sheet charge carrier density (defined as charge carrier density per unit area) of 3.3x10^{13}, 4.0x10^{14} and 1.7x10^{15} cm^{-2} was estimated from the Hall measurements at performed at room temperature in dark for 20, 30 and 40 minutes of bombardment respectively. Inset of **Fig. 6.1(b)** shows the Hall measurements performed at room temperature for the sample with charge carrier density 4x10^{14} cm^{-2}. The linear behavior of ρ_{yx} suggested the existence of only one type of charge carriers, i.e, electrons in our case.[12]

6.3.1 Photoresponse under daylight illumination

Then, the photoconductivity measurements were performed on all the samples. **Figure 6.1(a)** shows the schematic of measurement geometry. Prior to exposure to daylight lamp illumination, the samples were left in dark for long time until their resistivity value saturated. **Figure 6.1(c)** shows the percentage change in resistance with time under the daylight lamp illumination. The largest photoresponse (∼40%) was reached for a sample with the lowest charge carrier density. The percentage change in resistance was defined as

$$\Delta R(\%) = \frac{R - R_0}{R_0} * 100$$

where R_0 is the sample's saturated resistance value reached in dark.

Figure 6.1(c) suggests that the amplitude of the photoresponse increases with the decreasing charge carrier density. **Figure 6.1(d)** shows the change of resistance normalised to its value after 40 minutes of illumination and suggests the response dynamics remain independent of carrier density. Then, to explore more about the nature of the photoresponse, we tried fitting our data. The photoresponse dynamics of any sample could not be described with a single exponential function. As an example, we have illustrated this fact in **Fig. 6.1(e)** for a sample with the carrier density 4x10^{14} cm^{-2}. The red solid line represents the single exponential fit curve. The photodynamics however, could be described with a bi-exponential function (black solid line):

$$R = Ae^{(-t/\tau_1)} + Be^{(-t/\tau_2)} \tag{6.1}$$

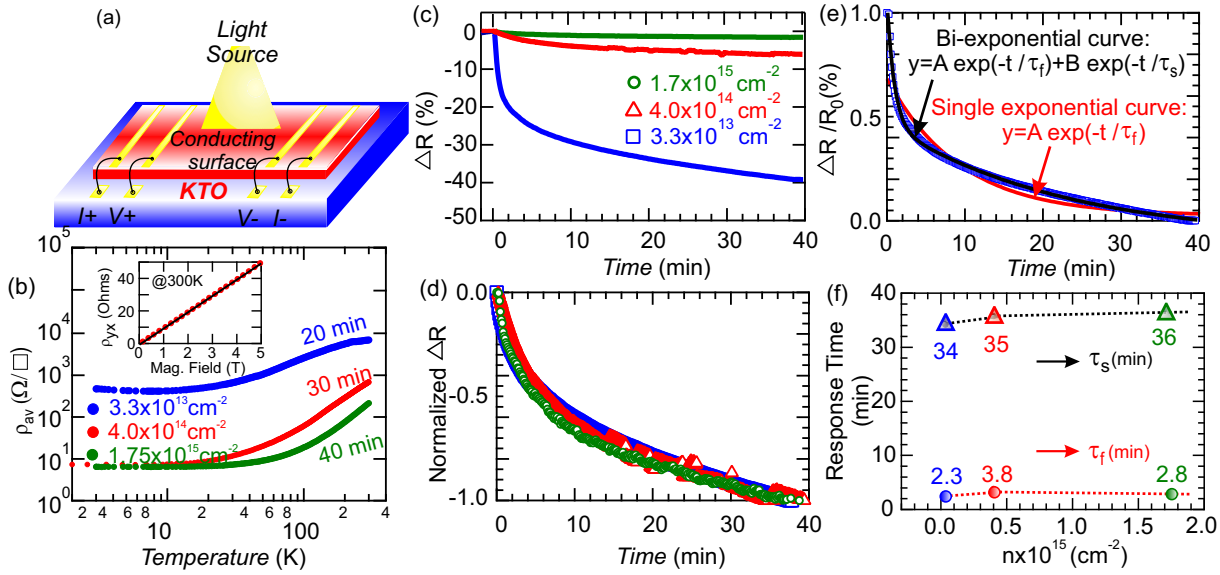

Figure 6.1: (a) Schematic of conductivity measurement geometry on Ar^+ bombarded KTO single crystals. (b) Sheet resistance as a function of temperature for all the samples bombarded with Ar^+ for different duration of time. Inset shows the Hall resistance as a function of magnetic field at room temperature for the sample with charge carrier density $4x10^{14}$ cm^{-2}. (c) Percentage change of resistance to daylight illumination. (d) Normalized change of resistance vs. time. The percentage change of resistance is normalized to its value after 40 minutes illumination. (e) Fitting with single and bi-exponential functions of normalized percentage change in resistance for the sample with charge carrier density $4x10^{14}$ cm^{-2}. The red and black lines are the fit curves for single and bi-exponential functions respectively. (f) Response times (fast and slow) as a function of charge carrier density.

where A and τ_1 are the relative weight and response time related to one component respectively. B and τ_2 are the relative weight and the response time of the other component respectively. Earlier work on photoresponse of STO had also demonstrated slow and fast excitation dynamics, one from defect centers within band gap to conduction band (CB) and the other from the valence band (VB) to CB.[14] From our experimental observations, we could also associate one component (τ_1) as the fast dynamics component (τ_f) with the excitation of electrons from the defect states formed in the band gap near the CB edge due to Ar^+ bombardment to the CB and the other component (τ_2) as slow component (τ_s) with the excitation of electrons

from the defect states as well as bulk VB to CB. Other phenomena such as formation of excitons etc. in the presence of photons with a band of wavelengths, might also be taking place which slows down the response process. **Figure 6.1(f)** displays the response (fast and slow) times as a function of charge carrier density suggesting that both fast and slow components of response were independent of carrier density of the samples. This essentially suggested that the dynamics of the photocarriers is identical in all the samples.

6.3.2 Photoresponse under laser light illumination

After studying the photoresonse of oxygen vacant KTO samples under daylight illumination, we performed a detailed study of the photoresponse of the sample with charge carrier density 4.0x10^{14} cm^{-2} under monochromatic laser light illumination of different wavelengths. This sample was chosen intentionally, since the sample with the lowest charge carrier density had strong aging effect (turned insulating after some time) and the sample with the highest charge carrier concentration had small amplitude of photoconductivity. In contrast, the sample with charge carrier density 4x10^{14} cm^{-2} was stable and has significant photoconductivity effect. To study the effect of monochromatic light on this sample, we used three different wavelengths (λ): 405, 532 and 633 nm which correspond to 3.02 eV (near the band gap of the KTO), 2.33 eV and 1.95 eV (lower than the band gap of the KTO), respectively.

Figure 6.2(a) shows the percentage change of the resistance of the sample under the illumination with laser light at 405, 532 and 633 nm wavelengths and at different light intensity, suggesting a stronger response for 405 nm compared to 532 and 633 nm. **Figure 6.2(b)** shows that the percentage change of the resistance (ΔR) increases with the laser power for illumination with 405 nm wavelength, whereas much weaker power dependence is observed for the illumination with the laser light at 532 and 633 nm. This behavior could be understood in the following way: the energy of the 532 and 633 nm laser lights are lower than the KTO band gap. Therefore these lasers can only excite the electrons from the defect states formed within the band gap to the CB edge. Since the electrons are only being excited from the defect states to the CB edge, the effect for 532 nm laser light is small. And it is even smaller for 633 nm as compared to 532 nm since the energy of 633 nm is smaller than 532 nm. It can only excite the electrons from the defect states near the CB to the CB edge. On the other hand, since the energy of the laser light of wavelength 405 nm can promote electrons from the defect states formed within the band gap as

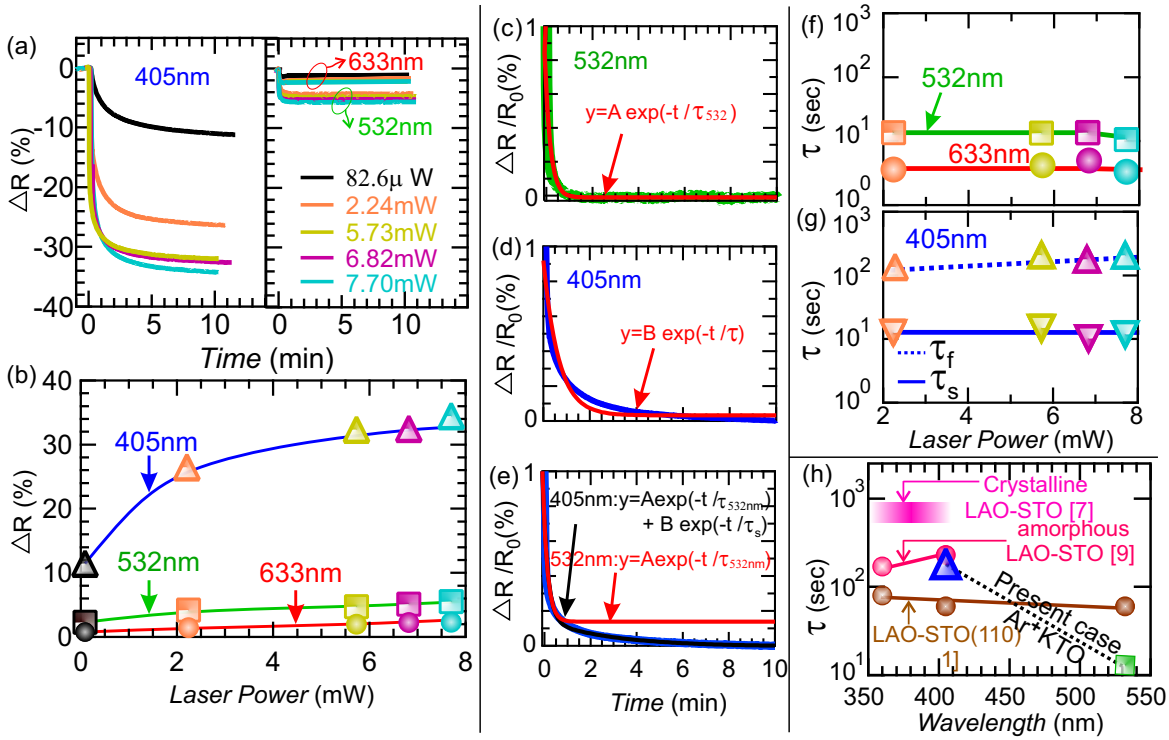

Figure 6.2: (a) Percentage change in resistance for the sample with charge carrier density 4x10^{14} cm^{-2} under illumination of different wavelength lasers and varying laser power. (b) Percentage change in resistance with varying laser power. (c) and (d) Single exponential fitting of normalised percentage change in resistance under illumination of 532 and 405 nm laser lights respectively. (e) Bi-exponential fitting of the response under illumination of 405 nm laser light. The black line is the bi-exponential fit curve and red line is the fit curve of the response for 532 nm laser light. (f) and (g) Response times as a function of laser power of wavelengths 633, 532 and 405 nm respectively. (h) Response time of Ar^+ bombarded surface conducting KTO as a function of the wavelength of illuminated laser light. This present sample is compared with that of reported conducting STO based interfaces.

well as from VB to the CB, the photoresponse amplitude keeps on increasing with the increase in the laser intensity due to large number of available electrons to be excited. The photoresponse gets saturated at a fixed laser intensity (6.82 mW) suggesting the balance between the excited and relaxed electrons. Further increasing the laser intensity does not increase the photoresopnse.

Similar to daylight illumination, the photoresponse under monochromatic light

illumination at wavelengths 633, 532 and 405 nm was fitted with single and bi-exponential functions. It was found that the response under 633 and 532 nm laser lights could be well fitted with single exponential function. The single exponential fitting for 532 nm (or 633 nm) laser light is shown in **Fig. 6.2(c)**, but the photoresponse under 405 nm laser light illumination could not be fit with a single exponential function as can be seen in **Fig. 6.2(d)**. However, it was perfectly fit using the bi-exponential function in Eq. 1.[9] **Figure 6.2(e)** shows the bi-exponential fitting of the response under 405 nm laser light. Fitting analysis (black line) suggested us that the response time under 405 nm laser wavelength had two components. One component was found to be same as that for 532 nm laser light (**Fig. 6.2(f)** and **(g)**) which we termed as the fast response (τ_f: τ_f=τ_{532nm}). Its contribution to the photoresponse at 405 nm is shown in red in **Fig. 6.2(e)**. This fast response comes from the promotion of electrons from defect states produced near to the CB edge to the CB. The other component termed as slow response (τ_s) comes from defect states all along the band gap as well as bulk VB to the CB. **Figure 6.2(f)** suggests that for 633 nm, the photoresponse is faster than that of 532 nm. **Figure 6.2(f)** and **(g)** summarize that the response times for illumination with λ=405, 532 and 633 nm are all independent of laser intensity. In **Fig. 6.2(h)**, we compared the response time of Ar^+ bombarded KTO sample with that of the reported STO based low dimensional conducting systems and it clearly indicates similar photoresponse time scales for both the systems.[1, 7, 9]

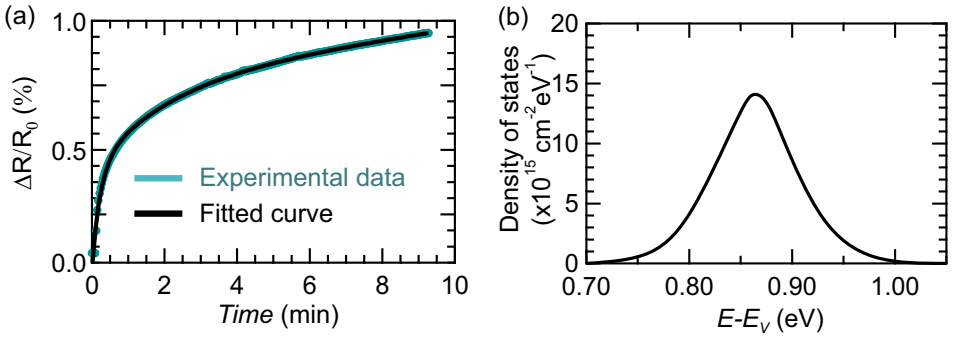

Figure 6.3: (a) Multiexponential curve fitting of the relaxation data when the light (405 nm) is turned off. (b) Defect density of states obtained from photoconductivity relaxation.

We then used our photoconductivity relaxation data to calculate the defect states distribution, as suggested by S. A. Studenikin et al.[15] To analyze the relaxation data, Laplace transform method was used[15, 16, 17] which gives rise to the

following expression for the effective density of states:

$$g(E) = \frac{N_i}{kT} \frac{\nu e^{-E/kT}/\tau_i}{(\nu e^{-E/kT} + 1/\tau_i)^2} \tag{6.2}$$

Where ν (=10^{12} s^{-1}) is the attempt to escape frequency[18], N_i is the defect density and τ_i is the characteristic time scale of the photoconductivity relaxation.

Following the same analysis, the relaxation data was first fitted (see **Fig. 6.3(a)**) to estimate the relaxation time and then the effective density of states (g(E)) was simulated (see **Fig. 6.3(b)**). This suggested us that the defect density of states was formed at about one-fourth of the band gap from the VB and had a peak like distribution with a maxima at 0.87 eV above the VB. The hole traps concentration was also calculated using following equation[17, 18]

$$N_{total} = \int g(E)dE$$

that came out to be 1.43x10^{15} cm^{-2}.

Then, the effect of laser light (532 and 405 nm) at a fixed power on the work function of this sample was studied with the help of KPFM at room temperature using conducting tip (Model: SCM-PIT-V2).[19] The KPFM measurements were performed at laser power of 7.7 mW since the maximum photoresponse was observed at this laser power. The work function of the sample was measured first in dark and then under illumination with the laser light of different wavelengths.

Figures 6.4(a-c) show the KPFM images of the bombarded sample with carrier density 4x10^{14} cm^{-2} obtained in dark and under illumination of laser light λ=405 and 532 nm respectively. The change in the contrast of KPFM images depicts the change in the work functions of bombarded and illuminated samples. To visualize the change of the work function for each wavelength more clearly, the corresponding laser lights were turned on in the middle of the KPFM scans. The sharp contrast of KPFM images in both panels in **Fig. 6.4(d)** signals the change in the work function upon excitation with laser light. **Figure 4(h)** shows the line scan of the work function along the arrows marked in **Fig. 6.4(a)** and **(d)** in corresponding color. The scan line presented in black dotted line in **Fig. 6.4(h)** is the work function of bare KTO.

From KPFM results, the work function of an unbombarded KTO was found to be 5.5 eV (black dotted line in **Fig. 6.4(h)**) and the work function of the bombarded KTO was calculated to be 5.25 eV.[19, 12] Hence, for Ar^+ bombarded

KTO, the Fermi level moved towards the CB edge by 0.25 eV from the middle of the band gap but it remained in the band gap.[12, 20, 21] This is confrontational to the fact that the sample was conducting down to 2 K (see **Fig. 6.5(a)**) with electrons being the charge carriers, suggesting that the Fermi level should reside in the CB (schematically depicted in **Fig. 6.5(b)**), rather than in the band gap. **Figure 6.5(c)** depicts the schematic of KPFM measurement on Ar^+ bombarded KTO. The KPFM measurements performed under laser lights of wavelengths 532 and 405 nm suggest the work functions to be 5.22 and 5.20 eV respectively. Thus the excitation with laser lights shifts the Fermi level towards CB by several tens meV. However, the Fermi level never lies inside the CB.

To explore about this non-trivial phenomenon, we performed controlled KPFM experiment on three different types of STO systems. We took pristine STO, Ar^+ bombarded conducting STO and Nb-doped STO. For pristine STO, KPFM measurement suggested that the Fermi level was lying at the center of the band gap (E_g=3.2 eV). For Ar^+ bombarded STO, KPFM results showed that the Fermi level moved up by 0.25 eV and hence, it was still in the band gap. This was similar to what we had observed for Ar^+ bombarded KTO (**Fig. 6.5(d)**). But for a uniformly chemical (Nb) doped conducting STO, KPFM measurements revealed that the Fermi level had moved upward by 1.7 eV which suggested that the Fermi level was lying in the CB. These observations suggested that the non-agreement between transport and KPFM measurement was special for Ar^+ bombarded conducting samples.

The discrepancy observed in the transport and KPFM measurement of Ar^+ bombarded KTO could be brought into the agreement if interconnecting narrow conducting patterns were formed on KTO sample, keeping a considerable amount of area insulating. A possible surface morphology is schematically shown in **Fig. 6.4(c)**. Creation of such patterned oxygen vacancies had already been observed on STO samples.[22] As illustrated in the picture, if macroscopic measurements like conductivity are performed then the presence of insulating islands in between conducting paths might be hindered suggesting the sample to be completely conducting. But at the same time, when local measurements such as KPFM are performed then the intermedia of both the regions come into picture and an average effect is observed. In particular, for the KPFM measurements of such sample, where the conducting parts try to bring the Fermi level into the CB, the insulating parts try to keep it in the mid gap. The average observed result is that the Fermi level still resides in the band gap but moved up towards the CB.

We also performed the AFM of the unbombarded and bombarded samples to

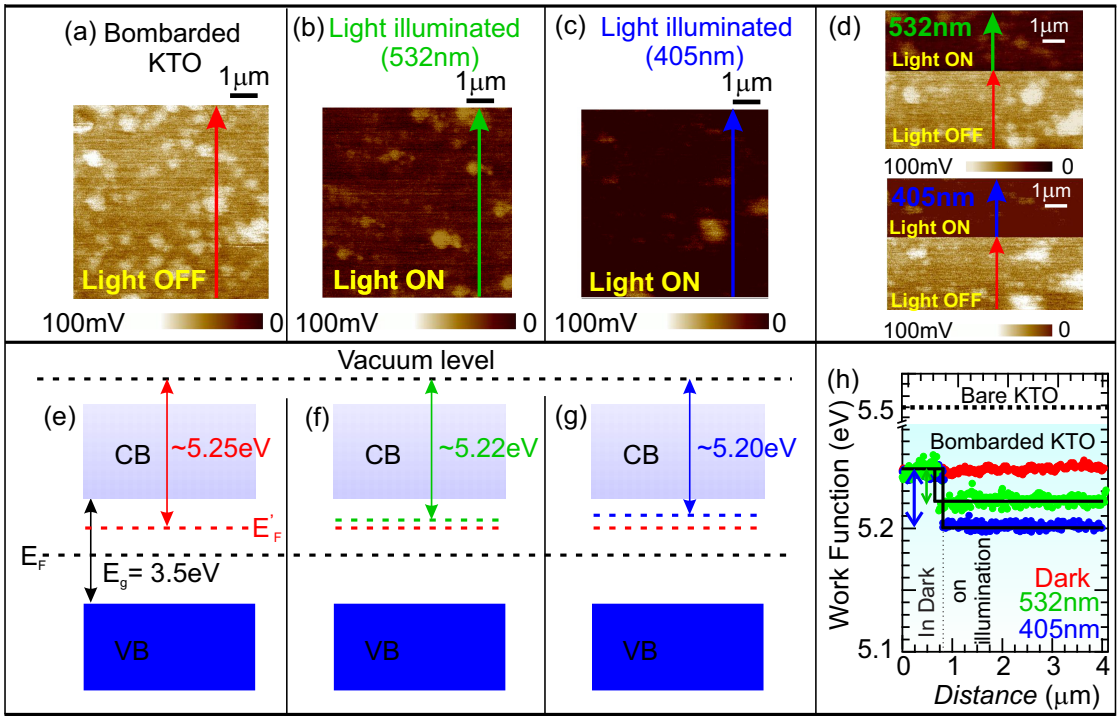

Figure 6.4: (a-c) KPFM images of bombarded, illuminated with 532 and 405 nm KTO samples with charge carrier density 4x10^{14} cm^{-2} respectively. (d) KPFM images: Top and bottom, where light (532 and 405 nm) is shinned in the middle of scan in dark. (e-g) The schematic band diagram of bombarded (in dark), illuminated with 532 and 405 nm wavelengths as observed from KPFM respectively. (h) Work functions of KTO sample for different cases (a-c) along the arrow shown in the KPFM images. The black dotted line shows the work function of bare KTO.

look carefully at the surface topography. We found strip like patterns on the bombarded surface along (100) and (010) crystallographic directions, as can be seen in **Fig. 6.5(f)**. The strips form a zig-zag pattern on the bombarded KTO. While, the surface of unbombarded KTO is smooth and has no pattern (**Fig. 6.5(e)**). These results suggested that conducting channels had been formed along some preferential directions ((100) and (010)) due to defect formation upon Ar^+ bombardment. These channels were interconnected but had non-conduction areas in between. When bulk property, such as transport is measured, it suggests that the sample is conducting. But a local measurement such as KPFM, that can also look into the non-conducting regions give the information about the percolating conducting channels. On annealing the bombarded KTO in air, the patterns formed vanish and the surface becomes

smooth similar to the bare KTO, as can be seen in **Fig. 6.5(g)**. It had also been reported in case of Ar^+ bombarded STO that oxygen vacancies are formed along some preferential direction.[22] The KPFM measurements under laser lights suggests that upon shinning the light, the charge carriers are pumped to the already conducting channels from the defect states created beneath them and contribute in the photoconductivity.

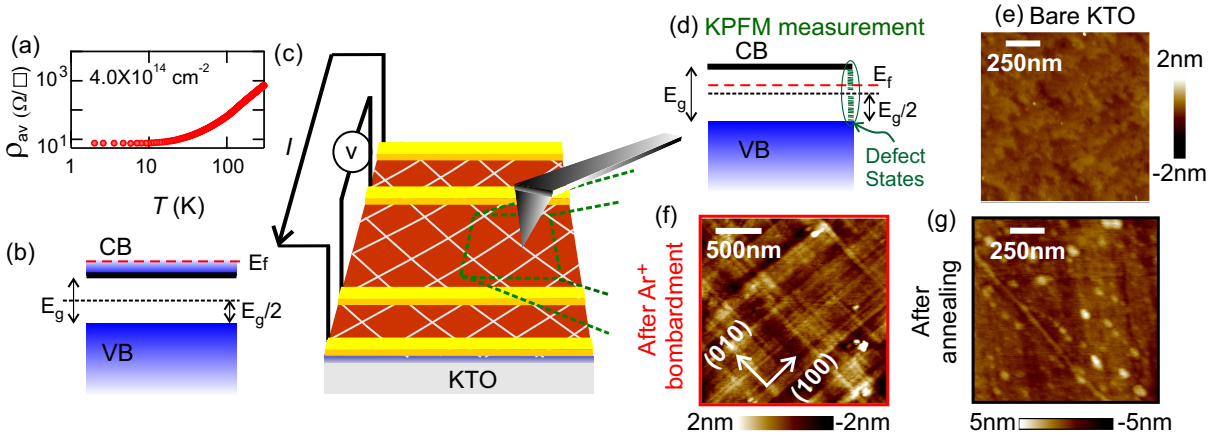

Figure 6.5: (a) Temperature dependent sheet resistance for the sample with charge carrier density 4x10^{14} cm^{-2}. (b) According to conductivity measurement schematic band diagram shows Fermi energy lying in conduction band. (c) Schematic of KPFM measurements on Ar^+ bombarded KTO single crystal. (d) Schematic band diagram drawn with KPFM results. Topographic AFM image of (e) Bare KTO (f) After Ar^+ bombardment (Scan angle-45^o) and (g) After annealing bombarded KTO in air.

6.4 Conclusion

In conclusion, we found that conductivity created on the surface of Ar^+ bombarded KTO through oxygen vacancies is not uniform. Defects are created along some preferential crystal directions and are connected to each other producing conducting channels on the surface. Photoconductivity measurements under daylight as well as laser light with wavelengths 633, 532 and 405 nm suggest that the photoresponse consists of two processes having two time scales: one is promotion of electrons from defect states created along the preferential directions on the surface of bombarded KTO and another is that from the VB as well as defect states to the CB. The defect

states calculated from the slow relaxation data show a peak like distribution with maxima at 0.87 eV above the VB. Predominant photoconductivity occurs mainly in the already conducting channels. Our observations demand a detailed and advanced surface as well as structural study of this interesting polar material that may hosts low dimensional conducting electron with strong spin-orbit coupling.

Bibliography

[1] M. Kim, C. Bell, Y. Hikita, Y. Kozuka, B.G. Kim, and H.Y. Hwang, *Sol. St. Commun.*, SLAC-PUB-15219 (2012).

[2] K. Zhang, L. Yan, and H.U. Habermeier, *J. Phys. Condens. Lett.*, **25**, 035802 (2013).

[3] N. Osawa, R. Takahashi, and M. Lippmaa, *Appl. Phys. Lett.*, **110**, 263902 (2017).

[4] F. Rossella, P. Galinetto, G. Samoggia, V. Trepakov, and L. Jastrabik, *Sol. Stat. Commun.*, **141**, 95 (2007).

[5] A. Rastogi, A.K. Kushwaha, T. Shiyani, A. Gangawar, and R.C. Budhani, *Adv. Mater.*, **22**, 4448 (2010).

[6] A. Rastogi, J.J. Pulikkotil, S. Auluck, Z. Hossain, and R.C. Budhani, *Phys. Rev. B*, **86**, 075127 (2012).

[7] A. Rastogi, and R.C. Budhani, *Opt. Lett.*, **37**, 317 (2012).

[8] A. Rastogi, J.J. Pulikkotil, and R.C. Budhani, *Phys. Rev. B*, **89**, 125127 (2014).

[9] E.D. Gennaro, U. Coscia, G. Ambrosone, A. Khare, F.M. Granozio, and U.S.D. Uccio, *Scien. Rep.*, **5**, 8393 (2015).

[10] D. Kumar, Z. Hossain, and R.C. Budhani, *Scien. Rep.*, **91**, 205117 (2015).

[11] S. Harashima, C. Bell, M. Kim, T. Yajima, Y. Hikita and H.Y. Hwang *Phys. Rev. B*, **88**, 085102 (2013).

[12] N. Wadehra, R. Tomar, H. Halder, M. Sharma, I. Singh, N. Jena, B. Prakash, A.D. Sarkar, C. Bera, A. Venkatesan, and S. Chakraverty, *Phys. Rev. B*, **96**, 115423 (2017).

[13] M. Stevin, M. Reticcioli, F. Poelzleitner, J. Hulva, M. Schmid, L. A. Boatner, C. Franchini, and U. Diebold, *Scien.*, **359**, 572 (2018).

[14] T. Feng, *Phys. Rev. B*, **25**, 627 (1982).

[15] S.A. Studenikin, N. Golega, and M. Cocivera, *Jour. Appl. Phys.*, **84**, 5001 (1998).

[16] H. Naito, and M. Okuda, *Jour. Appl. Phys.*, **77**, 3541 (1995).

[17] S.A. Studenikin, N. Golega, and M. Cocivera, *Semiconduc. Scien. Techno.*, **13**, 1383 (1998).

[18] S.A. Studenikin, N. Golega, and M. Cocivera, *Jour. Appl. Phys.*, **83**, 2104 (1998).

[19] R. Tomar, N. Wadehra, V. Budhiraja, B. Prakash, and S. Chakraverty, *Appl. Surf. Science*, **427**, 861 (2018).

[20] G.S. Bhalla, C. Bell, J. Ravichandran, W. Siemons, Y. Hikita, S. Salahuddin, A.F. Hebard, H.Y. Hwang, and R. Ramesh, *Nat. Phys.*, **7**, 80 (2011).

[21] N. Shanthi, and D.D. Sarma, *Phys. Rev. B*, **57**, 2153 (1998).

[22] M.S.J. Marshall, A.E.B. Toledo, L.D. Marks, and M.R. Castell, *Springer Series in Surf. Science*, **58**, DOI 10.1007/978-3-319-14367-5_11 (2015).

Chapter 7

Electrostatic memory in $KTaO_3$

7.1 Introduction

As discussed in the previous chapters, transition metal oxides have gained a lot of interest in the past few years because of their prospective applications and implementation in the emerging field of spintronics.[1, 2, 3, 4] The discovery of 2DEG at the interface of perovskite oxides LAO-STO in 2004 and possibility of realization of Rashba type spin splitting in such oxide heterointerfaces drew great attention towards this class of materials for spintronics based devices.[5] Also, observation of novel phenomena like giant magnetoresistance, superconductivity and anomalous Hall effect etc. in these oxides made them the most suitable candidates for such applications.[6, 7, 8, 9, 10] In addition to all this, their credibility was further endorsed by the fact that their conductivity can be tuned over a wide range and these structures can be scaled even to nano dimensions.[11, 12]

In the present day scenario, the advancement in technology has further eased down the process and has enhanced the usability of oxides. Recently, researchers have used atomic force microscopy (AFM) to write nano-electrical domains on the oxide heterostructures.[13, 14] This has extended their applicability to nano-electrostatic storage devices. Charge writing on LAO-STO interface has been reported.[15, 16, 17, 18] Other heterointerface such as LVO-STO has also been tried for charge writing and has shown similar results as LAO-STO.[19] Some other oxide thin films have also been tried for electrical domain writing over the years.[20, 21, 22] Realizing electrostatic memory on the surface of oxides with strong spin-orbit cou-

pling like KTO may open up new possibilities in terms of additional degrees of freedom to control in the field of nano-electrical storage systems.

In this chapter, we have realized the writing and erasing of "electrostatic memory" on the surface of conducting KTO using a biased conducting AFM tip. The written signal (phase difference between written and unwritten region) on KTO is around 3 times more than previously studied systems among perovskite oxides. Kelvin probe force microscopy (KPFM) measurements suggest writing pattern either accumulates or depletes electrons at the written region from the surrounding electron sea or re-distributes oxygen vacancies in the system depending upon the sign (positive or negative) of applied voltage on the tip. Magnetic force microscopy detects the appearance of a magnetic field when charge writing was done in a dipolar configuration. This may open up opportunities in the field of nano-electric devices for magnetic sensor applications.

7.2 Experimental Details

For the current study of exploring charge writing on KTO, we took oxygen vacant KTO (001) single crystals prepared by bombarding them with Ar^+ ions as reported in previous chapter.[23] The samples were conducting due to the formation of oxygen vacancies at the surface of the single crystal. Two different samples S1 and S2 were used, one bombarded for 20 minutes and the other for 5 minutes. The room temperature two probe resistance and charge carrier density of the samples were 30 kΩ and 2 $M\Omega$ and 5x10^{14} cm^{-2} and 1x10^{13} cm^{-2} respectively.

7.2.1 Electrical domain writing

Conducting AFM tip (SCM-PIT-V2) having PtIr coating was then used to induce extremely small electrically active charge domains on the surface of KTO using Bruker Multimode-8 AFM. The structures were written by scanning the tip in contact mode over an area of 2μm x 2μm. DC bias was applied to the tip (V_{tip}) and the samples were grounded as shown in **Fig. 7.1(a)**. Then the written structures were read by scanning the tip over an area of 6μm x 6μm using electrostatic force microscopy (EFM) mode of AFM. In this mode, the written structures are read by applying zero, positive and negative bias to the tip. The charge present on the sample exerts coulombic force of attraction or repulsion on the biased tip depending

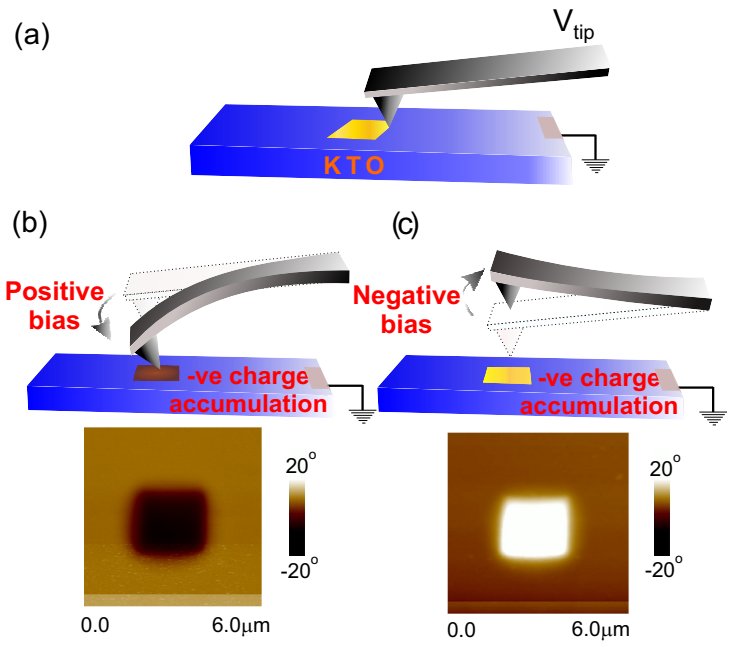

Figure 7.1: (a) Schematic of the writing geometry with biased AFM tip. (b)-(c) Schematic of the motion of tip when negative charge written on sample is read using positive or negative tip bias. (Below) AFM images of the phase change on reading with positive and negative tip bias applied.

on the nature of charge and the polarity of the tip reading voltage (V_r). This in turn changes the amplitude, phase and resonant frequency of the tip and the surface charge is detected by observing change in any one of these parameters.

Reading with zero bias always yields a darker contrast in the EFM phase image of the written region. This happens because the charge present on the sample induces charge of opposite polarity on the tip which results in bending of the tip due to coulombic forces of attraction between the tip and the written region. This observation reveals the presence of charge on the surface. In our case, we got similar darker contrast in the region written with -8V tip bias. The nature of the charge is detected by alternating the polarity of the reading voltage. In our case, reading with positive voltage, yielded a darker contrast in the phase image (**Fig. 7.1(b)**) indicating the presence of negative charges in the written region. Reading with negative voltage, repelled the tip and gave a brighter contrast in the phase image confirming the presence of negative charges in the written region (**Fig. 7.1(c)**). It was observed that it was not possible to write charge on bare KTO sample which is completely insulating but once the sample was made oxygen vacant and had mobile

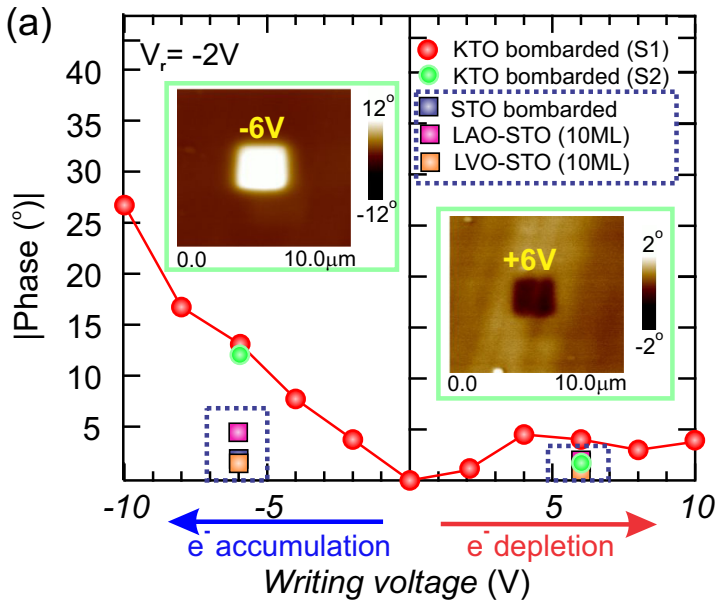

Figure 7.2: Phase change vs. tip writing voltage plot for oxygen vacant KTO samples and other STO based samples. (Inset) EFM phase images of sample S2 with charge written using -6V, +6V and read by -2V.

charge carriers, writing electrical domains was possible. **Figure 7.2** shows the phase vs. tip bias voltage plot for S1 where charge was written using V_{tip} in the range of ± 10V in steps of 2V and V_r is -2V. It was observed that there was an asymmetry in the phase change of the written region with respect to the polarity of the writing voltage which was in accordance with the observations in earlier reports.[16] We also tried to write on the other KTO sample (S2) which had less charge carrier density. But it was observed that the amount of the charge carriers had no effect on the writing ability. The phase change of the written region for writing voltage of -6V was almost same (13^o) in both the cases as shown in **Fig. 7.2**.

The phase change in the written region of KTO was compared with some other perovskite oxides based systems like Ar^+ bombarded oxygen vacant STO, interface conducting heterostructures of LVO-STO and LAO-STO. It was found that KTO has much larger phase change in comparison to any other perovskite oxide based systems for the same writing voltage of ± 6V as shown in **Fig. 7.2**.

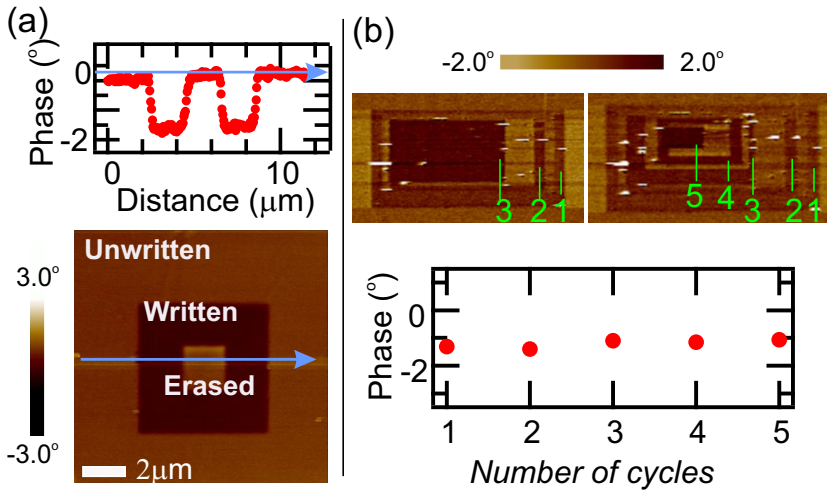

Figure 7.3: (a) (Bottom panel) Phase image of region written with +5 V and erased using -0.4 V. (Upper panel) Line profile of the phase image along the blue arrow. (b) (Upper panel) EFM phase image showing continuous writing and erasing in boxes of decreasing dimension: (Left image) after 3 cycles, (Right image) after 5 cycles. (Bottom panel) shows the phase response of the written region as a function of number of cycles of writing and erasing.

7.2.2 Erasability of written domains

The beauty of writing charge on KTO samples by AFM tip was that we could also erase the charge simply by applying opposite polarity voltage to the tip. It was found that the written structures on KTO could be erased and rewritten a number of times. Another observation was that due to the asymmetry in the response of the sample corresponding to the polarity of the writing voltage, very less magnitude of negative bias was required to erase the region written with positive voltage. For example, only -0.4V was required to erase the region written with +5V. By identifying the erasing voltage the written structures could be erased as required. **Figure 7.3(a)** shows the EFM phase image of a 6μm x 6μm square written using +5V and erased region of 2μm x 2μm using -0.4V. Top panel shows the line profile of the phase image along the blue arrow. It can be clearly seen that the erased region has the same phase as the unwritten region. **Figure 7.3(b)** top panel shows the shows the EFM image of consecutively written and erased boxes of decreasing dimension: (left image) boxes written with +5V and erased with -0.4V after 3 cycles, (right image) after 5 cycles. Lower panel shows the phase response of the written region as a

funtion of number of cycles of writing and erasing. The topmost smallest box in the EFM phase image is written and erased for 5 times and yet shows the same phase change as the box written for the first time. The ease of writing and erasing the written structure is a crucial thing for any memory devices.

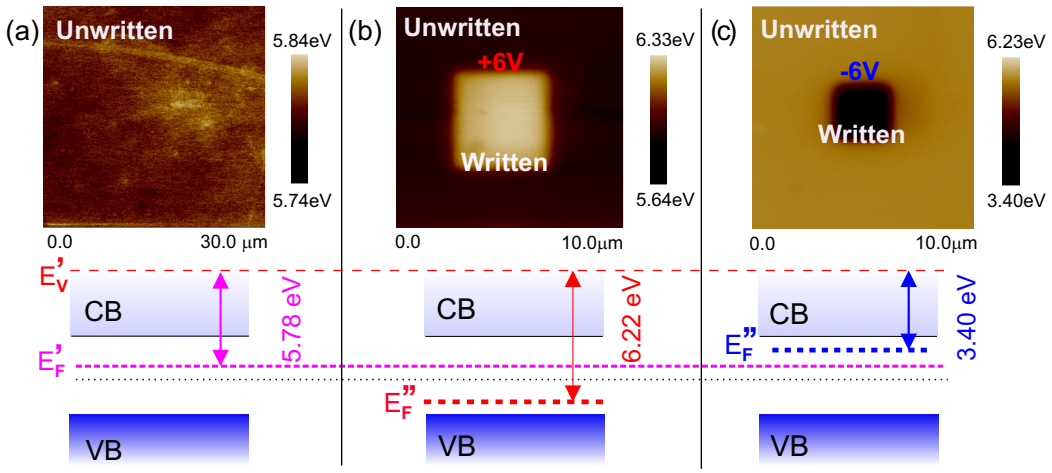

Figure 7.4: (a) Surface potential image of bombarded KTO S2 with no charge written region. (lower panel) its band diagram showing the movement of fermi level (E'_F) towards C.B. due to presence of oxygen vacancies. (b) and (c) Surface potential image of S2 with positive charges and negative charges written using +6V and -6V respectively. (lower panels) Band line-up showing movement of fermi level (E''_F) towards V.B. for +6V and towards C.B. for -6V written regions.

7.2.3 Surface potential changes in written regions

Also, to probe the surface potential changes in the written nano-electrical domain regions, we performed KPFM measurements. **Figure 7.4** shows the surface potential images of unwritten bombarded KTO (S2), KTO having regions written with +6V and -6V. The surface potential of the region written with +6V was found more and that of the region written with -6V was found to be less than the unwritten region indicating the presence of localized positive and negative charges in the two cases respectively. KPFM measurements were also used to estimate the work function changes in the written regions. The position of the fermi level in the sample was determined by firstly calibrating the work function of tip w.r.t standard sample of gold (work function 5.1 eV). Then, using contact potential difference (CPD) value

obtained from surface potential image, work function of KTO sample was calculated using equation $\Phi_{sample} = \Phi_{tip} + \text{CPD}$. Lower panels in the **Fig. 7.4 (a)-(c)** show the band line-up of the unwritten and written regions. The work function calculated for unwritten region was 5.78 eV which is accordance with the previous reports.[23] The fermi level of the region written with +6 V moved towards valence band (V.B.) and the calculated work function of 6.22 eV confirmed the presence of positive charges (or electron depletion) in the written region. The fermi level for -6 V region moved towards conduction band (C.B.) similar to the n-doped systems and had the work function of 3.40 eV confirming the presence of localized negative charges accumulation in the written region. There are two possible mechanisms which had been proposed for the charge writing phenomenon in STO based systems. Where one mechanism suggests the adsorption of H^+ and OH^- ions over the written regions, the other suggests the formation and re-distribution of oxygen vacancies depending on the polarity of the writing tip bias.[17, 24, 25] In our KTO case, the work function behavior appears very similar to that reported for STO charge writing case where an enhancement in local conductivity had been observed under the application of negative bias and the work function is found to decrease.[25, 26] In our case, we have also seen that charge writing is possible only for the reduced samples. These observations suggest that the possible origin of charge writing in KTO might be formation and re-distribution of oxygen vacancies.

7.2.4 Emergence of magnetic field from electrical domains

Then to check the possible emergence of magnetic field, the normal conducting tip was replaced with magnetic tip (model: MESP) for reading the phase change. The charges were written in two different configurations (monopole and dipole). In monopole configuration, a square was written with -8 V applied to the tip and then the written region was read as a function of time using a magnetic and non-magnetic tip separately with no tip bias applied. In dipole configuration, two rectangles of 1μm x 2μm each were written in contact with each other using -8 V and +8 V as shown in **Fig. 7.5** and were read as a function of time using magnetic and non-magnetic tip. Several continuous scans were run for about 140 minutes and phase change was monitored for each scan. It was observed that for dipole configuration, while reading with non-magnetic tip, the interaction for positive and negative charge region was attractive. The attractive forces were due to induction of opposite polarity charge on the tip. The phase change in this case simply decayed with time as

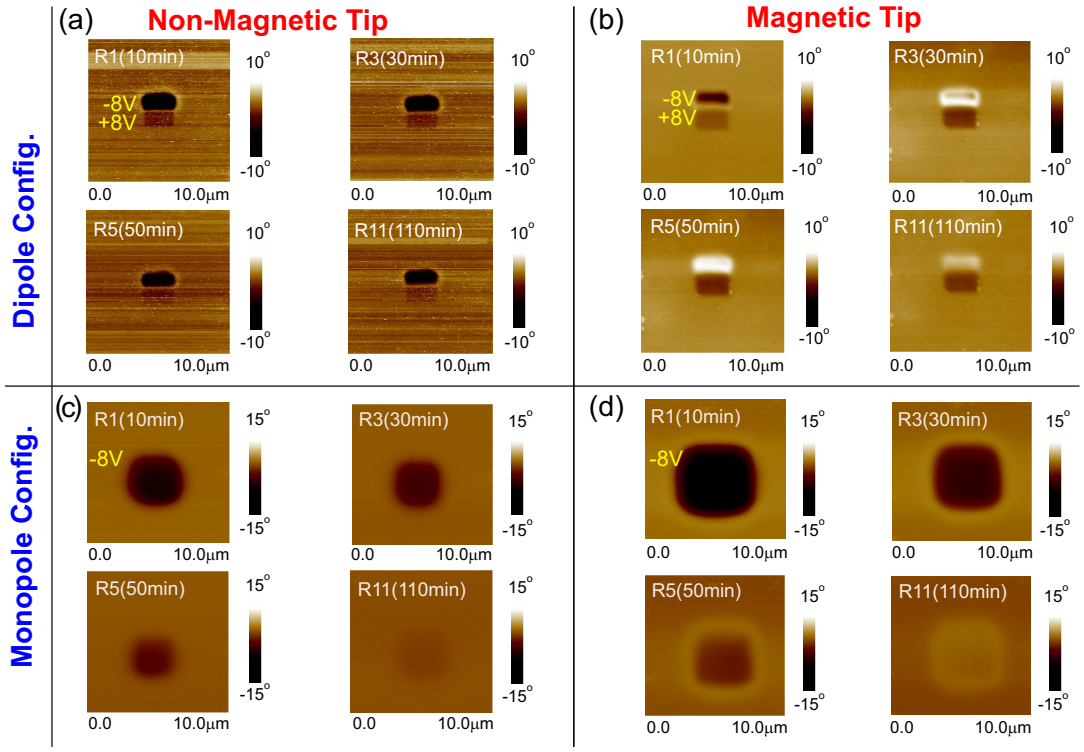

Figure 7.5: (a) and (b) Time dependent phase images of the nano-electrical domains written in dipole configuration read by using a non-magnetic and magnetic tip respectively. (c) and (d) Time dependent phase images of the nano-electrical domains written in monopole configuration read by using a non-magnetic and magnetic tip respectively.

shown in AFM images of **Fig. 7.5(a)**.

On the other hand, when dipole configuration was read with magnetic tip, the nature of interaction of the negative charge region, which had dark contrast (referring attractive interaction between tip and written region) in the beginning turned brighter (repulsive) with time. The contrast completely flipped after 40 minutes and then decayed with time. The time evolution of the phase change is shown in **Fig. 7.5(b)**.

This was really surprising and to explore more, when we read the monopole configuration (i.e. charge written with only -8V) using both non-magnetic and magnetic tips, we found no phase polarity change even with magnetic tip. The phase simply decayed with time in both the cases as shown in AFM phase images of **Fig. 7.5(c)** and **(d)**. The normalized phase change of the negative charge region for

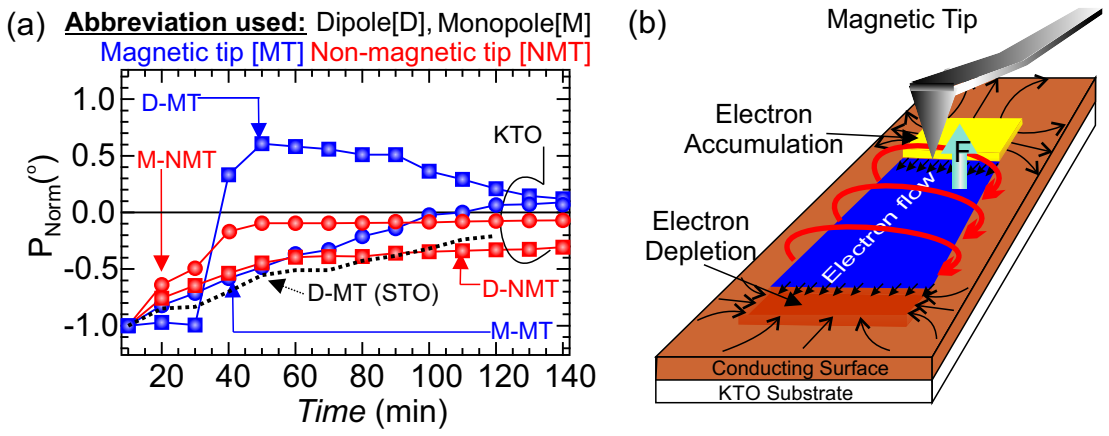

Figure 7.6: (a) Normalized phase change vs. time plot for the negative charge region of monopole and dipole configuration read using non-magnetic and magnetic tips. (b) Schematic presentation of possible mechanism behind repulsion of magnetic tip by charge written in dipole configuration.

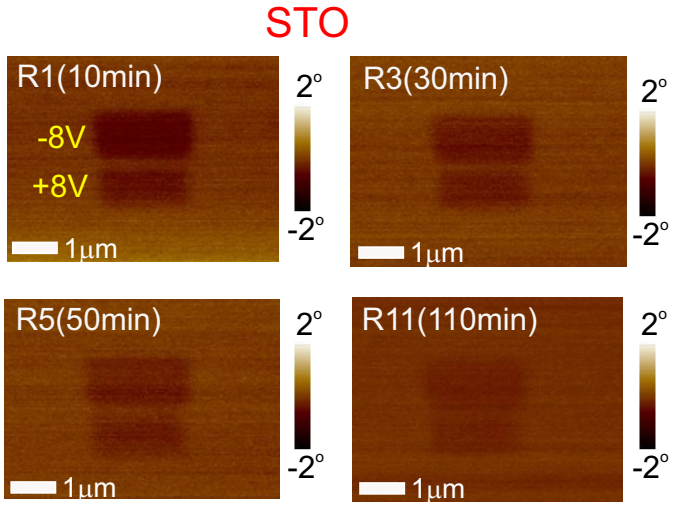

Figure 7.7: Time dependent phase images of dipole configuration written on Ar^+ bombarded STO and read using magnetic tip.

the above four cases is plotted as a function of time in **Fig. 7.6(a)**. It can be seen from the figure, when the dipole configuration is read using magnetic tip (D-MT case), the polarity of the phase measured at the center of the negative charge region flips from negative to positive and then decays. While, for the other three cases: dipole configuration read using non-magnetic tip (D-NMT), monopole configuration read using magnetic and non-magnetic tip (M-MT and M-NMT respectively), the phase simply decays towards zero.

A possible explanation of this observation can be a flow of electrons on the surface of the sample with dipole configuration of nano-electrical domains with the -8 V region acting as the source of electrons while the +8 V region as the sink. Then in between +8 V and -8 V written regions, a net electric current may flow that produces a magnetic field which will exert a repulsive force on the magnetic tip and not on the non-magnetic tip. We have tried to present this situation schematically in **Fig. 7.6(b)**. No repulsive force is experienced in the monopole configuration even on using magnetic tip because in this case, electric charge is flowing equally in all directions producing no net current and hence magnetic field. But typically, the flow of charge carriers from the -8 V region to +8 V region should subside within a few picoseconds and result in a fixed space charge layer with no further charge transfer between the two regions. Also, the current and hence the magnetic field might be too small to exert any significant force on the magnetic tip. Another possibility that might explain the observed experimental results is the oxygen vacancy re-distribution on writing with opposite polarity voltage. This may produce a net magnetic moment resulting in repulsion of the magnetic tip.

To further check if this phenomenon is common to other perovskite oxides as well, we did similar experiment on Ar^+ bombarded STO by writing in dipole configuration and reading with magnetic tip. Surprisingly, no flip in the polarity of the phase of the -8 V written region was observed. The phase simply decays over time as shown in **Fig. 7.7**. This suggests that the flipping of the polarity of the phase is a unique property of KTO and might be related to the interplay between the strong spin orbit coupling of KTO and the defect-redistribution.

Figure 7.8 shows the pincode of Institute of Nano Science and Technology (INST), Mohali (160062) written in binary form of KTO single crystal by applying opposite polarity writing voltage for 0 and 1.

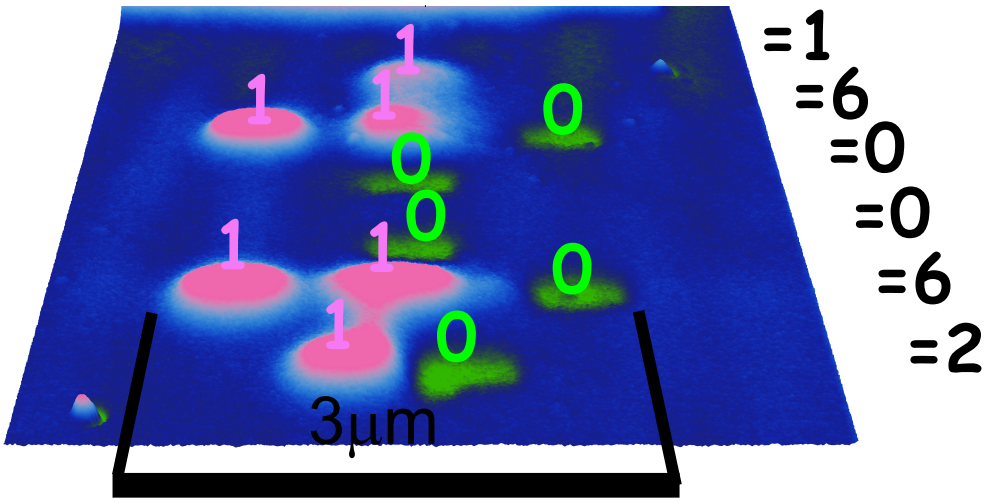

Figure 7.8: Pincode of INST (160062) in binary form written on KTO using tip bias voltage of opposite polarity for 0 and 1.

7.3 Conclusion

In conclusion, we have written nano-electrical domains on the surface of oxygen vacant conducting KTO. The written signal on KTO is around three times more than that reported in other perovskite oxide systems. KPFM measurements reveal that charge writing is predominantly electron accumulation or depletion process due to re-distribution of oxygen vacancies. Magnetic force microscopy could detect the generation of a magnetic field produced in absence of an external voltage, when charge writing was done in a dipolar configuration. A control experiment on STO suggest that this generation of magnetic field might be unique for KTO. Our observations may pave a way for spin-charge based nano-electronic devices and sensor for magnetic nano-structures.

Bibliography

[1] C.N.R. Rao, *Annu. Rev. Phys. Chem.*, **40**, 291 (1989).

[2] M. Bibes and A. Barthelemy, *IEEE transactions on Electron Devices*, **54(5)**,1003 (2007).

[3] N. Reyren, M. Bibes, E. Lesne, J.M. George, C. Deranlot, S. Collin, A. Baethelemy, and H. Jaffires, *Phys.Rev. Lett.*, **108**, 186802 (2012).

[4] M. Bibes, J.E. Villegas, and A. Barthelemy, *Advances in Physics*, **60(1)**, 5 (2011).

[5] A. Ohtomo and H.Y. Hwang, *Nature*, **47**, 424 (2004).

[6] Y. Tokura, A. Urushibara, Y. Moritomo, T. Arima, A. Asamitsu, G. Kido, and N. Furukawa, *J. Phys. Soc. Jpn.*, **63**, 393 (1994).

[7] J.F. Schooley, W.R. Hosler, and M.L. Cohen, *Phys. Rev. Lett.*, **17**, 474 (1964).

[8] K. Ueno, S. Nakamura, H. Shimotani, A. Ohtomo, N. Kimura, T. Nojima, H. Aoki, Y. Iwasa, and M. Kawasaki, *Nat. Mater.*, **7**, 855 (2008).

[9] K. Ueno, S. Nakamura, H. Shimotani, H.T. Yuan, N. Kimura, T. Nojima, H. Aoki, Y. Iwasa, and M. Kawasaki, *Nat. Nanotech.*, **6**, 408 (2011).

[10] Y. Ohuchi, J. Matsuno, N. Ogawa, Y. Kozuka, M. Uchida, Y. Tokura, and M. Kawasaki, *Nat. Commun.*, **9(213)**, 1 (2018).

[11] C.H. Ahn, J.M. Triscone, and J. Mannhart, *Nature* **424**, 1015 (2003).

[12] Y.Y. Pai, H. Lee, J.W. Lee, Y. Kozuka, A. Annadi, G. Cheng, S. Lu, M. Tomczyk, M. Huang, C.B. Eom, P. Irvin, and J. Levy, *Phys. Rev. Lett.*, **120**, 147001 (2018).

[13] C.H. Ahn, T. Tybell, L. Antognazza, K. Char, R.H. Hammond, M.R. Beasley, O. Fischer, and J.M. Triscone, *Science*, **276**, 1100 (1997).

[14] C. Cen, S. Thiel, G. Hammerl, C.W. Schneider, K.E. Andersen, C.S. Hellberg, J. Mannhart, and J. Levy, *Nat. Lett.* **7**, 298 (2008).

[15] C. Cen, S. Thiel, J. Mannhart, and J. Levy, *Science*, **323**, 1026 (2009).

[16] Y. Xie, C. Bell, T. Yajima, Y. Hikita, and H.Y. Hwang, *Nano Lett.*, **10**, 2588 (2010).

[17] F. Bi, D.F. Bogorin, C. Cen, C.W. Bark, J.W. Park, C.B. Eom, and J. Levy, *Appl. Phys. Lett.*, **97**, 173110 (2010).

[18] Y. Xie, C. Bell, Y. Hikita, and H.Y. Hwang, *Adv. Mater.*, **23**, 1744 (2011).

[19] M. Balal, S. Sanwlani, N. Wadehra, S. Chakraverty, and G. Sheet, *Appl. Phys. Lett.*, **110**, 261604 (2017).

[20] H. Suzuki, N. Wakiya, N. Sakamoto, Y. Hoshi, and J. Akedo, *Trans. Mat. Res. Soc. Japan*, **33**, 21243 (2008).

[21] F. Yan, F. Schoofs, J. Shi, S. D. Ha, R. Jaramillo and S. Ramanathan, *J. Mater. Chem. C*, **2**, 23805 (2014).

[22] W. M. D. Wright and D. G. Chetwynd, *Nanotechnology*, **9**, 133 (1998).

[23] N. Wadehra, R. Tomar, S. Halder, M. Sharma, I. Singh, N. Jena, B. Prakash, A.D. Sarkar, C. Bera, A. Venkatesan, and S. Chakraverty, *Phys. Rev. B*, **96**, 115423 (2017).

[24] N. Balke, P. Maksymovych, S. Jesse, A. Herklotz, A. Tselev, C.B. Eom, I.I. Kravchenko, P. Yu, and S.V. Kalinin, *ACS Nano*, **9**, 6484 (2015).

[25] M. Andrae, F. Gunkel, C. Baumer, C. Xu, R. Dittmann, and R. Waser, *Nanoscale*, **7**, 14351 (2015).

[26] S. Das, B. Wang, Y. Cao, M.R. Cho, Y.J Shin, S.M. Yang, L. Wang, M. Kim, S.V. Kalinin, L.Q. Chen, and T.W. Noh, *Nat. Commun.*, **8**, 615 (2017).

Chapter 8

Summary and Future Scope

8.1 Summary

Transition metal oxides are the potential candidates to be explored for enhanced properties and greater integrability for future generation electronic devices. The vast spectrum of exotic properties of oxides even make them interesting for realizing and understanding the different physical phenomena fundamentally. This thesis work is a step towards the realization of an all-oxide spin-transistor. In this thesis, we have focused on perovskite oxide (KTO) with strong spin-obit coupling and have realized its conducting interface with other perovskite oxide (LVO) which can be used as a channel material of the spin-transistor. This interface is found to host many emergent phenomena like Rashba spin-splitting, highest spin-orbit coupling, anisotropic magnetoresistance and planar Hall effect which not only open opportunities for devices with enhanced properties but also make this interface a hunting ground for exploring the physical phenomena and building up our understanding about these processes.

Since this thesis mainly deals with oxides and their use in spintronics, in first chapter, we have introduced the different properties of oxides which make them the suitable candidates for future generation electronic devices. We have also given an overview of the spitronics, its basic principle-the Rashba effect and explained about the functioning of a spin-transistor in this chapter. Also, we have briefly touched on the thin-film growth technology and discussed how it can be used to make all-oxide spintronic devices. We have also introduce the formation of two dimensional electron

gas at the interface of oxides and discussed their possible mechanisms. Then, we have focused on the properties of KTO which is the key player of this thesis work and have discussed the work done on KTO in the past. In the second chapter, we have discussed the different experimental techniques used for the completion of thesis work. The detailed working of pulsed laser deposition technique which was used to grow the heterostructures of LVO-KTO is explained. The various growth parameters and their optimization is discussed in this chapter. Also, RHEED- the technique to monitor the thickness and quality of the films is described. We have also discussed the basics of surface and structural characterization of the samples done using AFM and XRD respectively. Other than these, the electrical and magneto-transport measurements by physical property measurement system are discussed. Also, other measurement tools like DPSS lasers and the source meters are introduced in this chapter.

As the foremost step to make thin film heterostructures is the substrate preparation, in the third chapter, we have discussed the procedure to prepare the KTO substrates. To realize the conducting interface between two insulating oxides, the terminating layer of the substrate plays a crucial role. Hence, we have discussed an indigenously developed non-corrosive method of attaining single (TaO_2) termination of the KTO substrate. Using the high temperature annealing method followed by DI water etching, we have shown that we were successful to attain the singly terminated KTO substrates. Also, as the oxygen vacancies modify the electronic band structure of the oxides greatly, in the second part of the chapter, we have discussed the effect of oxygen vacancies on the band structure of KTO. For this study, we have intentionally created oxygen vacancies in the KTO single crystals by Ar^+ ion bombardment and studied their effect on the work function and band gap of KTO. Through our experimental optical spectroscopy measurements and KPFM measurements along with first principle DFT based theoretical simulations, we have presented a band line-up of the KTO single crystals showing the effect of oxygen vacancies.

In fourth chapter, we have discussed in detail the fabrication of oxide heterostructure of LVO-KTO. The growth parameter optimization and the variation of the electrical properties of the heterostructure with the variation of the thickness of the LVO film is discussed. The interface made out of two insulating oxides is shown to be conducting as a function of the thickness in accordance with electronic reconstruction mechanism of the interfacial conductivity. The quality of the LVO films is discussed using RHEED, XPS and XRD measurements.

In the fifth chapter, we have shown the magneto-transport measurements performed on the LVO-KTO heterostructure. From the out-of-plane magnetoresistance measurements, we have shown that the interface has the highest spin-orbit coupling strength among all perovskite oxides reported so far. The chapter also shows the non-trivial anisotropic magnetoresistance and planar Hall effect observed for this interface when magnetic field is applied in the current carrying plane of the sample. These observations are generally observed for the magnetic or topological systems and are predicted for systems with Rashba spin bands. Our theoretical model based on Rashba spin-split bands in LVO-KTO is able to capture our experimental observations at low magnetic fields giving us evidence of presence of Rashba type spin splitting in the system. This chapter discusses the topological characteristics of the electronic bands of the heterostructucture and shows the signature of chiral anomaly as observed in the topological materials having different charge carriers with opposite chairalities. The observation of these emergent phenomena in a heterostructure of simple cubic perovskite oxides is really exciting and open up a pool of opportunities to be explored using this heterostructure.

The sixth chapter discusses the photoresponse of the oxygen vacant KTO under daylight illumination and under monochromatic laser light of different wavelengths 405 nm (equivalent to the band gap), 532 nm and 633 nm (less than the band gap of the material). The dynamics of the photoresponse of the KTO single crystals is discussed and the response times are calculated as a function of the charge carrier density of the samples. Using these photoconductivity measurements, the position of the defect states in the band gap of the system is probed. It is found that the majority of the carriers are excited from the defect states present 0.87 eV above the valence band of the system. In addition to this, the resistivity measurements coupled with KPFM measurements are used to know about the preferential directions of the oxygen vacancy formation in the system. A cris-cross pattern along (100) and (010) crystallographic directions is observed on the surface of oxygen vacant KTO samples suggesting the creation of oxygen vacancies in these preferred directions.

Seventh chapter discusses the applicability of KTO for memory device applications. In this chapter, we have shown that nano-electrical domains can be written on oxygen vacant KTO using conducting AFM tip. The written structures can also be erased infinite number of times making KTO useful for storage device applications. The writing ability of KTO is found to be three times more than that of STO. The KPFM measurements suggests that writing pattern either accumulates or depletes electrons at the written region from the surrounding electron sea or

re-distributes oxygen vacancies in the system depending upon the sign (positive or negative) of applied voltage on the tip. Magnetic force microscopy detects the appearance of a magnetic field when charge writing is done in a dipolar configuration. This may open up opportunities in the field of nano-electric devices for magnetic sensor applications.

8.2 Future Scope

With the emerging development in the field of technology, there is a great scope to unfold the mysteries of nature using simple systems as oxides and to utilize their exotic properties for device applications in our daily life. As mentioned earlier, this thesis work for the fabrication of polar-polar oxide heterostructure with insulating oxides having strong spin-orbit coupling is the first step towards realization of an all-oxide spin-transistor. The heterostructure LVO-KTO can be used as the channel material of the spin transistor but further work needs to be done to explore for ferromagnetic oxides to be used for source and drain of the transistor. Then a detailed study for optimization and characterization of the heterojunction of the source/drain oxide with LVO and KTO needs to be done so as to attain the impedance matching condition/current flow across the different heterojunctions.

Another possibility is to fabricate a heterostructure of LVO-KTO and induce spin-polarized 2DEG at the interface by depositing another ferromagnetic oxide above LVO which can induce ferromagnetism at the interface by proximity effect. This scheme may cut down the number of heterojunctions to be studied for continuous current flow through the device.

Another work which needs to be done in continuation of this thesis is to explore and understand the band structure of the heterostructure LVO-KTO thoroughly. The study of evolution of the band structure or the crossing point of the Rashba spin bands on application of the magnetic field of increasing magnitude is really crucial to understand the experimental results obtained for in-plane magnetotransport measurements. The appearance of 4 fold oscillations and deviation of PHE amplitude from B^2 dependence at high magnetic fields is still an unanswered question in this thesis. The complete analysis of the band structure evolution of the heterostructure on application of magnetic field can give the answers. Also the signature of chiral anomaly observed in our magnetotransport measurements demands more practical explanation. The spin-texture or the Rashba spin-splitting in LVO-

KTO can be studied using angle resolved photoemission spectroscopic (ARPES) measurements. Also, transmission electron microscopy (TEM) measurements can give a detailed understanding of the heterointerface and can also shed light on the exact mechanism behind the interfacial conductivity in this heterointerface.

Further, tuning of the spin-orbit coupling strength as a function of charge carriers can be studied using external gate voltage and its effect on the Rashba physics of the heterostructure can be explored which may further enhance the applicability of this heterostructure for device applications.

Other than this, since LVO has photovoltaic properties, studying the photoresponse of LVO-KTO heterostructure would be really interesting. Also, the dynamics of the charge carriers of the 2DEG at the interface of LVO-KTO can be explored using ultrafast spectroscopy.

In addition to the LVO-KTO heterostructure, further studies should be carried out to understand the exact mechanism behind the charge writing phenomena on the oxygen vacant KTO samples. More experiments to determine the time scales of the written structures should be performed. Experiments to further enhance the efficiency and towards practical implication of the electrostatic memory devices using oxides should be performed.

Simple cubic transition metal perovskite oxides with strong spin orbit coupling are a store house of emergent properties which have started making their mark as alternative materials for electronic device applications. Their further utilization can revolutionise the entire field as they are not just alternative materials for different applications but also, they offer a vast range of alternative mechanisms to achieve a particular target. This increases the degrees of freedom to tune the desired properties. Hence, oxides should be utilized to their fullest as they are the future of the next generation electronic devices.

List of publications

Publications included in thesis

1. **Neha Wadehra**, Ruchi Tomar, R.K. Gopal, Yogesh Singh, Sushanta Dattagupta, and S. Chakraverty, Planar Hall Effect and Anisotropic Magnetoresistance in a polar-polar interface of $LaVO_3$-$KTaO_3$ with strong spin-orbit coupling, ***Nat. Commun.***, 11, 874 (2020).

2. **Neha Wadehra**, Nand Kumar, Shivam Mishra, Ruchi Tomar, and S. Chakraverty, Nano-electrical domain writing for oxide electronics, ***Appl. Surf. Sci.***, 509, 145214 (2020).

3. **Neha Wadehra**, and S. Chakraverty, Electrostatic Memory in $KTaO_3$, ***Appl. Phys. Lett.***, 114, 163103 (2019).

4. **Neha Wadehra**, Ruchi Tomar, S. Halder, M. Sharma, I. Singh, N. Jena, B. Prakash, A. D. Sarkar, C. Bera, A. Venkatesan, and S. Chakraverty, Electronic structure modification of the $KTaO_3$ single-crystal surface by Ar^+ bombardment, ***Phys. Rev. B***, 96, 115423 (2017).

5. Ruchi Tomar, **Neha Wadehra**, Shelender Kumar, Ananth Venkatesan, D. D. Sarma, Denis Maryenko, and S. Chakraverty, Defects, conductivity and photoconductivity in Ar^+ bombarded $KTaO_3$, ***J. Appl. Phys.***, 126, 035303 (2019).

6. Ruchi Tomar, **Neha Wadehra**, V. Budhiraja, B. Prakash, S. Chakraverty, Realization of single terminated surface of perovskite oxide single crystals and their band profile: $(LaAlO_3)_0.3(Sr_2AlTaO_6)_0.7$, $SrTiO_3$ and $KTaO_3$ case study, ***Appl. Surf. Sci.***, 427, 861 (2017).

Publications not included in the thesis

1. Saveena Goyal, **Neha Wadehra** and S. Chakraverty, Tuning the electrical state of 2DEG at $LaVO_3$-$KTaO_3$ interface: Effect of light and electrostatic Gate, ***Adv. Mater. Interfaces***, 2000646 (2020).

2. Amit, R.K.Singh, **Neha Wadehra**, S. Chakraverty and Yogesh Singh, Type-II Dirac semimetal candidates ATe_2 (A = Pt, Pd): A de Haas-van Alphen study, ***Phys. Rev. Mater.***, 2, 114202 (2018).

3. Mohammad Balal, Shilpa Sanwlani, **Neha Wadehra**, S. Chakraverty, and Goutam Sheet, Electrical domain writing and nanoscale potential modulation on $LaVO_3/SrTiO_3$, ***Appl. Phys. Lett.***, 110, 261604 (2017).

4. Ruchi Tomar, **Neha Wadehra**, Vishwajit M. Gaikwad, and S. Chakraverty, Low field manifestation of spiral ordering in sheet like $BiFeO_3$ nanostructures, ***AIP Advances***, 8, 085306 (2018).

5. Nand Kumar, Ruchi Tomar, **Neha Wadehra**, M. Manolata Devi, Bhanu Prakash, Suvankar Chakraverty, Growth of Highly Crystalline and Large Scale Monolayer MoS_2 by CVD: The Role of substrate Position, ***Crys. Resear. Techno.***, 53, 1800002 (1-7) (2018).

6. **Neha Wadehra**, R. Gupta, B. Prakash, D. Sharma and S. Chakraverty, Biocompatible ferrite nanoparticles for hyperthermia: effect of polydispersity, anisotropy energy and inter-particle interaction, ***Materials Research Express***, 4(2), 025037 (2017).

Publications under review

1. Nand Kumar, **Neha Wadehra**, Ruchi Tomar, Sushanta Dattagupta, Sanjeev Kumar, and S. Chakraverty, Observation of Shubnikov-de Haas Oscillations, Non-trivial Berry Phase, Planar Hall and Anisotropic Magnetoresistance at the conducting interface of EuO-$KTaO_3$. **arxiv identifier: 1908.04977** (2019).

Research Schools, Workshops and Conferences

1. Presented poster in "Nano India 2019" conference organized by Mahatma Gandhi University, Kerala, India held from 26th-27th April 2019.

2. Presented poster in "Advanced School and Workshop on Correlations in Electron Systems- from Quantum Criticality to Topology" organized by Abdus Salam International Centre for Theoretical Physics (ICTP) in Trieste, Italy from 6th - 17th August 2018.

3. Presented poster in "IUMRS-International Conference of Young Researchers on Advanced Materials (ICYRAM) 2016" organized by International Union of Material Research Societies in Indian Institute of Science, Bangalore, India held from 11th-15th December 2016.

4. Received **best poster award** for poster entitled "Electronic properties of high mobility Spintronic materials" in 6th MRS Trilateral symposium-2015 organized by Material Research Society in Indian Institute of Science Education and Research, Mohali, Punjab, India from 23rd to 25th November, 2015.

5. Presented poster in "2nd Australia-India Strategic Research Fund (AISRF) meeting 2015" organized by Institute of Nano Science and Technology, Mohali, Punjab, India from 25th -27th November, 2015.

6. Presented poster on "Negative index metamaterials" in 1st IAPT National Student Symposium on Physics at Panjab University Chandigarh, India from 25th-27th February,2013.

7. Presented poster in "Chandigarh Science Congress CHASCON-2013" at Panjab University Chandigarh, India from 1st-3rd March 2013.